

LASER DIAGNOSTICS OF PLASMA ASSISTED COMBUSTION

By

Xing Rao

A DISSERTATION

Submitted to  
Michigan State University  
in partial fulfillment of the requirements  
for the degree of

Doctor of Philosophy

Mechanical Engineering

2010

# ABSTRACT

## LASER DIAGNOSTICS OF PLASMA ASSISTED COMBUSTION

By

Xing Rao

In this study, a microwave re-entrant cavity discharge system and a direct current (DC) plasmatron are used to investigate flame enhancement and nitric oxide (NO) formation using laser and optical diagnostics. The uniqueness of this study lies in the direct coupling concept, a novel highly efficient strategy used here for the first time.

To investigate combustion dynamics of direct microwave coupled combustion, an atmospheric high- $Q$  re-entrant cavity applicator is used to couple microwave (2.45 GHz) electromagnetic energy directly into the reaction zone of a premixed laminar methane-oxygen flame using a compact torch. When microwave energy increases, a transition from electric field enhancement to microwave plasma discharge is observed. At 6 to 10 Watts, ionization and eventually break-down occurs. 2-D laser induced fluorescence (LIF) imaging of hydroxyl radicals (OH) and carbon monoxide (CO) is conducted in the reaction zone over this transition, as well as spectrally resolved flame emission measurements. These measurements serve to monitor excited state species and derive rotational temperatures using OH chemiluminescence for a range of equivalence ratios (both rich and lean) and total flow rates.

Combustion dynamics is also investigated for plasma enhanced methane-air flames

in premixed and nonpremixed configurations using a transient arc *DC* plasmatron. Results for *OH* and *CO PLIF* also indicate the differences in stability mechanism, and energy consumption for premixed and nonpremixed modes. It is shown that both configurations are significantly influenced by in-situ fuel reforming at higher plasma powers.

Parametric studies are conducted in a plasma assisted methane/air premixed flame for quantitative *NO* production using a *DC* plasmatron with *PLIF* imaging. Quantitative measurements of *NO* are reported as a function of gas flow rate (20 to 50 *SCFH*), plasma power (100 to 900 *mA*, 150 to 750 *W*) and equivalence ratio (0.7 to 1.3). *NO PLIF* images and single point *NO* concentrations are presented for both plasma discharge only and for methane/air plasma enhanced combustion cases. *NO* formation occurs predominantly through  $N_2(\nu)+O \rightarrow NO+N$  for the pure plasma discharge without combustion. The *NO* concentration for the plasma enhanced combustion case (500 to 3500 *ppm*) was an order of magnitude smaller than the pure plasma discharge (8000 to 15000 *ppm*) due to the reduction of nitrogen break up from plasma reactions by the methane. Experiments show the linear decay of *NO* between the equivalence ratio range 0.8 to 1.2 under the same flow condition and discharge current.

The diagnostic methods performed in this study include: (1) species concentration by laser induced fluorescence (*NO*, *OH* and *CO*); (2) rotational temperature by optical emission spectroscopy; (3) excited species emission by optical emission spectroscopy; (4) IR thermometry; and (5) multi-line *NO PLIF* thermometry.

© Copyright by Xing Rao 2010  
All Rights Reserved

To my wife, Shujian Shi  
For her dedication and support

## ACKNOWLEDGMENTS

First and foremost, I would like to thank my adviser, Dr. Tonghun Lee, for his generous support during my Ph.D. study, and for his guidance and advising of my research work. Without his wisdom and drive, this program would have been significantly less. You will be my life-time mentor and advisor.

I want to express my sincere gratitude to Dr. Jes Asmussen, Dr. Timothy Grotjohn, Dr. Indrek Wichman and Dr. Guoming Zhu for their helpful and insightful suggestions throughout this program.

I would like to thank my colleagues, Casey Allen, Steve Hammack, Zach Williams, Kadek Hemawan, Xiaojian Yang, Zhen Ren, Xuefei Chen and Xin Wang for their support and assistance with the experiments. I am also grateful to all the staffs and students in Energy and Automobile Research Lab, especially Gary and Jeff from the machine shop were of great help. Special thanks to Dr. Harold Schrock for the nice building and equipments.

I also would like to acknowledge the sponsorship of the U.S. Air Force Office of Scientific Research with Dr. Julian Tishkoff as Program Manager, and Michigan State University. I also want to thank Dr. Campbell Carter from WPAFB for his help with experiments and guidance in publication writing.

Finally, I am sincerely grateful to my parents and my sister Dan for their understanding and encouragement for my whole life. I would also like to convey my heartfelt gratitude to my wife, Shujian Shi, for her love, support and confidence in me.

## TABLE OF CONTENTS

LIST OF TABLES .....	x
LIST OF FIGURES .....	xi
LIST OF SYMBOLS.....	xvi
LIST OF ABBREVIATIONS .....	xvii
Chapter 1, Introduction.....	1
1.1 Background and Motivation .....	1
1.2 Recent Progress on Plasma Assisted Combustion .....	3
1.3 Scope of Research.....	16
Chapter 2, Basic Knowledge of Spectroscopy.....	19
2.1 Introduction to Laser Induced Fluorescence ( <i>LIF</i> ) .....	19
2.2 <i>NO LIF</i> : Literature Survey.....	29
Chapter 3, Experimental Facility .....	33
3.1 Microwave Plasma System.....	33
3.2 Direct Current Plasma System.....	43
3.3 Laser and Optical Diagnostics Setup.....	48
Chapter 4, Combustion Dynamics with Microwave Discharge .....	55
4.1 Impact on Flame Structure and Radical Concentration .....	55
4.2 Flammability Limits and Flame Speed .....	62
4.3 Emission Measurements and Temperature .....	64
4.4 In-Situ Fuel Reforming.....	69
Chapter 5, Combustion Dynamics in a <i>DC</i> Plasmatron.....	73
5.1 Premixed and Non-Premixed Modes .....	73
5.2 Impact on Flame Structure.....	75
5.3 Impact on Radical Concentration.....	80
5.4 Flame Stability, <i>CO</i> Formation and Energy Efficiency .....	84
Chapter 6, Nitric Oxide Formation in a <i>DC</i> Plasmatron.....	91
6.1 Nitric Oxide Formation in Flames .....	91
6.2 Quantification of Nitric Oxide.....	94
6.3 Temperature Profile Measurements .....	96

6.4 Planar Laser-Induced-Fluorescence ( <i>PLIF</i> ) Imaging of <i>NO</i> .....	100
6.5 Temperatures and <i>NO</i> Concentrations in Plasma Discharge Only.....	102
6.6 Temperatures and <i>NO</i> Concentrations in a Plasma Enhanced Flame .....	109
Chapter 7, Conclusion and Future Work.....	117
7.1 Microwave Discharge Results .....	117
7.2 <i>DC</i> Discharge Results .....	119
7.3 Nitric Oxide Measurements Results .....	120
7.4 Some Suggestions for Future Work .....	121
Bibliography.....	123

## LIST OF TABLES

Table 4.1: Transitions for <i>OH</i> rotational Temperature Method .....	67
Table 5.1: Thermocouple Measurements and Calibrations .....	79
Table 6.1: Reactions for <i>NO</i> formation in methane/air flame in plasma .....	91
Table 6.2. Energy data of discharge only in air with different current.....	106
Table 6.3. <i>NO</i> Concentration in Air over in <i>PAC</i> .....	109

## LIST OF FIGURES

Figure 1.1 Effect of different types of discharge on the maximum co-flow speed (blow-off velocity) [8].	5
Figure 1.2 Discharge-enhanced flame stabilization. (a) Without discharge. (b) With discharge. The flame is lifted off in (a) and reattached by discharges in image (b). The electrode position is 10 diameters (46 mm) above the nozzle. [8].	6
Figure 1.3 Comparison of $OH$ ( $A-X$ ) emissions with and without discharge [30].	6
Figure 1.4 Schematic of the plasma-assisted combustion experiment in a supersonic flow [5].	7
Figure 1.5 Photograph of the discharge in air (top) and of the discharge/flame region in ethylene-air (bottom) [4].	8
Figure 1.6 Experimental and computational results of ignition temperatures with 20% Methane in Nitrogen with preheated air in a MGA ( $I = 350 \text{ mA}$ ) [6].	9
Figure 1.7 Lifetimes of plasma produced species as a function of pressure. [7].	10
Figure 1.8 Lifted flame speed enhancements by addition of $O_3$ at 1 atmospheric pressure [6].	11
Figure 1.9 Images of $OH$ -number density in equivalence ratio of 0.76 $CH_4$ /air flame without (a) and with (b) microwave radiation.[12].	12
Figure 1.10 Schematic of gliding arc and the electric components (Left). Photo image of $GA$ discharge (Right) [32].	13
Figure 1.11 $ICCD$ images of plasma discharge development (camera gate time is 200 $ps$ . One atmospheric pressure, $U = 20 \text{ kV}$ ) [33].	14
Figure 1.12 Flow temperatures (Left $Y$ axis) and unreacted fuel fraction (Right $Y$ axis) downstream of the discharge vs. equivalence ratio in flow mixed with methane and air. Pressure is 100 $\text{torr}$ with no flame detected in the test section. [23]	14

Figure 1.13 Images of plasma combustion, 70 torr total pressure in air (left) and $C_2H_4$ /air at equivalence ratio of 0.9 (right). [23] .....	15
Figure 1.14 Percentage of fuel left which is unreacted in the flow in a transverse RF discharge with shaded areas indicating conditions when flame occurs. [34].....	15
Figure 1.15 Discharge temperature (a) and unreacted fuel fraction (b) as functions of flow velocity. Ethylene/air, P=70 torr, $\phi=1.0$ , pulser rep rate 50 kHz. Closed symbols indicate ignition is achieved [35]. .....	16
Figure 2.1 Two-level system with pertinent energy transfer processes. ....	22
Figure 2. 2 Transition from linear regime to saturation regime in the non-transient two-level model in a 1 bar, equivalence ratio of 0.9 methane/air flame. Difference for four small figures are different laser intensity scale [44]......	27
Figure 3.1: Picture of coaxial re-entrant cavity applicator with three fine adjustments using unislides; picture of methane/oxygen flame shown in the inset.....	34
Figure 3.2 Scheme of the structure of coaxial re-entrant cavity applicator with burner centered in the middle.....	35
Figure 3.3: Equivalent circuit for coaxial re-entrant cavity applicator.....	39
Figure 3.4: Numerical simulation of electric field from (V/m) COMSOL MultiPhysics RF Electromagnetic solver for current experiments.....	40
Figure 3.5 Components of microwave cavity plasma assisted flame system with E-field pattern shown in the figure [53]......	42
Figure 3.6 Flame extinction limits (lean) with 10 Watts, and 20–100 Watts microwave power. [53]......	43
Figure 3.7 Image and schematic of transient arc plasmatron with gas/liquid feeding (a); Air plasma imaging at 20 SCFH and 300 mA (b); Plasma assisted stoichiometric methane/air imaging at 20 SCFH and 300 mA (c). .....	44
Figure 3.8 Schematic of transient arc plasmatron with gas/liquid feeding.....	45
Figure 3.9 Typical DC discharge gap voltage and current passing through the gap [54].	47

Figure 3.10 Voltage and current plots for discharge in air/propane mixture and <i>CCD</i> images of the discharge with exposure time of $\Delta t$ shown in the voltage-current plot [54].	48
Figure 3.11 Overall experimental setup with synchronization of lasers, energy monitor, <i>ICCD</i> camera and control system.	49
Figure 3.12 Excitation Spectra of <i>OH</i> ( <i>A-X</i> ) with $Q_1(8)$ transition shown at 283.029 <i>nm</i> .	50
Figure 3.13 Excitation Spectra of <i>CO</i> ( <i>B-X</i> ) with highest intensity at 230.109 <i>nm</i> .	51
Figure 3. 14 . Spectrally resolved <i>I-D</i> line imaging (inset) and the emission spectra of <i>NO-LIF</i> with 226.03 <i>nm</i> excitation and selected filter function (solid red line). The emission spectra has contributions from <i>NO</i> , <i>O<sub>2</sub></i> and Rayleigh scattering.	53
Figure 4.1 Emission (top), <i>OH PLIF</i> (middle) and <i>CO PLIF</i> (bottom) intensity images of <i>CH<sub>4</sub>/O<sub>2</sub></i> flame vs. microwave power with three stages noted (100 <i>SCCM</i> total flowrate at $\phi=1.1$ ).	55
Figure 4.2 <i>OH</i> number density in burnt gas of <i>CH<sub>4</sub>/O<sub>2</sub></i> flame vs. microwave powers from averaged <i>PLIF</i> images.	58
Figure 4.3 <i>OH</i> number density vs. equivalence ratios ( $\phi=0.8$ to 1.2) with different microwave powers (0 to 30 <i>Watts</i> ). Total flow rate is 100 <i>SCCM</i> .	62
Figure 4.4 Flammability limits for methane/oxygen flame (lean and rich) with flamespeed increase demonstrated by flame photographs with no microwave radiation and 10 <i>Watts</i> microwave radiation (right top).	63
Figure 4.5 Emission spectra from <i>CH<sub>4</sub>/O<sub>2</sub></i> flame with no microwave radiation and 10 <i>Watts</i> microwave radiation (top) and <i>OH</i> rotational temperature at the same conditions as in Figure 4.2 (bottom).	65
Figure 4.6 Sample Image to show how to get <i>OH</i> rotational temperature at condition of 100 <i>SCCM</i> total flow rate and equivalence ration of 1.1. The <i>OH</i> rotational temperature using this method is 2,900 <i>K</i> .	68
Figure 4.7 <i>CO</i> number density in burnt gas of <i>CH<sub>4</sub>/O<sub>2</sub></i> flame vs. microwave powers at the same conditions as in Figure 4.2 using <i>CO</i> Two-Photon Laser Induced Fluorescence.	71

Figure 5.1: Schematic of transient arc plasmatron with cathode in the center and two different inlets are used to get two different experimental setup(left); Images for premixed (100 mA and 400 mA DC current) and nonpremixed (0 and 400 mA DC current) flames of methane/air with equivalence ratio of 0.9.....	73
Figure 5.2: Single and averaged 2-D OH Planar Laser-Induced Fluorescence (PLIF) images as a function of increasing microwave power for both premixed flames (top) and nonpremixed flames (bottom). .....	76
Figure 5.3: OH number density is plotted for different DC currents, total flow rates (top, equivalence ratio is fixed at 0.95 and for different DC current, equivalence ratios (bottom, total flowrate is fixed at 15 LPM) in premixed mode.....	82
Figure 5.4: OH number density with the same flow conditions (total flow rate is 9 SLPM, and $\phi=0.95$ ) but different currents for both premixed (from data point the same as in Figure 5.3) and nonpremixed (two data points, one outer flame front and the other one inner flame front as shown) flames. ....	84
Figure 5.5: Averaged OH PLF images for all flowrates at premixed mode with $\phi=0.7$ , 1.0 and 1.3 (top); Averaged OH PLF images for 6 LPM (middle)/15 LPM (bottom) at nonpremixed mode with $\phi=0.7$ , 1.0 and 1.3.....	85
Figure 5.6: Averaged CO PLF images for premixed (insert top) and nonpremixed (insert bottom); CO number density is plotted for with equivalence ratio 0.7 (premixed and nonpremixed) and 1.1 (nonpremixed). ....	88
Figure 5.7: DC Power input with different current for air plasma, premixed flames and nonpremixed flames. ....	90
Figure 6. 1 NOx emission as f function of combustion temperature [30, 84].....	93
Figure 6.2 NO addition method for determination of the baseline strength and the nascent NO concentration. ....	96
Figure 6.3 IR temperature profile with different equivalence ratio for premixed methane and air flame with circle shown in the figure where the multi-line thermometry calibration is used. ....	97
Figure 6. 4 Multi-line NO LIF thermometry (126 transitions between 225.975 nm and 226.1 nm). ....	98

Figure 6.5 Single shot *NO* concentration fields using *NO PLIF* of gas discharge of air and plasma enhanced flames with different plasma power at same gas flow rate (a). Averaged *NO* concentration fields from *NO PLIF* (200 images averaged) of plasma enhanced flames with different plasma power at same gas flow rate (b). ..... 101

Figure 6.6 Temperature (a) and *NO* concentration (b) data at specific location of the discharge for different power levels and air flow rates in discharge only case in air. .... 103

Figure 6.7 Temperature (a) and *NO* concentration (b) data as function of current and flow rate when the equivalence ratio is held at 1 in plasma assisted methane/air flame. .111

Figure 6.8 Temperature (a) and *NO* concentration (b) data as function of current and equivalence ratio when flow rate the same in plasma with methane/air combustion.. .....113

Figure 6.9 Temperature (a) and *NO* concentration (b) data with equivalence ratio and flow rate when the current is the same in plasma assisted methane/air combustion. ....114

## LIST OF SYMBOLS

$T_e$	Electron Temperature
$T_g$	Gas Temperature
$T$	Temperature
$K$	Boltzmann Constant
$N_{NO}$	Number Density of <i>NO</i>
$X_{NO}$	Mole Fraction of <i>NO</i>
$P$	Pressure
$I_{LIF}$	<i>LIF</i> Intensity
$C_p$	Specific Heat
$R_f$	Radio Frequency
$\lambda$	Wavelength
$\omega$	Angular Frequency
$U$	Voltage
$I$	Current

## LIST OF ABBREVIATIONS

<i>PAC</i>	Plasma Assisted Combustion
<i>NO</i>	Nitric Oxide
<i>CO</i>	Carbon Monoxide
<i>LIF</i>	Laser Induced Fluorescence
<i>PLIF</i>	Planar Laser Induced Fluorescence
<i>TALIF</i>	Two Photon Absorption <i>LIF</i>
<i>SCCM</i>	Standard Cubic Centimeter per Minute
<i>SCFH</i>	Standard Cubic Foot per Hour
<i>ppm</i>	particle per million
<i>DC</i>	direct current
<i>AC</i>	alternative current
<i>mA</i>	mili-ampere
<i>UV</i>	UltraViolet
<i>IR</i>	Infrared
<i>eV</i>	electron volt
<i>TEM</i>	Transverse Electromagnetic
<i>CCD</i>	Charge Coupled Device
<i>ICCD</i>	Intensified Charge Coupled Device
<i>NO<sub>X</sub></i>	Nitrogen Oxide

<i>SECD</i>	Single Electrode Corona Discharge
<i>USRD</i>	Ultra-short Repetitive Discharge
<i>DBD</i>	Dielectric Barrier Discharge
<i>MGA</i>	Magnetic Gliding Arc
<i>GA</i>	Gliding Arc
<i>PIV</i>	Particle Image Velocimetry
<i>E.U.</i>	European Union

# Chapter 1 Introduction

## 1.1 Background and Motivation

Plasma assisted combustion has emerged as an important research topic in recent decades as a potential method to improve combustion efficiency in energy conversion and propulsion systems while simultaneously reducing the pollution emissions from advanced gas turbines and aircraft engines. The term ‘plasma’ is described by Bittencourt as “a wide variety of macroscopically neutral substances containing many interacting free electrons and ionized atoms or molecules, which exhibit collective behavior due to long-range Coulomb forces.” [1]. The electron density in a typical flame is close to  $10^8 \text{ cm}^{-3}$  while for plasma assisted combustion cases, it rises to  $10^{11-12} \text{ cm}^{-3}$ . The process of combining a plasma discharge with combustion is a sophisticated one, requiring knowledge of physics, chemistry, engineering (electric and mechanical) et al. There are still unknown subject areas in exact discharge coupling processes and chemical kinetics simulations. The prospect of gaining insight into the systematic integration of electrodynamics and combustion chemistry is a challenge, which this dissertation explores.

The use of electromagnetic energy and nonequilibrium discharge in particular for enhancing ignition and combustion stability is receiving great attention due to the potential for enabling highly efficient thermal energy conversion, reliable ignition in

harsh operating conditions, flammability limit extension, reaction with alternative fuels of different burning characteristics [2, 3], and for the development of next generation propulsion systems using hypersonic flow [4, 5]. From a future application perspective, a light-weight power supply and a discharge unit be integrated into a practical combustion system, and the generated nonequilibrium discharge must target energy transfer to efficiently boost the combustion chemistry.

The exact mechanisms for flame enhancement by plasma (either thermal or nonthermal) are being actively studied. A number of studies have provided a glimpse into various aspects of this process [6-12]. In the literature, the electromagnetic energy alters the reaction chemistry by: (1) increased flame temperature by ohmic heating; (2) radiation-induced excitation of electrons; (3) decomposition and breakup of the fuel molecule to smaller hydrocarbon molecules, including in-situ fuel reforming; and (4) creation of radicals via collision with electrons creating an increase in electrons, ions and excited state species. Dr. Starikovskii has written an extensive review of the progress on plasma assisted ignition and combustion in [2].

Another aspect of evaluating a combustion system is the level of emissions. A practical system requires low or even zero emissions of pollutants while coupling high temperature reactive flows (combustion) with a plasma discharge, especially for high power. This can lead to significant changes in the formation of  $NO_x$  (95% is nitric oxide). Nitric Oxide is one of the most hazardous combustion products and constitutes a critical design parameter for practical combustion systems using air as the oxidizer. Generally,

*NO* in conventional combustion forms from the following four main path ways [13, 14]: (1) thermal (Zeldovich) mechanism; (2)  $N_2O$  mechanism; (3) prompt *NO* mechanisms; and (4) fuel-bound nitrogen mechanism (This will be discussed in detail later in this dissertation). Aside from formation of *NO*, reduction of *NO* in combustion can be achieved by reacting with excess hydrocarbon radicals in a rich flame through a ‘*NO* reburn’ process [15]. In a rich flame, small excess hydrocarbon molecules can generate a large reduction of *NO*. In the case of plasma assisted combustion, atomic and molecular excited states and radicals reactions also play a critical role in the formation and reduction of *NO* [16, 17].

## **1.2 Recent Progress on Plasma Assisted Combustion**

Early work on plasma interaction with combustion focused mainly on interactions involving combustion and electric fields, not combustion with an actual discharge. Combustion with a direct current (*DC*) electric field can lead up to 100% in the blowout limit [18], which may come from an “ionic wind” between the “chemi-ionized” species and the applied electric field in the flame reaction zone. A more significant increase in the blowout limit was observed in [19] using 3 *kV DC* voltage. Investigations were also made using alternating current (*AC*) [20] and the enhancements were marginal compared to the results using *DC* power.

In recent decades (especially the past 10 years), several research groups (*US*, *Russia*, *EU*, *Japan* et al) have made intense efforts to examine plasma enhanced combustion from

different angles using various plasma discharge systems. The exact mechanism for flame enhancement using a discharge is still unclear and is being actively studied, but many studies have provided insights into different aspects of this complicated process [6-12]. Different kinds of plasma discharges, including thermal plasma [21], nanosecond pulsed discharge [22], dielectric barrier discharge [8], pulsed corona discharge [23], RF discharge [24], gliding arc [25], DC or low frequency AC discharges [26], plasmatron [27] and microwave discharge [28] have been investigated for enhancing high temperature thermal oxidation.

For this study, I will summarize some of the published results from various groups. Please note that these only comprise a fraction of the researches on plasma assisted combustion.

Cappelli et al. at Stanford University, investigated three different types of nonequilibrium plasmas used for comparison of flame stabilization in a lifted jet diffusion flame of methane-air: single electrode corona discharge (*SECD*); dielectric barrier discharge (*DBD*); and ultra-short repetitively pulsed discharge (*USRD*, pulse duration of about 10 ns) [8, 29]. It was shown that the flame can be stabilized using *SECD* discharge at a 20% higher co-flow speed than without *SECD*. The blow-off velocity with the *DBD* discharge was increased by up to 50%, and the *USRD* discharge increases the blow-off velocity by nearly a factor of ten, as shown in Figure 1.1.

It was shown by Kim et al. that significant increases in the critical co-flow velocity (the velocity at which flame will extinguish) [8] and the rate of *NO* [29] production in

plasma assisted combustion flames were obtained from ethane-air using repetitively pulsed nanosecond plasmas. The lifted jet diffusion flames were created in a vertical wind tunnel with a nozzle oriented parallel to the flow direction producing a co-flow jet. The lifted-off distance is seen to reduce from the case without discharge (shown in Figure 1.2(a)) to with the discharge (shown in Figure 1.2(b)), indicating greater flame stability in the case with plasma discharge.

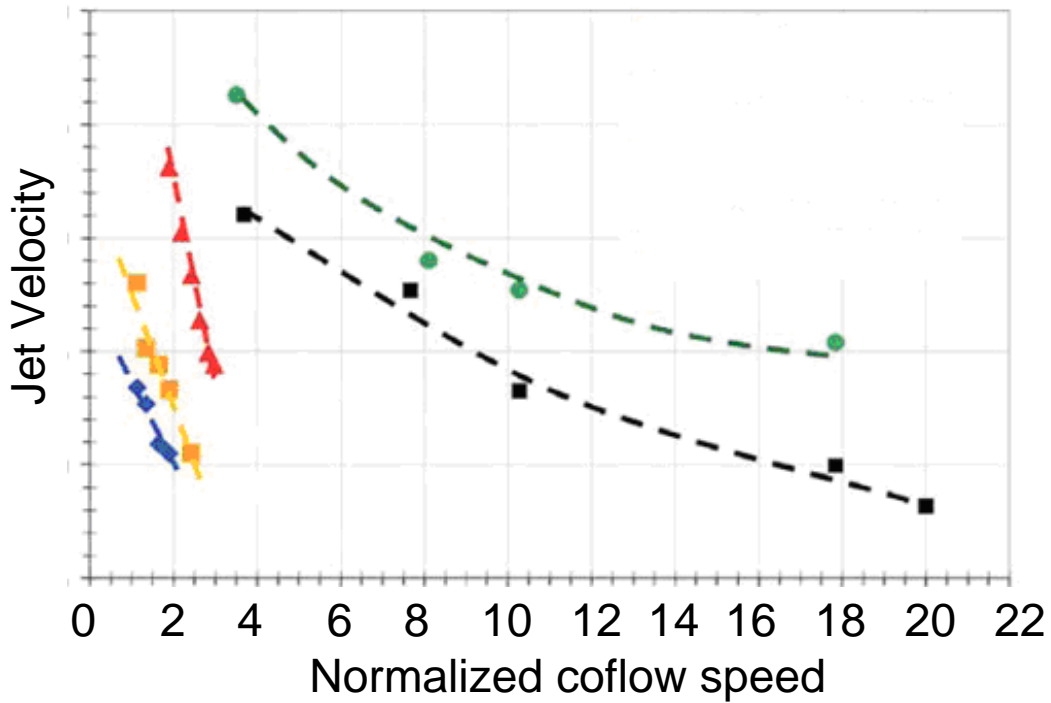


Figure 1.1 Effect of different types of discharge on the maximum co-flow speed (blow-off velocity) [8]. For interpretation of the references to color in this and all other figures, the reader is referred to the electronic version of this dissertation.

Pilla et al. [30] have shown an extension of the flame stability limit in the lean premixed turbulent propane-air flame ( $\phi = 0.3$ ). They compared flame stability using *ICCD* images of *OH* ( $A \rightarrow X$ ) emissions with and without the nanosecond repetitively pulsed discharge. This is shown in Figure 1.3.

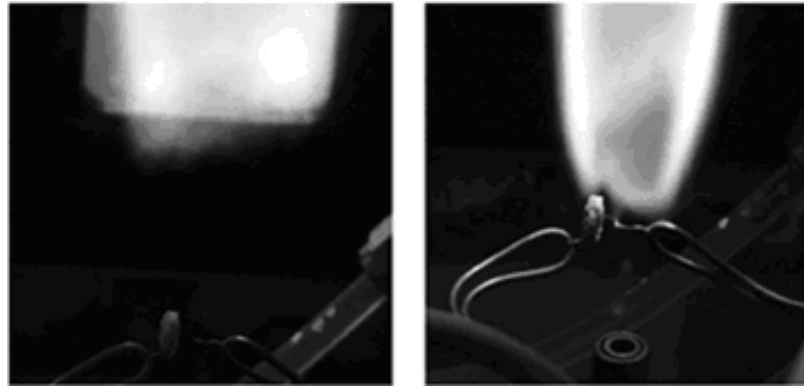


Figure 1.2 Discharge-enhanced flame stabilization. (a) Without discharge. (b) With discharge. The flame is lifted off in (a) and reattached by discharges in image (b). The electrode position is 10 diameters (46 mm) above the nozzle. [8]

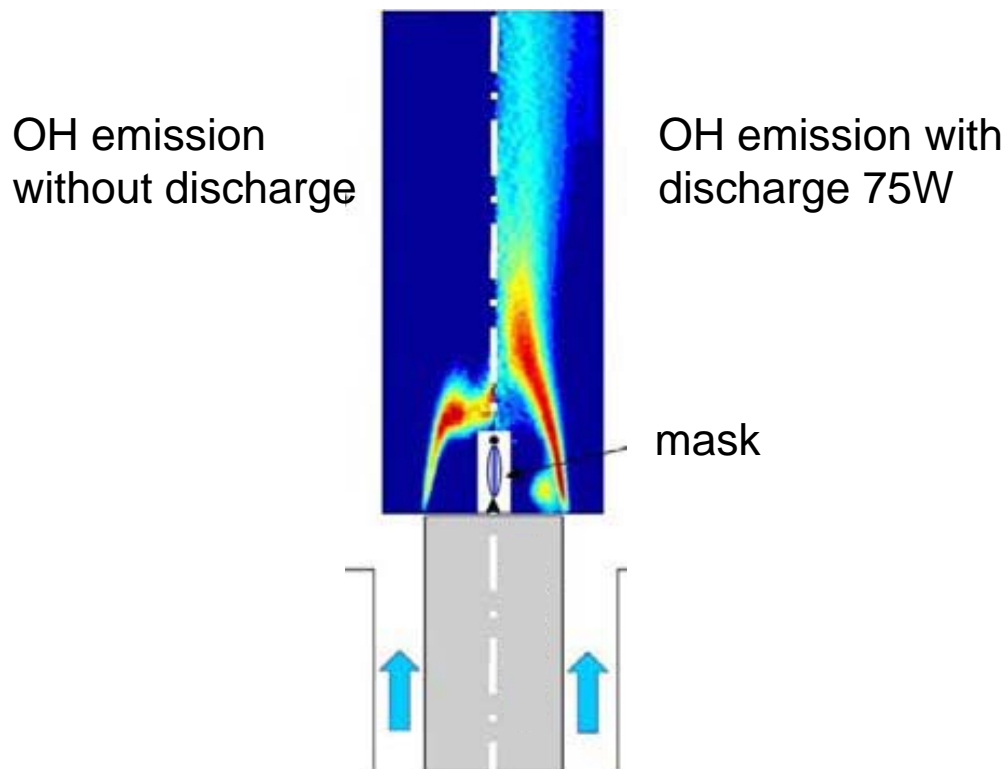


Figure 1.3 Comparison of  $OH$  ( $A-X$ ) emissions with and without discharge [30].

Leonov et al. [4, 5] at the Institute of High Temperature of the Russian Academy of Science investigated a  $DC$  discharge between separately ballasted pin electrodes using a

supersonic air flow to ignite the fuel (a hydrogen and ethylene mixture) which is injected into the flow in a cavity. The schematic of the experiment is shown in Figure 1.4. The Mach number of air flow is  $M=2$  with the initial static pressure ranging between 0.2 to 0.8 bars. The fuel injectors installed on the bottom wall of the cavity (the in Figure 1.4). The discharge is a filamentary *DC* discharge with input power in range 1-10 *kW*.

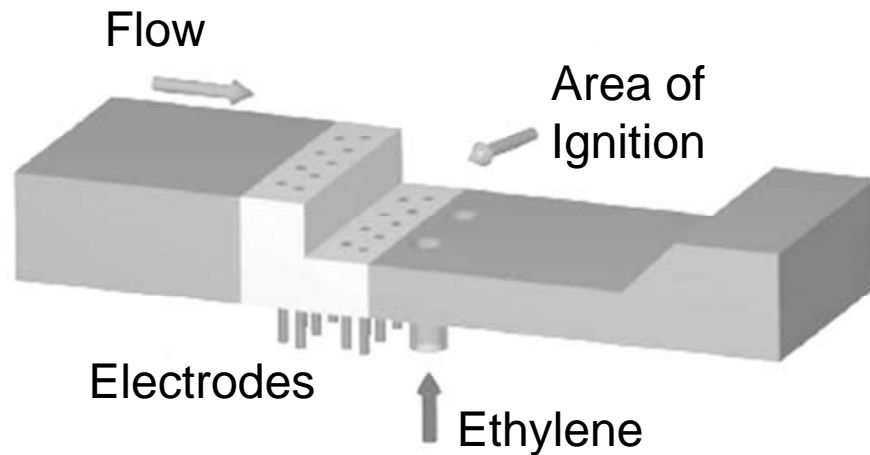


Figure 1.4 Schematic of plasma-assisted combustion experiment in a supersonic flow [5].

Experiments show that at discharge power greater than 1 *kW*, ignition of hydrogen and ethylene occurs. When the discharge power greater than 3 *kW* with the equivalence ratio greater than 1, the flame extended above the cavity as shown in Figure 1.5. In all these experiments the flow rates of the fuel are high, up to 4 *g/sec*.

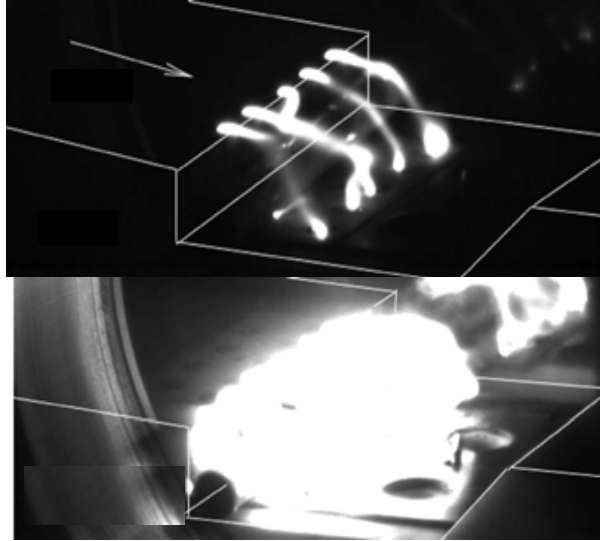


Figure 1.5 Photograph of the discharge in air (top) and of the discharge/flame region in ethylene-air (bottom) [4].

At Princeton University, Ju et al. tested a non-equilibrium Magnetic Gliding Arc (*MGA*) discharge plasma for enhancement of hydrocarbon-air and hydrogen-air counter-flow flames in diluted nitrogen [6, 31]. They showed that the strain rate at extinction in methane-air flows was significantly increased with plasma sustained in the air flow, up to 220 percent at a low discharge power of about 78 *Watts*. Ju et al. suggested that this was predominantly from thermal effects. However, it is also mentioned that excited species generated by the plasma contribute to the enhancement of combustion. Reduction of the ignition temperature by the plasma was both achieved experimentally and numerically with 20% Methane in Nitrogen for preheated air in a Magnetic Gliding Arc as shown in Figure 1.6 [6].

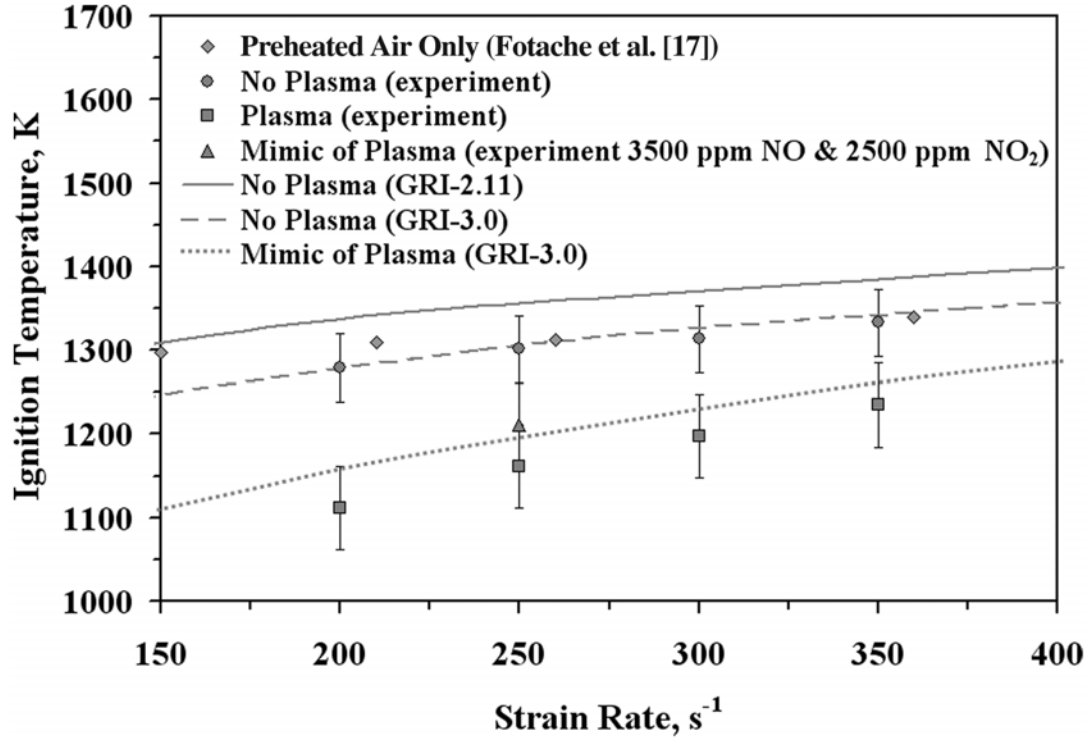


Figure 1.6 Experimental and computational results of ignition temperatures with 20% methane in nitrogen with preheated air in a MGA ( $I = 350 \text{ mA}$ ) [6].

Enhancement of the lifted flame speed by plasma excitation of oxygen (including  $O_3$  and  $O_2(a^1\Delta_g)$ ) by was studied T. Ombrello and et al. [7]. They isolated two oxygen containing species produced by plasma and investigated their influence on plasma enhanced combustion in order to isolate various flame enhancement mechanisms. Lifetimes of plasma produced species are shown in Figure. 1.7 as a function of pressure. From the figure, they also obtain some rough pressure ranges for a practical system (internal combustion engine, gas turbine, etc.). It is clear that stable species ( $NO_X$  and  $O_3$ ) have the highest lifetimes whereas electrons and ions have the lowest. The lifetimes of the radicals and some metastables ( $O$ ,  $OH$ ,  $H$ ,  $O_2$ ,  $a^1\Delta_g$ , etc.) and excited species and other metastable species ( $O(^1S)$ ,  $O_2(v)$ ,  $N_2(v)$ , etc.) are in between, with the lifetimes of

the former being higher. The results show significant kinetic enhancement by  $O_2(a^1\Delta_g)$  and  $O_3$  when comparing flame stabilization locations with or without the extra species generated by the plasma. The enhancement of the lifted flame speed by  $O_3$  is shown in Figure 1.8. With  $\sim 500$  ppm  $O_3$  addition,  $\sim 2\%$  enhancement is achieved while with  $\sim 1,300$  ppm, it is 8%. The experiments were also conducted under different pressure ranges.

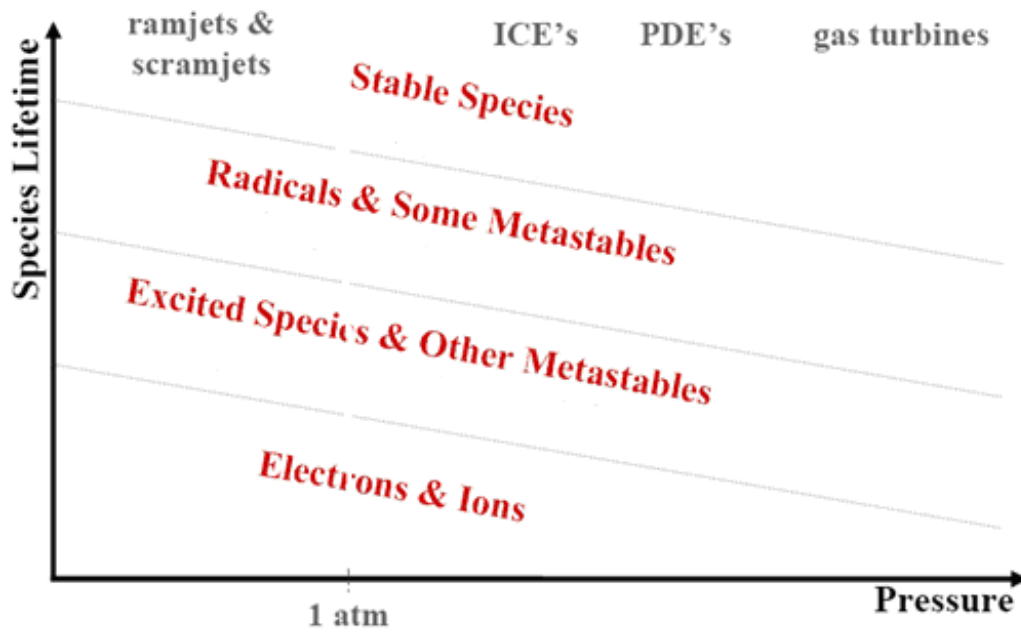


Figure 1.7 Lifetimes of plasma produced species as a function of pressure. [7]

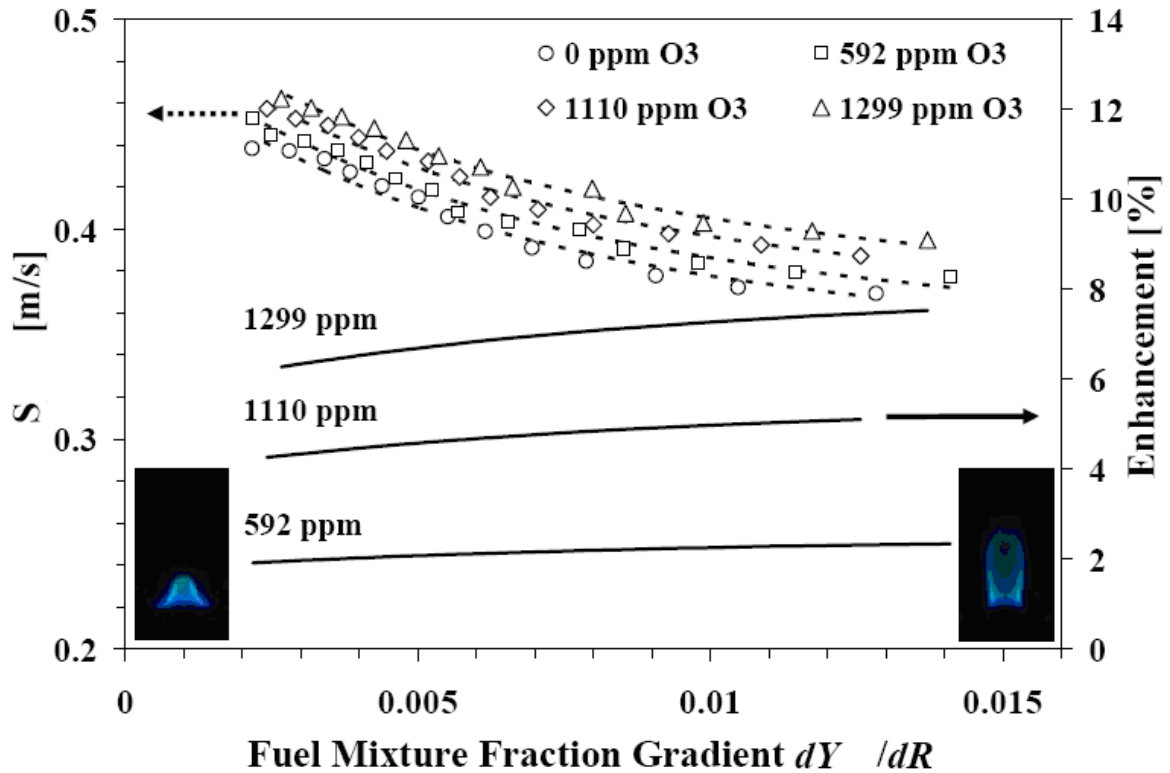


Figure 1.8 Lifted flame speed enhancements by addition of  $O_3$  at 1 atmospheric pressure [6].

Miles, et al. in Princeton studied microwave induced flame speed enhancement in a laminar, premixed  $CH_4$ /air wall stagnation flat flame in a high- $Q$  microwave cavity [12]. When the flame is activated by a continuous wave microwave field of about  $5\text{ kV/cm}$ , the flame front approaches the burner exit and stabilizes at a standoff distance with a flame speed increase of up to 20%. The temperature was measured using Rayleigh scattering thermometry, the laminar flame speed was measured using Particle Image Velocimetry (PIV), and the  $OH$  radical concentration was measured by laser induced fluorescence. Images of  $OH$ -LIF signal intensity for an equivalence ratio of 0.76  $CH_4$ /air flame without (a) and with (b) microwave radiation are shown in Figure 1.9. The authors indicate that

microwave radiation can be practical means to control and enhance flame stability non-invasively.

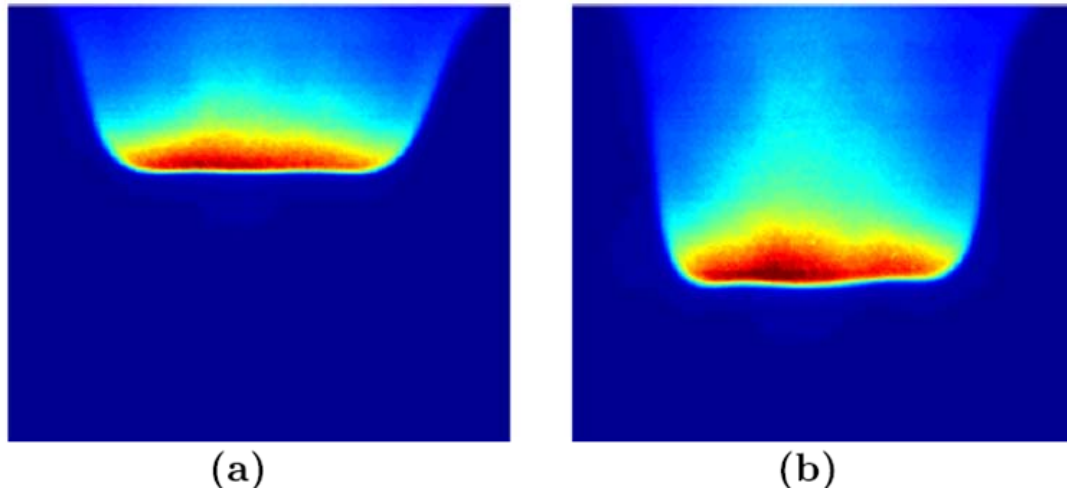


Figure 1.9 Images of  $OH$ -number density in equivalence ratio of 0.76  $CH_4$ /air flame without (a) and with (b) microwave radiation.[12].

A gliding arc ( $GA$ ) discharge system was used by Fridman et al. for flame enhancement research [32]. The study showed combined advantages of both thermal and non-thermal discharges for certain applications in optimized  $GA$  regimes. This discharge, as a source of intermediate plasma, is a promising way to modify important plasma chemical process (a plasma partial oxidation of methane). The authors compared this kind of discharge with a microwave discharge. The gliding arc discharge has unique advantages in that it is not restricted by pressure, which has limited the actual application of the microwave discharge.

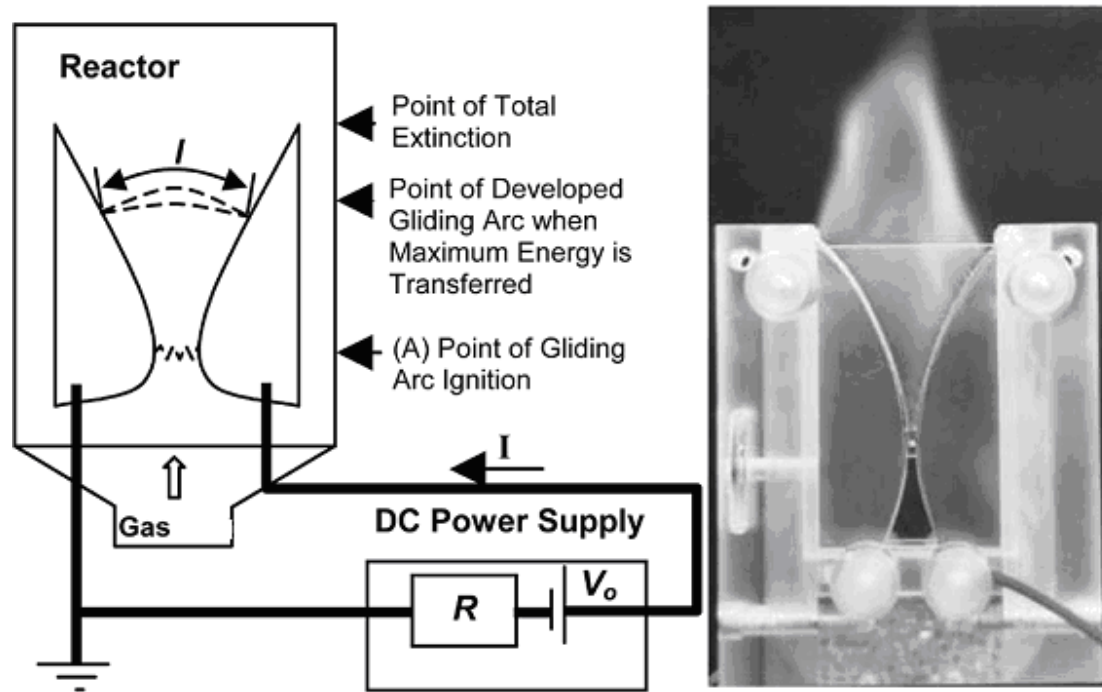


Figure 1.10 Schematic of gliding arc and the electric components (Left). Photo image of *GA* discharge (Right) [32].

Starikovskii et al; also in Drexel University studied plasma-assisted ignition below the self-ignition threshold for different fuel-air mixtures (including methane, ethane, propane and butane) [33]. A series of *ICCD* images is shown in Figure 1.11 with the plasma developing between two electrodes over a short time period. The ambient temperature for ignition is between 300 and 800  $K$  which is well below the auto-ignition temperature for most of the fuels. Laser-induced fluorescence was utilized to measure the *OH* concentration after the discharge. The *OH* profile shows that the *OH* concentration persists at a significant level after plasma discharge generation for a long time. The time increases with increasing temperature.

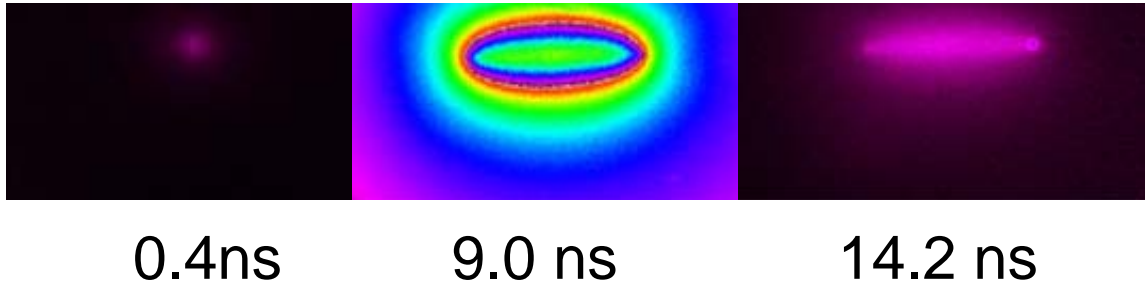


Figure 1.11 ICCD images of plasma discharge development (camera gate time is 200 ps. One atmospheric pressure,  $U = 20 \text{ kV}$ ) [33].

Lou et al. [23] (shown in Figure 1.12), and Bao et al. [34] (Figure 1.14) investigated ignition and almost-complete combustion in low temperature oxidation of methane and ethylene in air at  $P=70$  to  $90 \text{ torr}$ , at the conditions when the temperature for repetitively pulsed air plasma before fuel was addition ranged from  $100 - 200 \text{ }^\circ\text{C}$ . Pictures of the discharge in air, and in methane/air mixtures, are shown in Figure 1.13 with flow from left to right. A flame through a rectangular window is observed in the picture on the right.

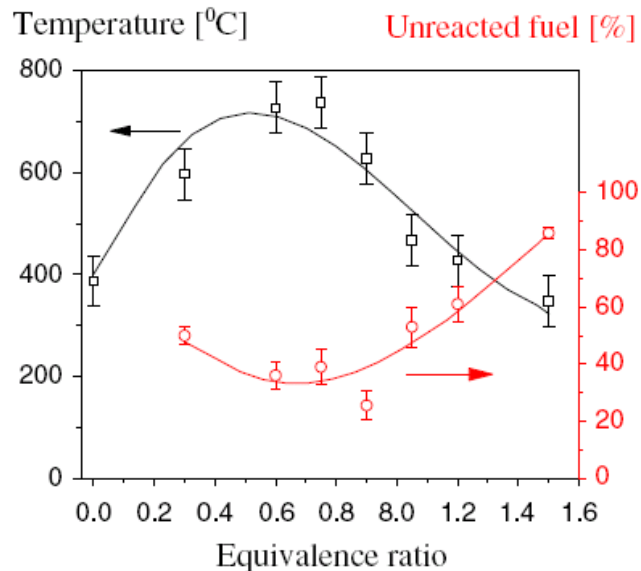


Figure 1.12 Flow temperatures (left  $Y$  axis) and unreacted fuel fraction (right  $Y$  axis) downstream of the discharge versus equivalence ratio in flow mixed with methane and air. Pressure is  $100 \text{ torr}$  with no flame detected in the test section. [23]

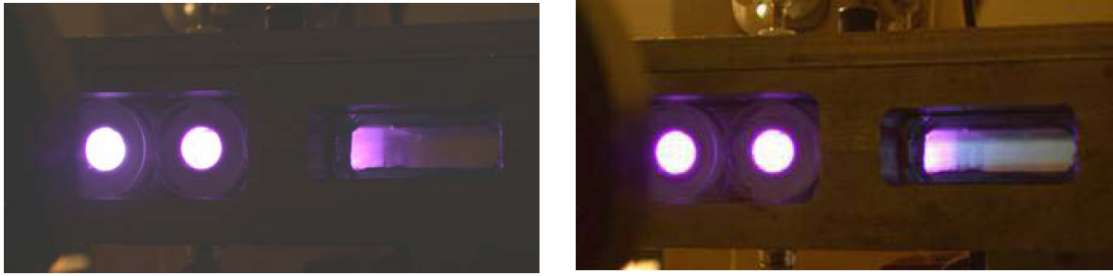


Figure 1.13 Images of plasma combustion, 70 torr total pressure in air (left) and  $C_2H_4$ /air at equivalence ratio of 0.9 (right). [23]

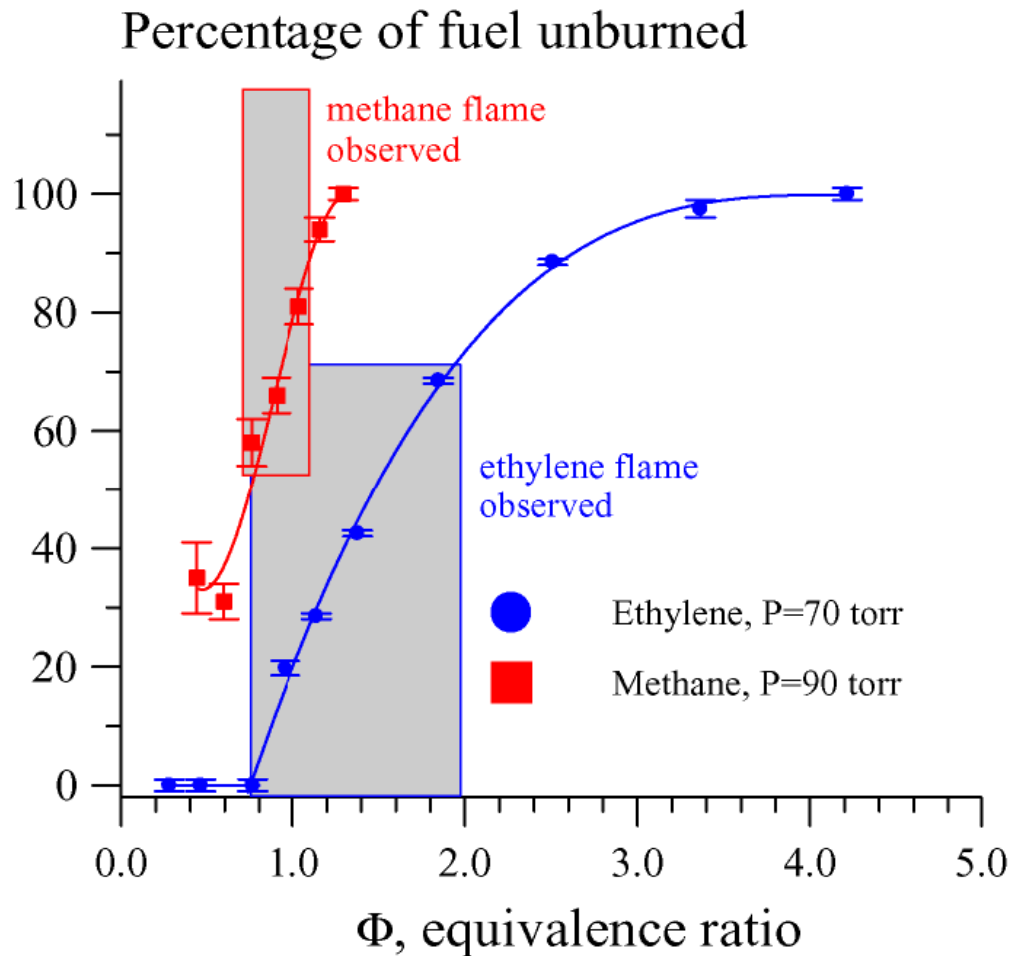


Figure 1.14 Percentage of fuel left which is unreacted in the flow in a transverse  $RF$  discharge with shaded areas indicating conditions when flame occurs. [34]

Temperatures of the air and air/ ethylene flow with respect to percentage un-reacted flow and flow velocity are shown in Figure 1.15(left) and (right) [35], respectively. Unburned percentage of fuel indicates the completeness of oxidation using the discharge for different equivalence ratio for 70 torr and 90 torr with both methane and ethylene. Please note here under some conditions there is flame while under others there isn't.

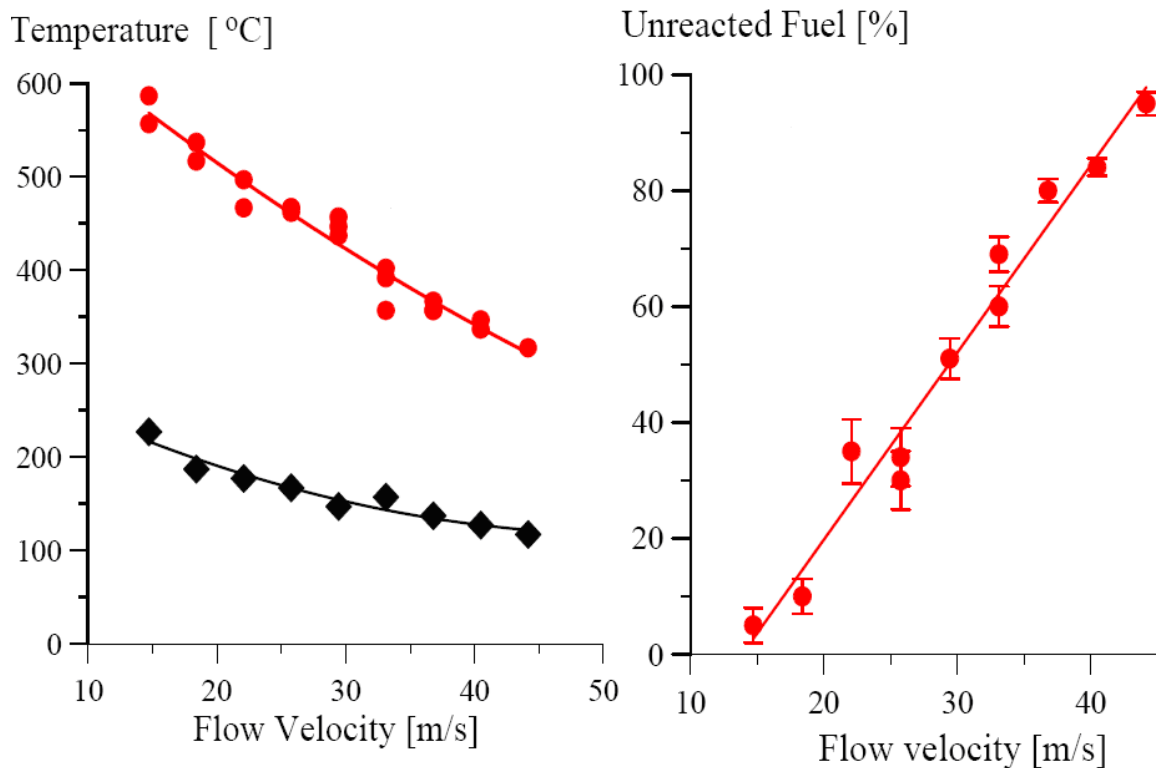


Figure 1.15 Discharge temperature (a) and unreacted fuel fraction (b) as functions of flow velocity. Ethylene/air, P=70 torr,  $\phi=1.0$ , pulser rep rate 50 kHz. Closed symbols indicate ignition is achieved [35].

### 1.3 Scope of Research

The goal of this dissertation is to examine energy-efficient and effective flame enhancement with reduced pollutant emissions by a plasma discharge. Two discharge

systems are investigated: (a) direct current (*DC*) plasmatron; and (b) microwave (*MW*) re-entrant cavity discharge system. Two combustion configurations, a premixed methane/oxygen flame and a premixed methane/air flame are also tested and reported. The scope of this research can be summarized by the following four fundamental questions:

1. By how much can plasma enhance combustion? What constitutes efficient kind of plasma delivery system?
2. How does a plasma discharge enhance a flame – i.e. what are the roles of radicals, thermal effects, and non-equilibrium kinetics?
3. What differences exist between premixed and non-premixed plasma assisted flames?
4. What are the  $NO_X$  production mechanisms and how to reduce  $NO_X$  production using high electric power?

The dissertation is organized as follows: Chapter 2 introduces basic knowledge on laser induced fluorescence and the computational simulation of Nitric Oxide. Chapter 3 describes the experimental facilities and diagnostics setup used. Chapter 4 discusses the results of combustion dynamics using a microwave cavity applicator here. Chapter 5 presents the results of premixed and nonpremixed combustion in a *DC* plasmatron. Chapter 6 presents *NO* formation and reduction in the *DC* plasmatron. Finally, Chapter 7

summarizes the results of the present work and offers some suggestions for future work suggestions.

## Chapter 2 Spectroscopy

### 2.1 Laser Induced Fluorescence (LIF)

Spectroscopy was originally used to study of the relations between radiation and matter. Spectroscopy used to be referred to disperse visible light of its corresponding wavelength, e.g. using a prism. Nowadays spectroscopy is expanded to include measurements using either wavelength or frequency, thus it can be also referred as the responses to varying frequency or an alternating field. After the relationship of energy with wavelength was realized,  $E = h\nu$ , spectroscopy was also related to energy. The spectrum is a plot with wavelength or more commonly frequency or energy.

Spectrometry is a spectroscopic technique used to investigate a specific species (atoms, molecules, ions). The instrument used for spectrometry is called a spectrometer, spectrograph, or spectrophotometer. Spectroscopy (spectrometry) is often used in physical and analytical chemistry for the quantification of substances through their absorption or emission spectra. This technology is heavily used in area of astronomy as most large telescopes have a similar function as spectrometers. In these areas, spectrometry is not only used to measure the physical and chemical properties of astronomical targets but also used to measure their velocities using the Doppler shift of the spectral lines.

Laser-Induced Fluorescence (*LIF*) is a well-established optical technique in many areas of science. It is especially useful in combustion because it can withstand harsh conditions and doesn't disturb the chemical reactions or the flow field. As *LIF* is both species and quantum state selective, this enables measurements of not only concentration, but also temperature, density, pressure, velocities and reaction chemistry. In combustion, *LIF* has also been widely used for the measurement of species (*OH*, *CH*, *NO* and *CO* among others) in reacting flows and flames. Planar *LIF* imaging (*PLIF*) has become an effective tool for 2-D imaging of chemical species concentrations and temperature fields. The historical progress of *LIF* is described in these review articles [36-39].

*LIF* can be understood as a two-step process as in the name: Laser Excitation and Fluorescence. First, molecules are excited to exact higher energy states by the absorption of a photon from the laser with the same wavelength. After a certain length of time, the excited molecules de-excite back to the ground state along both radiative and non-radiative pathways. Among these two pathways, the *LIF* signal comes from radiative relaxation with the excess energy released in the form of fluorescent light. Non-radiative de-excitation always happens with *LIF*: its impact is important for deducing quantitative results from the *LIF* signal.

To provide insight into such complicated process, a two-level model is introduced [40, 41]. A schematic of the model is shown in Figure 2.1 with transitions from two electronic energy states of a typical diatomic molecule.

This two-level model is based on following four assumptions to serve to the complicated process [42]:

1. Laser beam for excitation is uniform and linear in polarization;
2. The entire population of molecules is in the electronic ground state before excitation;
3. The fluorescence light is measured at the maximum of the emission pulse and the upper excited level population is in the steady state.
4. The emission fluorescence signal is of one single wavelength which corresponds to a single rovibronic transition.

With these assumptions, this model consists of four processes (absorption, stimulated emission, spontaneous emission, and collisional quenching) with four rate coefficients. A more accurate model with practical physics and energy distribution levels of actual diatomic molecules used the approach with quantum-mechanical density-matrix [41, 43]. In practice, the two-level model can be used as a rough approximation in quantification of *LIF* results.

There are some rules for electronic transitions in diatomic molecules:

- $J$  (quantum number of the total angular momentum):  $\Delta J = +1, 0, -1$  and  $J = 0$  to  $J = 0$  is forbidden
- Symmetry of the molecular system:  $+ \leftrightarrow -$  ( $Q$  branches:  $e \leftrightarrow f$ ;  $P$  branch:  $e \leftrightarrow e$ ;  $R$  branch:  $f \leftrightarrow f$ )

- $A$  (quantum number from the electron orbit angular momentum)  $\Delta M = +1, 0, -1$
- $S$  (Quantum Number for total Electronic Spin):  $\Delta S = 0$

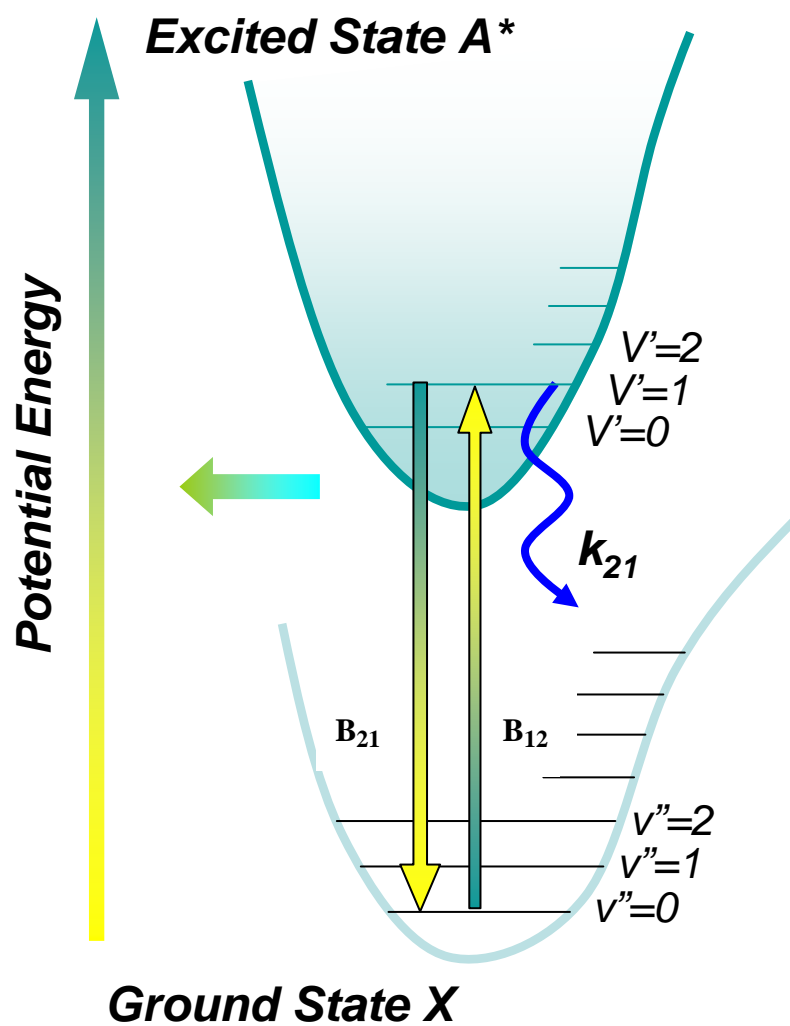


Figure 2.1 Two-level system with pertinent energy transfer processes

Transitions of  $NO$ , through either absorption or emission, between the electronic states  $A^2\Sigma^+ - X^2\Pi^+$  are usually observed in the  $UV$  range, and are traditionally called the  $NO$   $\gamma$  bands.

All the following processes can happen during the excitation and de-excitation of the target molecule. We will discuss their relations with  $LIF$  signals.

- *Stimulated Absorption* of excitation laser photon: the molecule excited from the ground state into the upper excited state. The absorption rate  $B_{12}$  is proportional to the laser spectral irradiance and Einstein coefficient.
- *Stimulated Emission*: the excited molecule relaxes from the upper excited state into the lower ground state and emits a photon.
- *Spontaneous Emission* (also Fluorescence): a photon emits with energy decreasing from the excited state into the ground state.
- *Simultaneous Excitation*: more than one ground state level is excited due to the overlap function of broadened absorption. *NO* in particular has a dense absorption spectrum. Moreover, under high pressures conditions, the widths of collisional lines can expand to many wave numbers, causing different pairs of states to participate in the overall *LIF* process.
- *Spontaneous Emission*: fluorescence from the laser excited higher energy state into other lower electronic energy states.
- *Photoionization*. Photoionization happens when a molecule absorbs a second photon on top of the excited state with its overall process main part of Resonantly Enhanced Multi-photon Ionization (*REMPI*) spectroscopy.
- *Rotational Energy Transfer (RET)*: If the target molecule collides with another one, its rotational state may alter. Since *RET* is a fast process, having the same time scale as the laser induced fluorescence processes, it then has critical implications on *LIF* dynamics. While molecules are continuously pumped from a lower energy state to a

higher state by the laser, and continuously de-excited, which perturbs the thermal equilibrium, *RET* in both states keeps on refilling and depleting these two laser related states to reestablish rotational equilibrium.

- *Vibrational Energy Transfer (VET)*. Similarly if the target molecule collides with another molecule, its vibrational state may alter. *VET* establishes and maintains vibrational equilibrium. *VET*, however is often less effective than *RET*.

- *Quenching or Electronic Energy Transfer (EET)*: Similarly if the target molecule collides with another molecule, its electronic state may alter. The higher excited electronic state is likely to relax to a ro-vibronic level of the ground electronic state after collision.

*RET* and *VET* keep the molecule remain in the electronically excited state, therefore leaving the possibility of fluorescence, while *EET* disables the fluorescence as it prohibits the fluorescence of the molecule. Therefore *Quenching/EET* is a direct and usually most important competitor to the *LIF* process.

Rate coefficients of absorption and stimulated emission rates are  $B_{12}$  and  $B_{21}$ , respectively. Quenching rates are  $k_{21}$  with spontaneous emission rates using  $A_{21}$ . The total molecule number density is  $N=N_1+N_2$ , with  $N_1$  and  $N_2$  representing the population number density in states 1 and 2. The energy density for excitation laser is  $\rho_\nu$ . The population of each energy state can be written as

$$\frac{dN_1}{dt} = -\rho_v B_{12} N_1 + (\rho_v B_{21} + k_{21} + A_{21}) N_2, \quad (2.1)$$

and

$$\frac{dN_2}{dt} = -\frac{dN_1}{dt} = \rho_v B_{12} N_1 - (\rho_v B_{21} + k_{21} + A_{21}) N_2, \quad (2.2)$$

The number of fluorescence photons  $N_f$  can be obtained as an integral over the duration  $\tau$  of laser excitation:

$$N_f = A_{21} \int_0^\tau N_2(t) dt, \quad (2.3)$$

If the excitation laser pulse function is a perfect square pulse, then the exact solution to Equations (2.1) to (2.3) is:

$$N_f = A_{21} \tau \cdot N \cdot \frac{\rho_v B_{12}}{\rho_v (B_{21} + B_{12}) + k_{21} + A_{21}} \left( 1 - \frac{1 - \exp\{1 - [\rho_v (B_{21} + B_{12}) + k_{21} + A_{21}] \tau\}}{[\rho_v (B_{21} + B_{12}) + k_{21} + A_{21}] \tau} \right), \quad (2.4)$$

Equation 2.4 is too complicated to analyze. To simplify the problem and quantify for the laser fluorescence signal used here, let us consider the steady state case. In the steady state, the population of both states remains the same, thus the derivative of the number density on each energy state is zero. Consider that there is degeneracy in each energy state, then Equation 2.4 can be simplified as follows (the degeneracy for each state is  $g_1$  and  $g_2$ ):

$$N_f = \frac{g_2}{g_1 + g_2} \frac{\rho_v B_{12}}{\rho_v B_{12} + \frac{g_2}{g_1 + g_2} (k_{21} + A_{21})} \cdot A_{21} \tau N, \quad (2.5)$$

The denominator has two terms. The first,  $\rho_v B_{12}$ , is related to rate of molecule excitation; the second term relates to quenching and emission rate coefficients. Depending on excitation laser intensity, two different limit cases are possible:

(1). Linear Regime. When  $\rho_v B_{12} \ll k_{21} + A_{21}$ , which means the laser intensity is low, one obtains

$$N_f = \frac{A_{21}}{k_{21} + A_{21}} \rho_v B_{12} \tau N = \phi \rho_v B_{12} \tau N, \quad (2.6)$$

The number of fluorescence photons is linearly proportional to the excitation laser intensity, which means that in this case signals must be calibrated for fluctuating laser intensities. The term  $A_{21}/(k_{21} + A_{21})$  in this equation is the fluorescence yield ( $\phi$ ), with the definition of the ratio of the spontaneous LIF emission rate to all de-excitation from excitation rates. Fluorescence yield is also a direct display the percentage of the excited molecules which will actually fluoresce.

(2). Saturation Regime. When  $\rho_v B_{12} \gg k_{21} + A_{21}$ , which means the laser intensity is high,

$$N_f = \frac{g_2}{g_1 + g_2} A_{21} \tau N, \quad (2.7)$$

In this case, the fluorescence signal is independent of the excitation laser intensity. In practical diagnostics application, this case is called the *laser induced saturated fluorescence* or *saturation spectroscopy*. Here the fluorescence signals are independent of the laser intensity. But, the very high laser intensities for saturation LIF require careful experimental attention. What is more, complete saturation is hard to achieve, especially at elevated higher pressures.

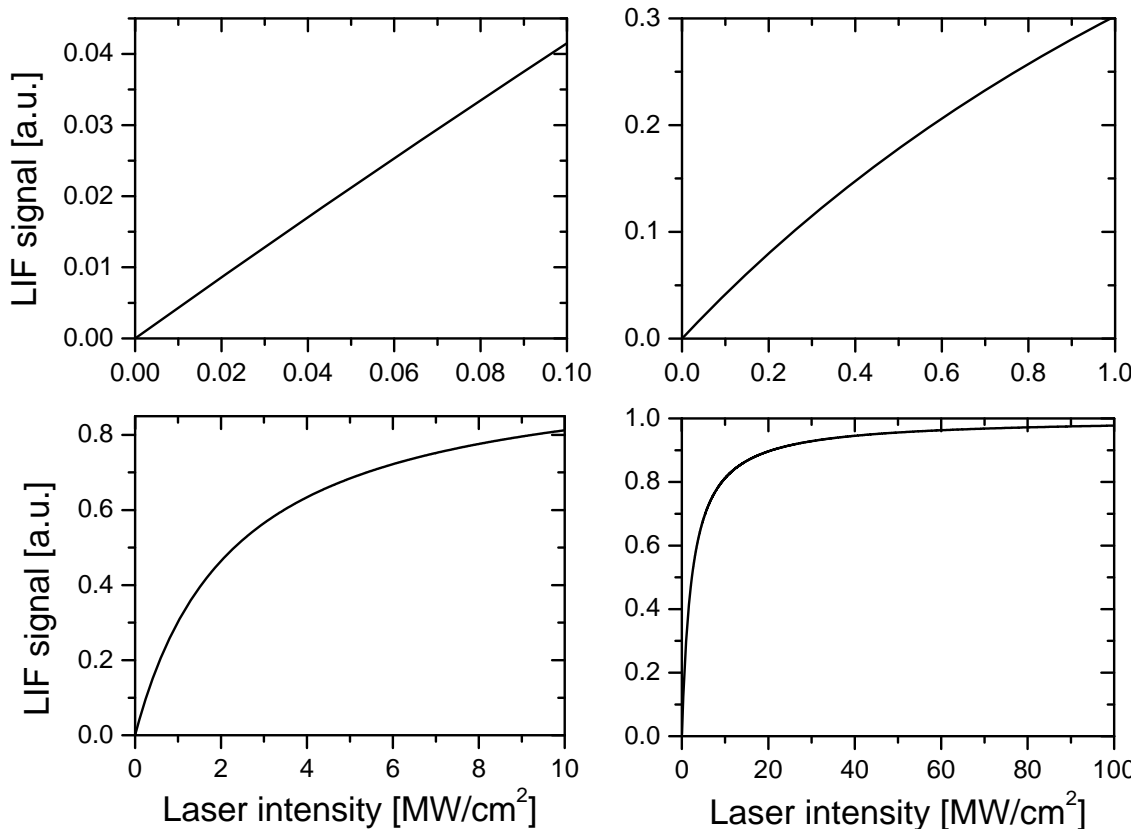


Figure 2.2 Transition from linear regime to saturation regime in the non-transient two-level model in a 1 bar, equivalence ratio 0.9 methane/air flame. A difference for four figures is the different laser intensity scales [44].

Figure 2.2 shows LIF signals over a different ranges of laser intensity calculated using the non-transient two-level model discussed below by Bessler [44]. It is clear that

the linear and saturation regimes are extreme cases for lowest and highest laser intensities. The highest signal intensity in the full linear range is only about five percent of the signal intensity at full saturation regime. In reality, transitions between these two cases were observed. In this research, all data is presented in the linear description, in which interpreting of the *LIF* signals is easier. It is also noted here that Rotational Energy Transfer (*RET*) in both states might change the saturation regime dramatically, especially during the extended linear ranges.

To sum, the *LIF equation*, from the key physics involved in the *LIF* process, can be derived from a non-transient analysis of the two-level model. The *LIF* intensity can be written as the following in Equation 2.7.

$$I_{LIF} = c \times I_{\nu}^0 \times n_1^0 \times f_B \times B_{21} \times V \times \Gamma \times \frac{\Omega}{4\pi} \times \frac{A_{21}}{A_{21} + k_{21}}, \quad (2.8)$$

Here,  $V$  is the volume,  $I_{\nu}^0$  is the laser intensity,  $c$  is the experimental setup optical collection efficiency and  $\Gamma$  is the dimensionless overlap function [45]. Equation 2.1 is known as the ***LIF equation*** which is a fundamental one to solve for LIF signals between practical experimentation and computational simulations. Values of  $A_{21}$  for  $NO A^2\Sigma^+$  ( $v^{\prime}=0$ ) state are  $\sim 4.6 \times 10^6 \text{ s}^{-1}$  while the quenching rate  $k_{21}$  is on the order of  $\sim 10^{10} \text{ s}^{-1}$ , which leads to a fluorescence yield of about  $10^{-4}$ .  $\Omega$  is the solid angle of collection.

## 2.2 *NO LIF*: Literature Survey

There are some unique advantages to use *NO* as a tracer for *LIF* measurements in combustion. First and foremost, *NO* has a relatively good fluorescence efficiency and a strong absorption cross-section, which lead to strong *LIF* signals for detection. Also, *NO* is a molecule whose spectroscopy is well studied and known. Third, *NO* does not exhibit *J*-dependent or so-called rotational-level dependent quenching rates or radiative *LIF* times that result in systematic measurement errors. Fourth, *NO* emits a strong nonresonant fluorescence signal, which can provide detection strategies without worrying about Rayleigh scattering or radiative trapping when combined with spectral filtering. All of these enable numerical modeling of the *LIF* signal. In addition the modeling has reached a high level of maturity and could provide flexibility in design and interpretation of the *NO-LIF* experiments. Also, *NO* is quite stable in harsh high temperature ( $T \geq 2000\text{K}$ ) and pressure ( $P \geq 30\text{bar}$ ) combustion environments to be a good tracer. Finally, *NO* can be easily seeded into the combustors to make *LIF* measurements in the entire flowfield. This is different from molecules such as *OH*, which are only feasible in the gas mixture reaction regions.

There have been extensive publications regarding *NO-LIF* for both experimental research and practical applications. Perhaps the first report of *NO-LIF* use was by Grieser and Barnes [46]. They used single-point *NO* fluorescence measurements. McKenzie and Gross [47] later reported the use of two-photon *NO LIF* for single-point temperature

measurements. Kychakoff *et al.* [48] reported the first 2-D imaging of *NO* fluorescence of *NO* in *CH<sub>4</sub>*/air flames and also suggested the potential use of 2-D imaging to get temperature. Paul *et al.* first reported two-line *PLIF* thermometry [49]. These references are a small fraction of the *NO-LIF* articles in the literature, and are chosen because of their pioneering contribution.

With the development of new technologies, single laser pulse *LIF* of *NO* for measurement of concentration, temperature, and velocity is well established. There is a need to obtain higher speed images of *NO LIF* to improve image and dynamic behavior of the reacting flow. This requires a high-speed laser system and a high-speed imaging system. Kaminski used four double-pulsed *Nd:YAG* lasers to pump one single dye laser, for *OH PLIF* imaging, resulting in a four times laser frequency and then a four times signal collection rate [50]. Using 270 *mJ* per pulse at 532 *nm* out of *Nd:YAG*, Kaminski and *et al.* generated pulses at 282 *nm* with a averaged energy of about 1 *mJ*/pulse 8 *kHz* repetition rate [50]. Kittler and Dreizler investigated the turbulent flame using UV light at 283 *nm* of about 22 *μJ*/pulse from a dye laser which was excited by a 5 *kHz* *Nd:YLF* pumping laser [51]. Lempert reported an ultrahigh (100 *KHz*) *PLIF* images of *NO* using ultrahigh (100 *KHz*) burst pulses of deep UV of 226 *nm* by mixing the third harmonic laser (355 *nm*) from a burst pulse laser with a 622 *nm* output from an optical oscillator [52]. One important parameter is the energy of the ultrahigh pulse, which in [52] are about 0.5 *mJ* at the 226 *nm* excitation laser, which is sufficient for instantaneous *PLIF*.

A simulation code, *LIFSim* [53], widely used to model *NO-LIF*, is also introduced in

this section. *LIFSim* was developed to conduct numerical simulations of excitation and emission processes in *LIF* (for both *NO* and *O<sub>2</sub>*) to quantify species concentrations and temperature measurements. Several basic criteria must be satisfied to perform quantitative *LIF* measurements. First, the emission spectrum of the molecule for *LIF* should be well known. Second, knowing the absorption spectrum from a practical accessible laser is necessary. Third, non-radiative pathways (besides *LIF* including quenching, predissociation and photoionization) should be understood. Fourth, the rate of excited state radiative decay should be known because the fluorescence power is proportional to this decay rate. *LIFSim* was developed by Bessler (2003, Heidelberg University) which is based on a previous numerical code by Sick (1995). This software is available in a *DOS* shell executable format and also via an interactive web interface ([www.lifsim.com](http://www.lifsim.com)) [53].

Here some examples of *LIFSim* are listed for different purposes.

- 1, Absorption Spectra Calculation: pressure, temperature, excitation wavelength range and resolution are necessary parameters for calculation of absorption spectra.

- 2, *LIF* Excitation Spectra Calculation: excitation wavelength range, pressure and resolution are necessary parameters for this calculation with detection bandpass being a variable.

- 3, *LIF* Emission Spectra Calculation: the monochromater function is calculated depending on parameters provided by the user.

- 4, Temperature and Pressure Dependence of the *LIF* Signal Calculation: pressure

range, excitation wavelength, and temperature range are necessary parameters. The *LIF* signal can also be used for constant mole fraction or number density, which is on a per volume or per molecule basis.

5, Simulated LIF Excitation Spectra Comparison with Experimental Data: this comparison has an adjustment of analysis of fit precision, line positions and accuracy. The relative *LIF* signal strength of the different transitions can show temperature information in a *LIF* excitation spectrum. Temperature is obtained by comparing experimental data with simulated spectra. To obtain correct temperatures from the comparison, the line positions from the simulation are adjusted to data from the experiments. Parameters used in fitting are intensity, temperature and a wavelength-independent baseline. There can be additional parameters used for the fitting, such as laser Lorentzian and Gaussian line width contributions (to evaluate the spectral shape of the laser) and a linear inclination of the baseline (to evaluate extended scans).

## Chapter 3 Experimental Facilities

### 3.1 Microwave Plasma System

#### 3.1.1 Coaxial Re-Entrant Cavity Applicator

A unique coaxial re-entrant cavity applicator was developed for coupling microwave energy directly into the reaction zone. Using microwave power for plasma generation offers a range of benefits including: (1) highly efficient production of radicals and in sustaining a discharge in high-flow gases; (2) ability to operate in thermal and non-thermal modes; (3) ability to sustain good plasma uniformity at atmospheric pressures and higher; (4) electrodeless microwave plasma system; (5) ability to be focused in a specific location and stabilized by gas flows [54]; and, (6) operation in continuous-wave modes (partial non-equilibrium) and pulsed modes (strong non-equilibrium with pulse duration  $< 100\text{ns}$ ). This torch also utilizes many of these advantages including discharge uniformity in a glow mode in the reaction zone at atmospheric pressure when viewed using an intensified *CCD* camera with gate times down to several nanoseconds.

In Figures 3.1 and 3.2 we show the coaxial re-entrant cavity applicator. Figure 3.1 displays a photograph of the system along with an inset picture of a methane/oxygen flame. Figure 3.2 displays the corresponding schematic. The applicator is a brass re-entrant cavity excited in the *TEM* mode [55] (in the current study, the *TEM* 011 mode

[56]) and includes the following components: (1) brass gas tube burner; (2) adjustable endplate; and (3) mono-pole antenna loop. All three adjustments are set by using a micrometer unislide with an accuracy of  $0.01\text{ mm}$ . This redesign of our previous system [57] has a modified tip around the main chamber that enhances focus of the microwave energy into the reaction zone of the flame.



Figure 3.1: Picture of coaxial re-entrant cavity applicator with three fine adjustments using unislides; picture of methane/oxygen flame shown in the inset.

In the bottom portion of Figure 3.2, the setup and components for microwave power supply and measurement system. It is consisted of a power supply, two directional couplers, two power meters with a power sensor and a directional coupler. Two directional couplers and two power meters are used because both incident and reflected power have to be measured and calibrated. This system not only sets up for tuning exact

resonant modes in the cavity but also is used for the calibration of power delivered into the system.

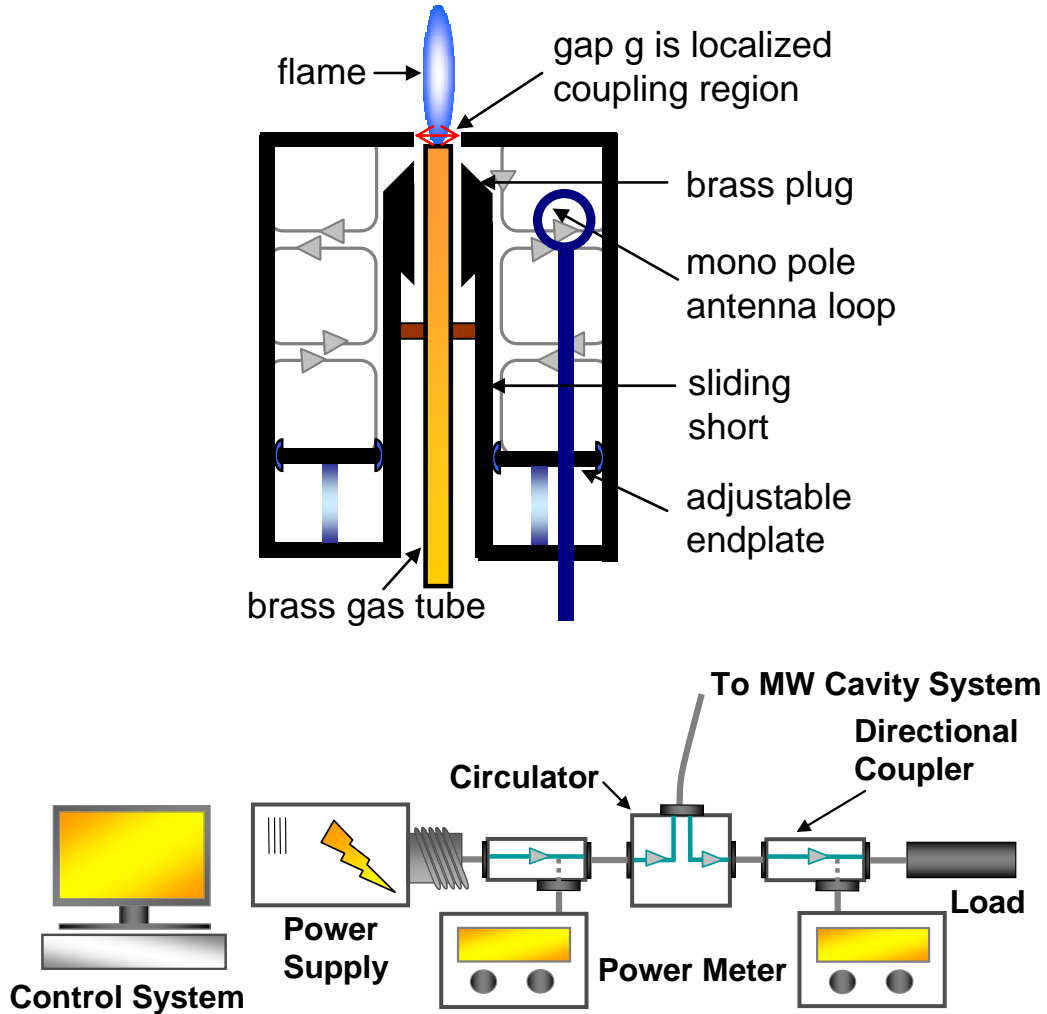


Figure 3.2 Scheme of the structure of coaxial re-entrant cavity applicator with burner centered in the middle (Top). Components of microwave power supply and measurements setup (Bottom).

2.45 GHz microwave energy is transmitted via a coaxial cable and emitted with a mono-pole antenna (Figure. 3.2). When the relative location of the torch, antenna, and baseplate are adjusted using the unislides, an optimized resonant mode can be found when most of the energy is focused into the region between the edge of the outer cavity

and the end of the combustion torch. Further details regarding simulations to optimize the orientation of the electrical field will be discussed next. There are several nearby *TEM* modes that can be accessed by changing the combination of the three way adjustments. We select a mode that allows the center torch to be exposed outside the main chamber, so that the flame is clearly visible and can accommodate laser and optical diagnostics. The chamber itself is 35 *mm* in diameter and is generally optimized to a length of around 3 *cm* ( $\lambda/4$  for 2.45 *GHz*). The chamber is constructed of brass, which can be considered a perfect electrical conductor for simulation purposes.

### 3.1.2 Direct Microwave Plasma Coupling

In the first part of this study, we investigated direct coupling of electromagnetic energy into the reaction zone of an existing premixed flame for the energetic enhancement of combustion chemistry. A practical extension of this concept could be a scramjet engine where electromagnetic energy is coupled into the combustor to extend operation limits during transient conditions or harsh loading. The plasma generation process can be achieved with minimal power, since a high electric field is directly coupled to the electrons created in a hydrocarbon-based flame through chemi-ionization.

It is expected that the combustion-produced electrons are localized to the flamefront and have densities much lower than the critical density ( $<10^{11}/\text{cm}^{-3}$  for 2.45 *GHz* excitation), where the microwave electric fields can freely penetrate the electron gas to accelerate the electrons through a collision cascade process. In this atmospheric flame ( $T_g$

= 2200 to 3300 K) the mean free path (MFP) for the electron–molecule/atom collisions is of the order of 1  $\mu\text{m}$ . The collision frequency for momentum transfer is of the order of  $10^{11}/\text{s}$ . Thus, the microwave electric field will heat the electron gas via elastic electron–neutral collisions, i.e., electron gas heating occurs by a collisional or Ohmic heating process that is governed by the following equation:

$$\langle P_{abs} \rangle (\vec{r}) = \frac{1}{2} \frac{n_{oe}(\vec{r})e^2}{2m_e\nu_m} \left( \frac{\nu_m^2}{\omega^2 + \nu_m^2} \right) |\vec{E}(\vec{r})|^2 \quad (3.1)$$

where  $\langle P_{abs} \rangle (\vec{r})$  is the absorbed microwave power density in  $\text{W}/\text{cm}^3$ ,  $n_{oe}(\vec{r})$  is the electron density in  $\text{cm}^{-3}$  as a function of position  $\vec{r}$  in the electron gas,  $\nu_m$  is the electron–neutral collision frequency for momentum transfer,  $\omega = 2\pi f$  is the angular frequency, and  $\vec{E}(\vec{r})$  is the impressed electric field strength. Typically for our gas temperatures and pressures,  $\nu_m$  is in the order of 10–20  $\omega$ .

When the microwave energy is coupled into the applicator/flame load, electron heating process takes place, and the electron temperature  $T_e$  increases above the gas temperature  $T_g$  ( $T_e > T_g$ ) creating a non-equilibrium plasma. As the microwave electric field and microwave power are increased, the  $T_e$  increases to the level where some electron–neutral collisions are inelastic, producing new radical and excited species. If electric field strengths and power levels are further increased, ionization collisions may also occur. Eventually, the increased electric field strength is sufficient to cause breakdown, resulting first in micro plasmas and then a partially ionized plasma plume in

the reaction zone. The de-excitation of this gas through three body collisions results in the increase in  $T_g$  downstream.

### 3.1.3 Equivalence Circuit and Electric Field Simulation

Figure 3.3 shows an equivalent circuit for the coaxial re-entrant cavity applicator. For simplicity, the microwave losses due to the surface currents on the coupling loop and the applicator are neglected. The circuit consists of a variable length  $L_s-L_g$ ,  $50\Omega$  transmission line, which extends from the sliding short to the gap region. The coupling loop is modeled as an ideal transformer with an  $n:1$  turns ratio and the lumped circuit  $jY_L$ . When the flame is ignited, the gap capacitance is further modified by the presence of the hot neutral gases and the low-density electron and ion gases produced by combustion. Microwave energy is introduced into the applicator by adjusting the applicator to an electromagnetic resonance at the  $2.45\text{ GHz}$  excitation frequency, and then the microwave energy is coupled into the flame via Ohmic heating of the flame electron gas. Detail analysis is shown in [57].

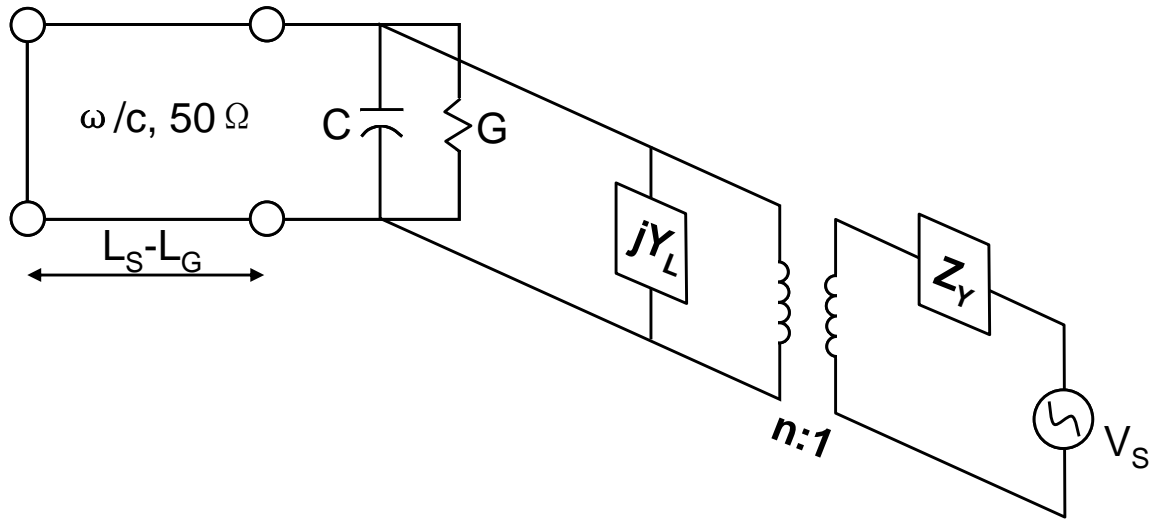


Figure 3.3: Equivalent circuit for coaxial re-entrant cavity applicator

The overall size and geometry of the re-entrant cavity applicator was designed to enable coupling of the microwave energy into the reaction zone of the flame and was based on numerical simulation of the electric field propagation. Figure 3.4 shows a numerical solution of Maxwell's equations using "Rf Electromagnetic Solver" module of the program COMSOL MultiPhysics 3.4. This provided a relative 2-D electric field distribution within the coaxial cavity structure. For our simulations, the medium inside the cavity is air, and all boundaries are set to be perfect electrical conductors. In our experiments, the focus of the electromagnetic energy into the tip of the torch is enhanced as the radicals and the weak concentration of electrons in the flame amplify the coupling process.

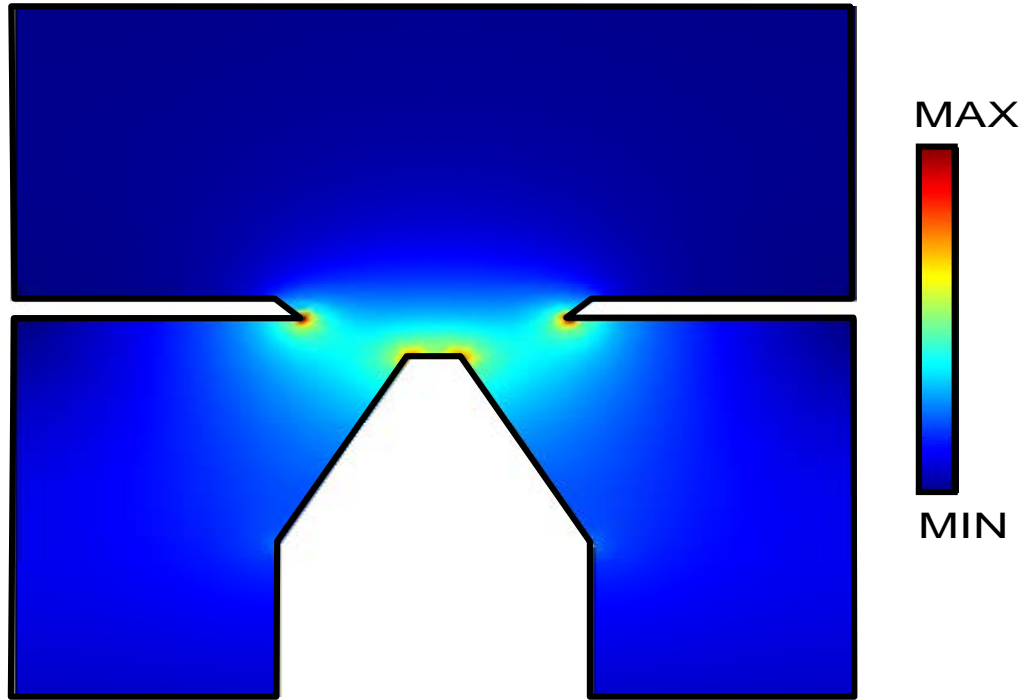


Figure 3.4: Numerical simulation of electric field from ( $V/m$ ) COMSOL MultiPhysics RF Electromagnetic solver for current experiments

The dimensions for simulation are from experimental conditions when plasma discharge is observed with the cavity tuned to resonance at  $2.45\text{ GHz}$  microwave excitation frequency. The  $E$ -field simulation shows an intense electric field at the end of the torch (reaction zone) and the sharp edge of the cavity. In practice, this type of mode can be used to focus the microwave energy when a flame exists on top of the burner exit. The tip of the burner can be raised almost flush with the cavity surface so that the flame is fully exposed for study using optical and laser diagnostics.

#### 3.1.4 Preview Study

A similar microwave cavity applicator with combustion torch burner was investigated by Hemawan at Michigan State University [58]. The components and e-field

pattern are shown in Figure 3.5. The top plate can be moved to change the height of the cavity where the exact mode is created. The sliding short is tuned to the length needed, which is approximately 14.2 cm for *TM012* mode. After putting microwave power into the system and tuning the system directly to *TM012* cavity mode fields, an atmospheric microwave discharge will be created at the end of the center conductor. The mixture in the torch is methane and oxygen. The torch needs a water cooling system due to the heat release of combustion and the thermal effect of the microwave power. It is reported that in this kind of experimental setup, the flame size increases with increased microwave power, especially after 40 *Watts*, which is when the microwave discharge is initiated [59]. With 30 *Watts* microwave power, the flame slightly increases and maintains a premixed combustion flame. When the microwave power exceeds 40 *Watts*, the visual size of the flame and emission intensity both dramatically increase. Also flammability limits of the microwave assisted flame with different microwave power levels were investigated. These are shown in Figure 3.6. The lean flammability limit is achieved under the same total flow condition and decreases the fuel to blow off, which misinterpreted as the lean limit. With the addition of only 10 *Watts* microwave power, the lean flammability limit is extended by 5%–12% in equivalence ratio. With more than 20 *Watts*, the equivalence ratio of lean flammability limit is zero indicating there isn't any need for fuel to sustain the plasma discharge at these plasma levels.

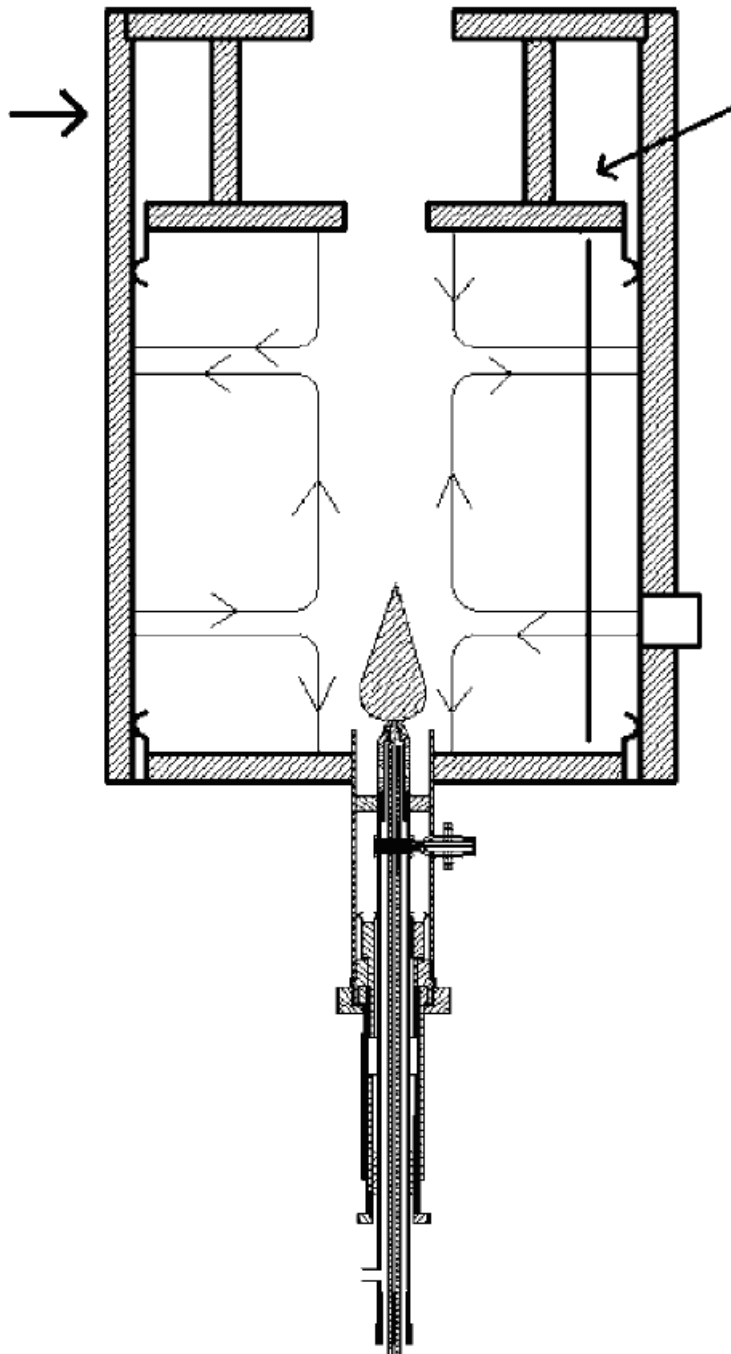


Figure 3.5 Components of microwave cavity plasma assisted flame system with E-field pattern shown [58].

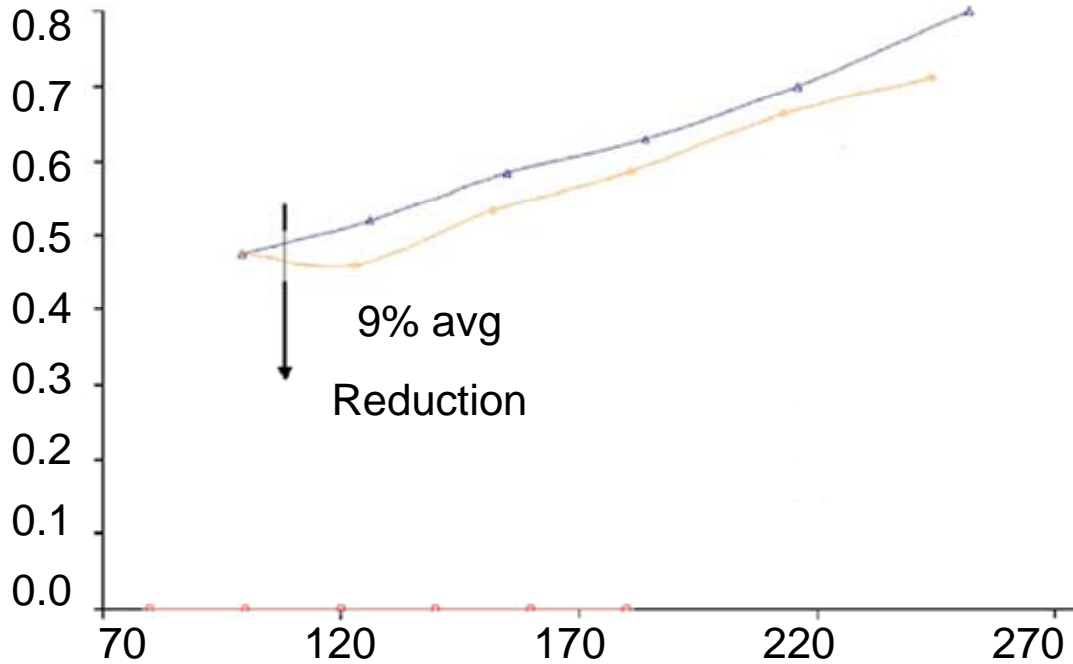


Figure 3.6 Flame extinction limits (lean) with 10 *Watts*, and 20–100 *Watts* microwave power. [58].

## 3.2 Direct Current Plasma System

### 3.2.1 Transient Arc Plasmatron

The transient arc plasmatron used in Chapters 4 and 5 in this research, shown in Figure 3.7, is a transient direct current (*DC*) discharge system that employs the high voltage arc plasmatron [26]. The plasmatron has 5 mm inner and 10 mm outer diameters with an arc chamber distance of about 5 cm. Figure 3.8 shows a schematic of the transient arc plasmatron. The transient arc *DC* system operates on a repetitive glow to spark transition mode, offering the advantages of a thermal plasmatron with low average power output and temperature ( $T_g < 1200\text{ K}$  in an air plasma,  $n_e \sim 10^{14-15}\text{ cm}^{-3}$ ). During glow to

spark transition ( $\sim 100$  ns), a short duration spark or diffused channel arises. The torch works mainly in the glow mode with voltage applied to the cathode (inner electrode) and the surrounding anode. One advantage is that the electrode erosion is less than traditional *DC* torches due to the lower electrode temperature. Therefore, intensive cooling is not required. Classical *DC* arc plasmatrons operate using very high current while this new plasma igniter/plasmatron uses a semi-glow discharge with random completed or noncompleted transitions to spark the mixture, which results in highly efficient ignition and flame control with relatively low current, and thus low average power input. This spark exists for only about 100 nano second, also hence the operation described as being ‘transient’.

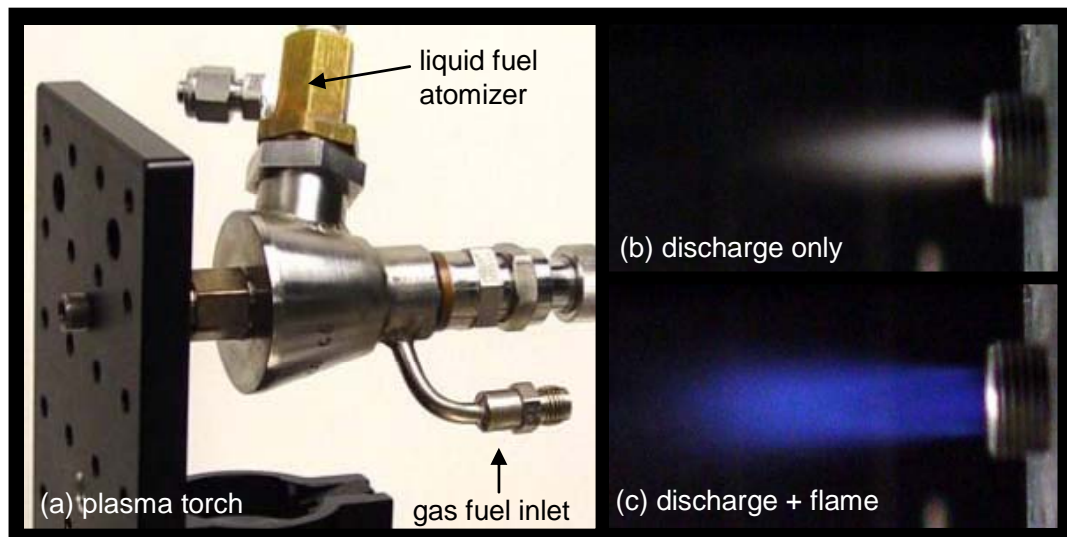


Figure 3.7 Image and schematic of transient arc plasmatron with gas/liquid feeding (a); Air plasma imaging at 20 SCFH and 300 mA (b); Plasma assisted stoichiometric methane/air imaging at 20 SCFH and 300 mA (c).

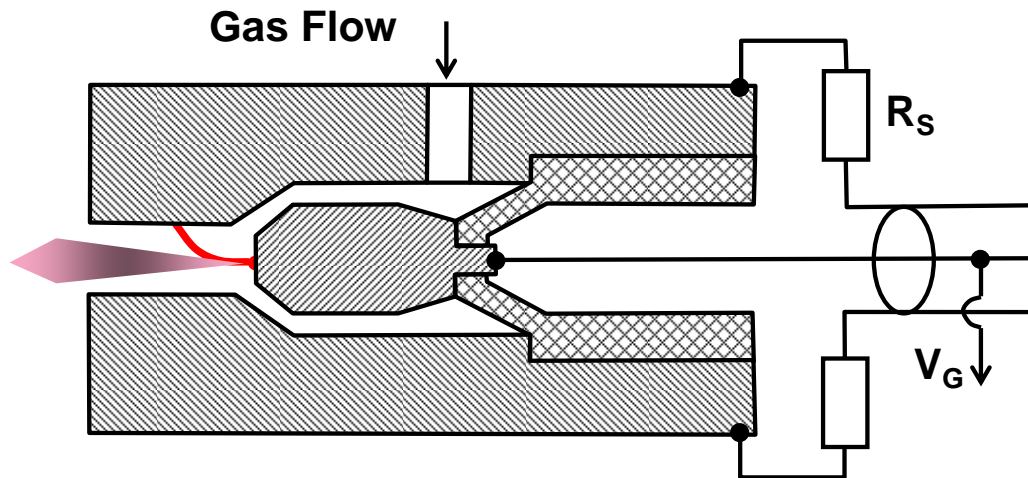


Figure 3.8 Schematic of transient arc plasmatron with gas/liquid feeding.

This plasmatron has been shown to increase the flammability over a wide range of operating conditions. For example, the flame speed with an unburned gas temperature of  $300\text{ K}$  in a traditional premixed methane/air flame is  $S_L=0.40\text{ m/s}$ , which can be increased more than three fold with a current of  $300\text{ mA}$ . A fuel/air mixture can be ignited and combustion stabilized at lean conditions with oxidation occurring with equivalence ratios as low as 0.1, and possibly lower. The ignition mechanism is related to the glow to spark transition mentioned above. At the low current glow mode, dissipated energy is not high enough to initiate the fast oxidation process of the fuel, but it is enough to build a pool of chemically excited species. When glow to spark transition occurs, short duration spark or a diffused channel arises, initiating the ignition process. Even with the small energy released by the transition spark or diffused channel, localized energy deposition coupled with chemically active particles can lead to the rapid initiation of thermal oxidation. Both liquid and gas fuels can be fed directly into the arc chamber, allowing for

high efficiency thermal oxidation without prior hydrocarbon decomposition. In practice, this igniter will be attached to the main combustor to initiate ignition and to sustain combustion.

### 3.2.1 Glow-to-Spark Transition

The uniqueness of this *DC* plasmatron lies in its glow-to-spark transition which was investigated by Matveev et al. [60]. The average discharge current for current *DC* plasmatron has been reduced to 0.1 *A*, much less than typical classical high-current *DC* arc plasmatron. Even though the total power from power supply is low (around 200 *Watts*) and the temperature output from the plasmatron is less than 500 *K*, this plasmatron has proven to be an efficient device for reliable ignition and flame holding in various flow conditions (flow rates, equivalence ratios).

A typical voltage and current plot is shown in Figure 3.9 in this type of plasmatron. The condition for such voltage and current plot is that the discharge gap doesn't recover the dielectric strength completely during the time interval between two high current pulses. From the figure, we can see that the situation in the electric circuit and the discharge gap changes radically. But for this system, the fuel oxidation process is initiated by the high current short time spark shown in Figure 3.9 while the flame cannot be sustained during the pause between the high current pulses.

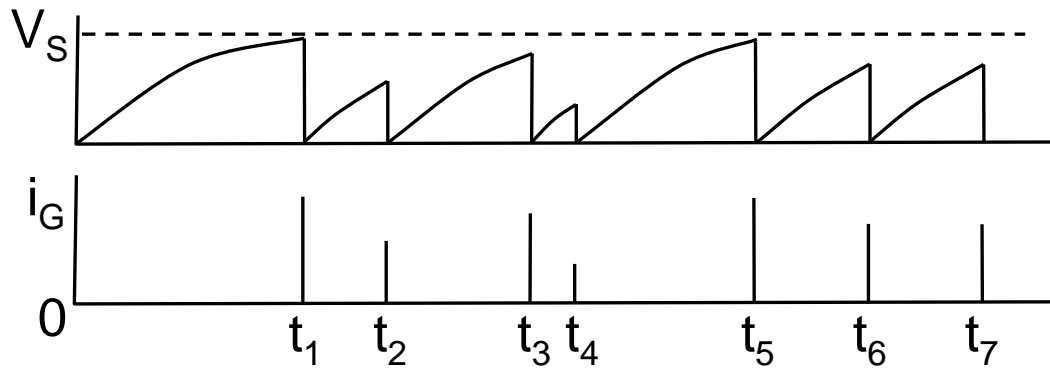


Figure 3.9 Typical DC discharge gap voltage and current passing through the gap [60].

The main idea of glow-to-spark transition is to form a regime where the gap is not fully recovered for its dielectric strength between each high current pulse. The most attractive advantage of such a regime is that the fuel/oxidizer is ignited by the high current spark discharges and is then additionally sustained because of a low-current glow-type discharge. Overall we can call ignition of the discharge “non-steady” since current and voltage fluctuate in this case. The transition of glow to spark can also be divided into completed transition and non-completed transition, as shown in Figure 3.10 by the plot of current and voltage and *CCD* camera photograph of the discharge between  $\Delta t$ . We can clearly see two types of glow-to-spark transition. Also the number of the diffusion channels in the *CCD* images is exactly the same as shown number of glow-to-spark transitions in the current-voltage plots.

To summarize the process of flame ignition in this type of *DC* transient arc plasmatron: most of the time the discharge is a low current glow type with specific power not high enough to ignite the mixture. But with the short duration high current, spark or

diffused channels appear which serve to initiate the ignition process. The initial ignition kernel grows quickly and efficiently into the surrounding medium full of the low density non-equilibrium glow discharge and large number of chemically active particles. In this condition, even very small spark energy is sufficient to sustain combustion process.

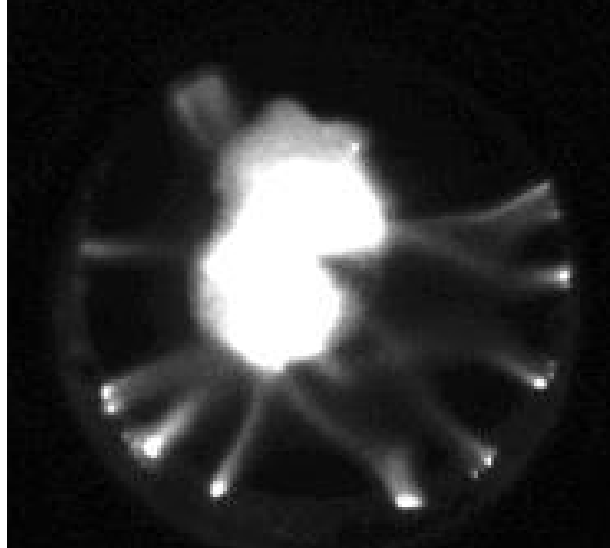


Figure 3.10 Voltage and current plots for discharge in air/propane mixture and *CCD* images of the discharge with exposure time of  $\Delta t$  shown in the voltage-current plot [60].

### 3.3 Laser and Optical Diagnostics Setup

A typical overall *LIF* experimental setup with synchronization of lasers, energy monitor, *ICCD* camera and control system is shown in Figure 3.11. This general setup applies to *LIF* of *OH*, *CO* and *NO*.

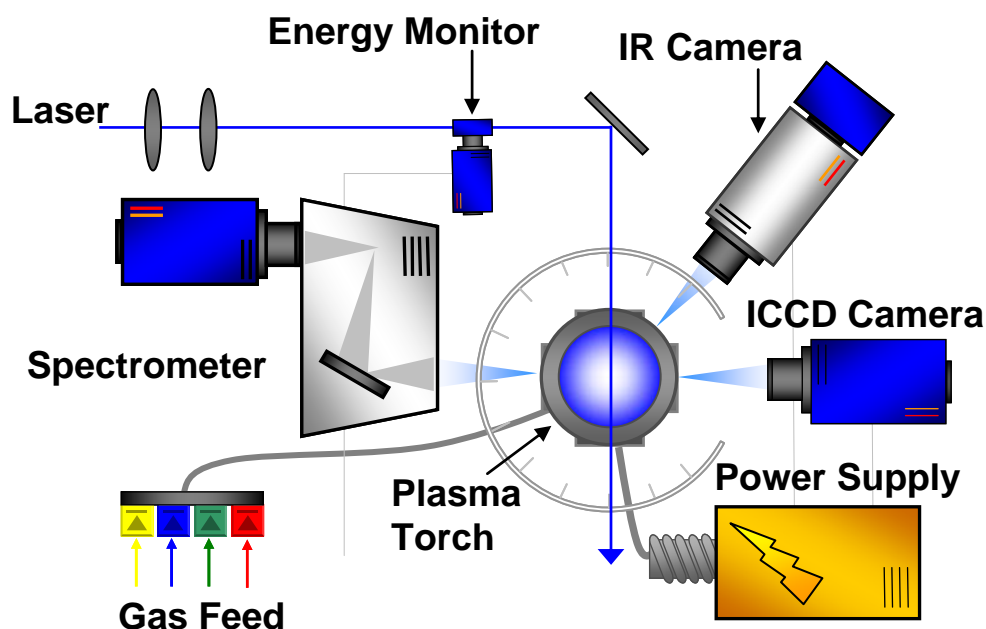


Figure 3.11 Overall experimental setup with synchronization of lasers, energy monitor, *ICCD* camera and control system.

For *OH PLIF*, the *UV* laser near  $283\text{ nm}$  was used for planar laser-induced-fluorescence (*PLIF*) using the  $Q_1(8)$  transition from the  $A^2\Sigma^+ - X^2\Pi(1,0)$  [61]. The emission spectra from experiments are shown in Figure 3.12. The measurements were conducted using a dye laser (Lumonics Hyperdye *HD-300*). *R590* dye from Exciton was used for generating pulses at  $566\text{ nm}$ , which is frequency doubled through an Inrad Autotracker (*ATIII*) to a final output frequency of  $283\text{ nm}$  (linewidth  $\sim 0.1\text{ cm}^{-1}$ ). The  $283\text{-nm}$  beam is isolated from the  $566\text{-nm}$  beam within an Inrad Prism Harmonic Separator (*PHS*). The laser was expanded into a sheet and the fluorescence signal was collected at  $90^\circ$  using an intensified *CCD* camera with a *WG305* filter. The number density was derived by calibrating the signal to that of a Hencken Burner using a methane-air mixture. Here it was assumed that the fluorescence was in the linear regime;

accordingly the  $OH$  number density was further corrected for rate differences for electronic quenching between the methane-oxygen flames and Hencken calibration flame using estimates of quenching rates from the  $OH$   $A-X$  transition [62]. It should be noted that the reported cross sections describe quenching from  $A(v'=0)$ , whereas fluorescence is derived from both the  $A-X$  ( $v'=1, v''=1$ ) and (0,0) bands after excitation to  $A(v'=1)$ .

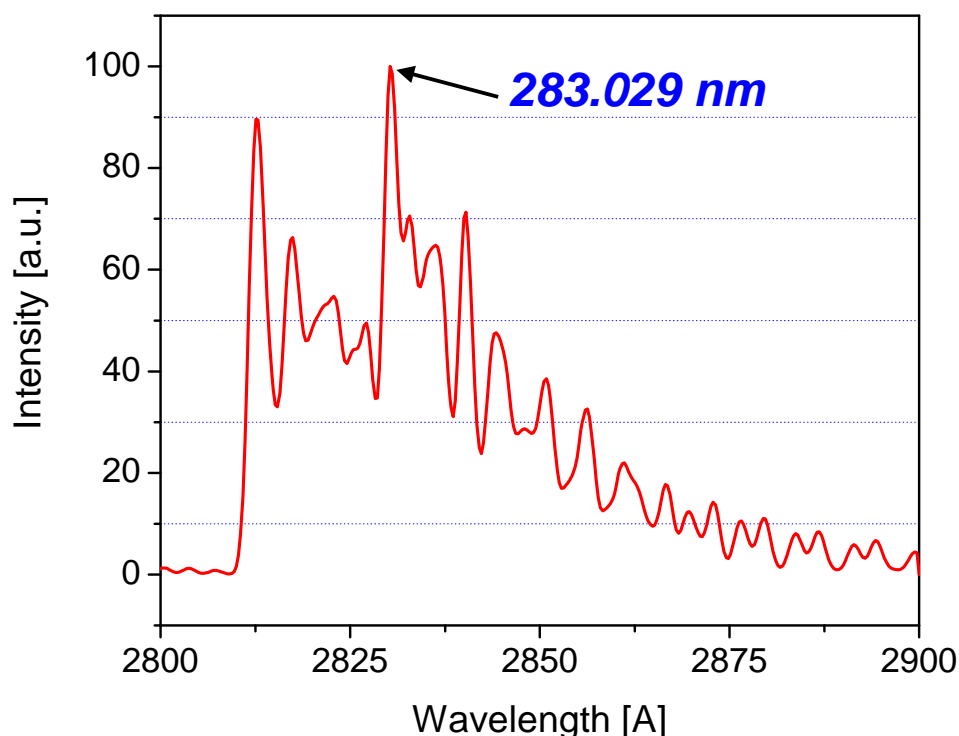


Figure 3.12 Excitation Spectra of  $OH$  ( $A-X$ ) with  $Q_1(8)$  transition shown at 283.029 nm.

$CO$  in the reaction was measured using two-photon  $PLIF$ , pumping the  $B^1\Sigma^+ - X^1\Sigma^+$  (0,0) transition at 230.10 nm [63]. The emission spectrum of  $CO$  with the maximum signal at 230.10 nm is shown in Figure 3.13. The 532 nm beam from a Newport  $Nd:YAG$  was used to pump a Sirah Precisionscan  $LG-2400$  dye laser operating with Exciton  $DCM$  dye. The 653-nm output of dye laser was sum-frequency-mixed with the third harmonic

beam (355 nm) from the injection seeded *Nd:YAG* laser to produce 230 nm radiation (linewidth  $\sim 0.1 \text{ cm}^{-1}$ ) needed for two-photon laser induced fluorescence. The pulse energy is recorded digitally using an energy monitor from LaVision.

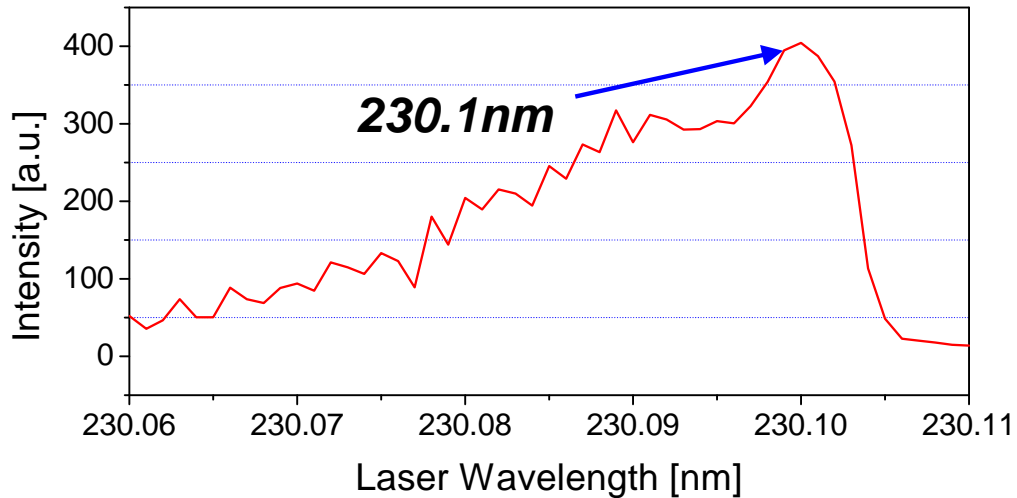


Figure 3.13 Excitation Spectra of *CO* (*B-X*) with highest intensity at 230.109 nm.

The fluorescence signal was imaged with an interference filter centered at 486nm with a bandwidth of 10 nm. The number density is calibrated from a Chemkin simulation (mole fraction for 0 Watt microwave power) using GRI-mech 3.0 [64] with *I-D* flame modeling with methane and oxygen. Equilibrium values past the reaction zone are used as a first order approximation of the Bunsen flame geometry of our flame. Here, it was assumed that the rate for photo-ionization, from a third photon at 230 nm, dominated the rate for electronic quenching and that no quenching correction was needed.

For *NO LIF*, the excitation of *NO* using  $A_2\Sigma^+ - X_2\Pi (0, 0)$  transition requires narrowband UV light near 226 nm. The measurements were conducted using a dye laser

(Sirah Precisionscan-LG-2400) with two stage amplification. Coumarin 450 from Exciton was used for generating pulses at 452 nm, which is frequency doubled through a BBO crystal to a final output frequency of 226.03 nm. Laser pulse energy ranged from 7~10 mJ/pulse with a 7 ns pulse duration. The laser is pulsed at 10 Hz with a final line width of  $0.2 \text{ cm}^{-1}$  at 226.03 nm. For spectrally resolved 1-D imaging of the LIF emission, the beam is weakly focused (diameter  $\sim 1.5 \text{ mm}$ ) along a line 20 mm above the top of the torch. The pulse energy is recorded digitally using a fast photodiode (LaVision).

The fluorescence signals were collected at a right angle to the incident laser beam and focused using a  $f=105 \text{ mm } f/4.5$  achromatic UV-lens (UV Nikorr 105), dispersed spectrally through an imaging spectrometer (Acton SP-2300) and imaged onto an intensified camera system composed of a intensified relay optic (LaVision IRO) and CCD camera (LaVision Imager Intense Pro). The resulting image shows the laser path propagating through the flame on the vertical axis and the spectral resolution on the X axis as shown in Figure 3.14 (upper portion). It should be noted that the emission wavelength region coincides with the emission from the Schumann Runge bands of  $O_2$ . In order to quantify this effect, the emission spectra of NO-LIF in Figure 3.14 have been separated into various components using a nonlinear fitting scheme (using a numerical emission model [53]) and show the potential contribution from  $O_2$ . Therefore, selection of an excitation line with a minimized  $O_2$  contribution should be considered.

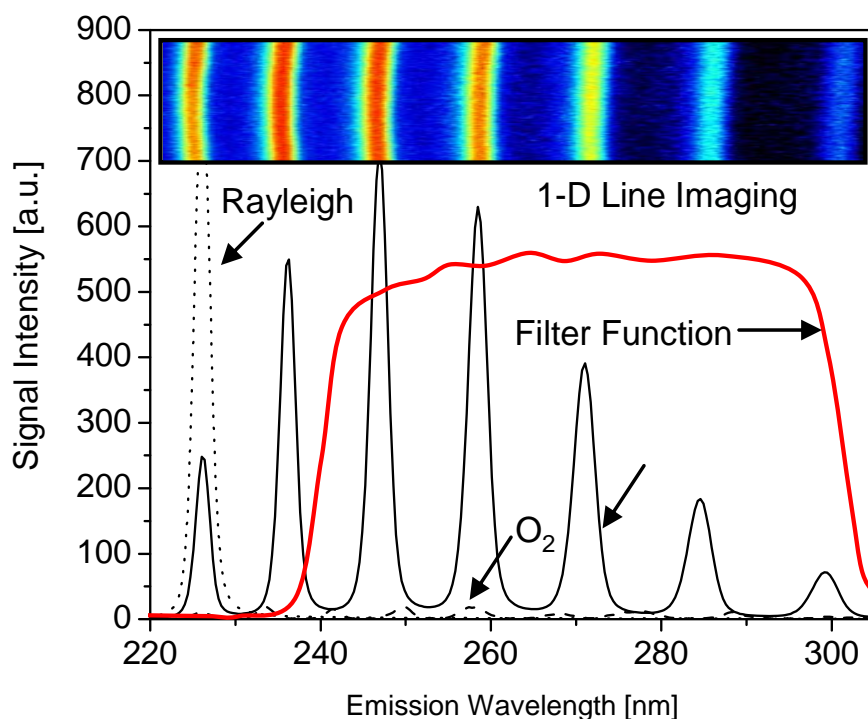


Figure 3.14 . Spectrally resolved *1-D* line imaging (inset) and the emission spectra of *NO-LIF* with 226.03 nm excitation and selected filter function (solid red line). The emission spectra has contributions from *NO*, *O<sub>2</sub>* and Rayleigh scattering.

For planar *LIF* imaging, the laser was optically stretched into a vertical sheet (0.5 X 35 mm) and imaged directed using the intensified camera with a set of filters for suppression of Rayleigh scattering.

A high pass interference filter at 240 nm (Asahi Optics) was used for suppression of the Rayleigh Scattering and a low pass filter at 300 nm (Asahi Optics) was superimposed to cut off any red shift emission past 290 nm as shown in Figure 3.14. It should be noted that the spectral shape of *NO LIF* emission spectra strongly depends on the *NO* rotational state [65], with the upper excited state generally not reaching thermal equilibrium within the fluorescence lifetime. Therefore, to avoid effects of nonequilibrium excited-state

population effects, broadband detection or one or more complete vibrational bands is preferred.

The full resolution of our camera was 1024 X 1376, which was binned 2 X on the vertical axis and 2 X on the horizontal axis to provide a resolution of 64 by 64 micrometers resolution per pixel. All the images were shot with a 50 ns gate to exclude any stray emission and room light. To ensure the spectral accuracy of the laser, scans of neighboring NO lines were conducted before and after each data set and compared to a numerical simulations from *LIFSim* [53]. No perceivable drift of the wavelength was detected. Additionally, an *IR* camera (Flir Phoenix *PTS*) is used for the imaging temperature fields.

For the optical emission measurements, A McPherson 216.5 *l-m* spectrometer (entrance slit of 20  $\mu m$ ) was used for flame emission measurements and rotational *OH* thermometry. The emission was focused using a spherical lens ( $f=50 mm$ ) through a pin-hole filter to isolate the reaction zone. A wide-range scan was conducted over the range 250 to 550 *nm* at an increment of 0.5 *nm* to monitor the qualitative change in the emission of excited state species.

## Chapter 4 Combustion Dynamics with Microwave Discharge

### 4.1 Impact on Flame Structure and Radical Concentration

Photographs, 2-D *OH PLIF* and *CO PLIF* images of the flame are shown in Figure 4.1 as a function of increasing microwave power. At this condition, the fuel combustion power is 22 *Watts* using the lower heating value of methane.

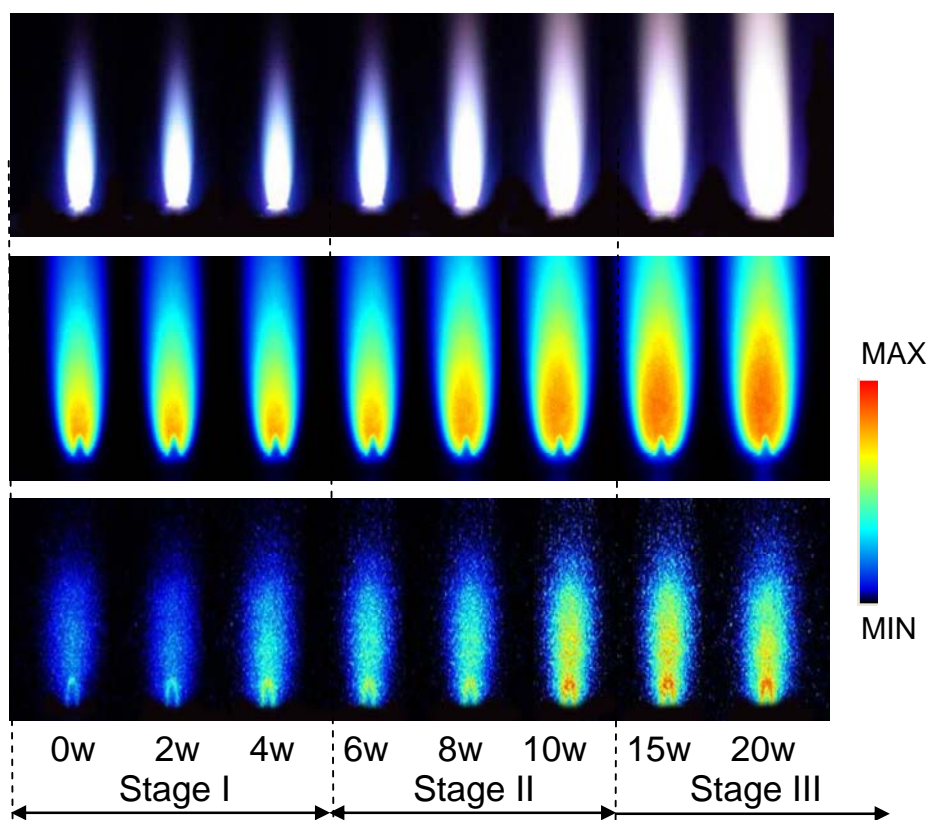


Figure 4.1 Emission (top), *OH PLIF* (middle) and *CO PLIF* (bottom) intensity images of  $CH_4/O_2$  flame vs. microwave power with three stages noted (100 *SCCM* total flowrate at  $\phi=1.1$ ).

The plasma plume is established in a uniform glow mode and micro-arc transition for certain conditions outside our operational conditions. Overall, the flame luminosity and volume are increased as more microwave power is coupled into the flame region. At low powers the flame length is about 2 *mm* and a typical light blue hue is observed from the  $CH^*$  emission. As the power is raised to about 6 *Watts*, the microwave energy generates a distinctly different plasma plume with a purple emission that can be up to 10 *mm* in length (top row in Figure 4.1). From the *OH* images (middle row), it can be seen that the location of the reaction zone does not change dramatically, and only a significant rise of *OH* in the post combustion gas region is evident. It is expected that emission from a dramatic increased ionization and excited state species dominates the normal visible emission spectra at this point. The progression of the plasma discharge as a function of microwave power can be divided into three distinct stages, which we will refer throughout the rest of this dissertation. Note that the microwave power listed here generates a volumetric discharge around the flame. Only a fraction of the energy is actually coupled into the reaction zone.

- **Stage 1:** “Electric Field Enhanced Stage”: The flame is influenced by only a weak electric field. The input microwave power is below 6 *Watts*. No visual change can be seen in either the photographs or the *OH PLIF* images as the power is increased.
- **Stage 2:** “Transition Stage”: Between 6 and 10 *Watts*, the plasma discharge and flame exist at the same time. The discharge volume is dramatically increased. Near the end of this range, the system can sustain a plasma plume even if the combustion gas is

discontinued. The plume can re-ignite a flame if combustible mixtures are reintroduced. The intensity of both  $OH$  and  $CO$  is increased. The reduced electric field concentration is above the critical threshold required for breakdown in the range  $10^{7-8}$   $V/m$ . The distribution of the electric field was shown in Figure 3.4 in the previous Chapter.

- **Stage 3:** “Full Plasma Stage”: If the microwave energy input exceeds 10  $W$ , the system enters a stage where the plasma plume dominates, and the discharge emits a pink hue. As the power is further raised, the volumetric discharge of the plasma is increased and the emission transitions to a pink-purple hue. The discharge has a uniform glow when viewed using an intensified  $CCD$  camera with gate times down to several nanoseconds.

Without a flame present, the microwave energy cannot couple itself into the air and generate a plasma plume in the power ranges discussed here. An interesting phenomenon was observed that air discharge can be sustained at microwave power higher than 10 Watts after oxygen/fuel line was shut off.

In all three stages microwave energy is coupled into the flame via energy transfer from the input microwave energy source into the electron gas. This energy transfer then raises the electron gas temperature, thereby creating a non-equilibrium chemistry condition in all three stages. The electron gas transfers its energy via electron - heavy molecule elastic and inelastic collisions processes into the heavier molecular gases. The main differences for these three stages are that electrons in Stage 1 mostly come from

flame only whereas in Stages 2 & 3, the electrons are believed to increase by 1 to 2 orders of magnitude (from  $\sim 10^{10} \text{ cm}^{-3}$  to  $\sim 10^{11-12} \text{ cm}^{-3}$ ).

To quantify the change in the OH radical over the entire range of microwave powers in more detail, the number density of OH in the reaction zone of the flame is shown in Figure 4.2.

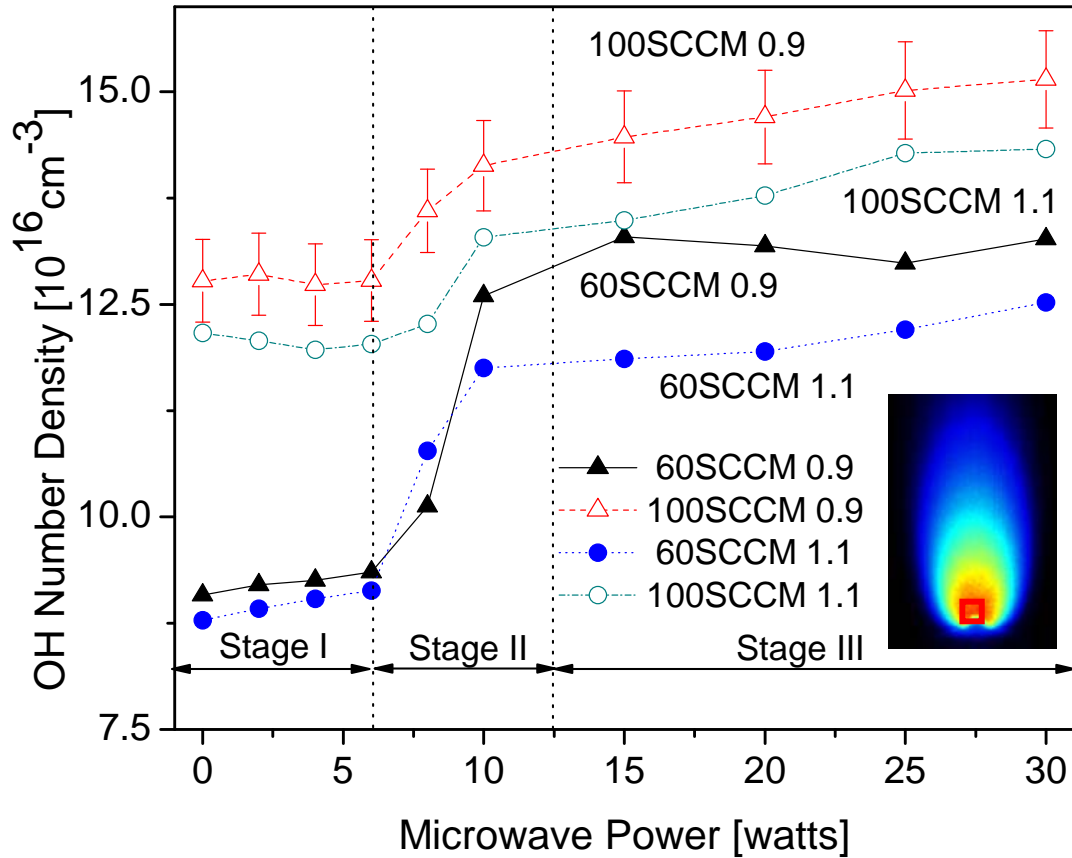


Figure 4.2 *OH* number density in burnt gas of  $\text{CH}_4/\text{O}_2$  flame vs. microwave powers from averaged *PLIF* images.

The region of data extraction in the *PLIF* image is shown in the inset and is mainly from the reaction zone of the flame. The *OH* number density is plotted as a function of microwave power (0 to 30 *W*) for different total flow rates and equivalence ratios. The

data is extracted from *OH 2-D PLIF* images which have been averaged over 200 single shots and calibrated for variations in laser energy. For each data set (0 to 30 *W* at the same total flow rate and equivalence ratio), the same general trend over the three stages can be observed. At the same equivalence ratio ( $\phi=0.9$  or 1.1), the *OH* number density increases with total flow rate. Also at the same total flow rate (60 or 100 *SCCM*), the *OH* number density for  $\phi=0.9$  is higher than that for  $\phi=1.1$ .

- **Stage 1:** “Electric Field Enhanced Stage”: In the first stage (0 to 6 *W*), the *OH* does not show a noticeable increase when the measurement uncertainty is considered ( $\sim 8\%$ ). There is insufficient microwave energy to generate a cascade of ionization leading to a plasma discharge. Nonetheless, both flame speed and stability is enhanced mainly through temperature rise from elastic collisions and in-situ reforming.
- **Stage 2:** “Transition Stage”: In this stage (6 to 10 *W*), as the microwave field intensity increases,  $T_e$  (electron temperature) exceeds  $T_g$  (gas temperature). High  $T_e$  and high reactivity lead to inelastic collisions for excitation, dissociation and ionization to generate new species and eventually break down to generate a plasma discharge.
- **Stage 3:** “Full Plasma Stage”: In the third stage (more than 10 *W*), the plasma volume grows larger and *OH* production remains relatively constant even though microwave power is raised.

It can be seen by quantifying the slope of *OH* increase with respect to power input, for 60 *SCCM* total flow rate, the slope for Stage 2 is 4 times bigger than that in Stage 1

and 20 times bigger than that in Stage 3. For the 100 *SCCM* case, the change in slope is not as dramatic although Stage 2 is still the region of maximum change rate.

It is believed that in plasma enhanced flames, free electrons are generated in the flamefront through the reaction  $CH+O \rightarrow HCO^+ + e^-$  [66, 67]. At higher total flow rates, more heat release from combustion with relatively less heat loss to the burner leads to higher temperatures, which results in more CH and subsequently more electrons. This results in more OH production for higher flowrates in Stage 2 of Figure 4.2. In Stage 1, the microwave power is not high enough to generate more atomic oxygen.

The other important pathways for OH production in Stage 2 are  $H_2O + e^- \rightarrow e^- + H + OH$ ,  $H_2O + O \rightarrow OH + OH$ , and  $H + O_2 \rightarrow OH + O$  [68]. Atomic oxygen is believed to increase in a plasma coupled combustions more than in combustion only cases [11] (increased from the order of  $10^{-5}$  in mole fraction without plasma discharge to  $10^{-4}$  with pulsed plasma). A Chemkin simulation using GRI-mech 3.0 [64] with a premixed burner model of a flame with methane and oxygen show that, with the addition of  $10^{-4}$  mole fraction of atomic oxygen, the OH number density increases by 40%. A similar increase was observed in our experiments for both  $\phi = 0.9$  and 1.1 conditions at a total flow rate of 60 *SCCM*.

There are three reasons for relatively stable OH number densities in Stage 3. First, even though higher microwave power creates more electrons, the increased OH by the electron impact reactions is cancelled by more space recombination as additional active species are increased. Second, the microwave coupling efficiency is lower for higher

microwave powers, due to more recombination reactions. Third, even though the power is increased, the plasma volume is also increased and the power/volume ratio remains relatively constant. From a practical perspective, this would be the stage that can be utilized for both flame stability enhancement and re-ignition.

The relative uncertainty associated with the beam energy fluctuation corrections and wavelength shift of the laser are expected to be less than  $\pm 4\%$ . The camera readout error was suppressed by subtracting a background image taken without the laser pulse and can be neglected. Combined with the errors from the flowmeters and shot noise, the overall relative uncertainty is expected to be less than 8%. The error in the absolute accuracy is expected to be higher (10–20% range).

Figure 4.3 shows the OH number density versus equivalence ratio (0.8 to 1.2) for various microwave powers (0 to 30 W). For the same equivalence ratio, the trend in the OH number density is generally the same in the three stages with the highest number density being exhibited around  $\phi=0.9$  and 1.0. For each of the lines in Figure 4.3, the OH profile change as a function of the equivalence ratio is similar to that typically found in regular premixed flames [69]. This profile will be influenced by the electron number distribution as microwave energy is coupled into the flamefront. Coincidentally, the simulations of a microwave plasma enhanced combustion of methane and air [67] show that the electron number density reaches a peak when the equivalence ratio is close to stoichiometric and decreases towards both lean and rich conditions, and therefore, the overall trend of the OH peaking near  $\phi=1$  is maintained. The results show that the OH

number density for powers above the break-down threshold (above stage 1:  $\sim 6\text{ W}$ ) is much higher than the two lines in stage 1 (0 and 5  $\text{W}$ ) where only the influence of the electric field was altered due to the increase in electron-impact reactions.

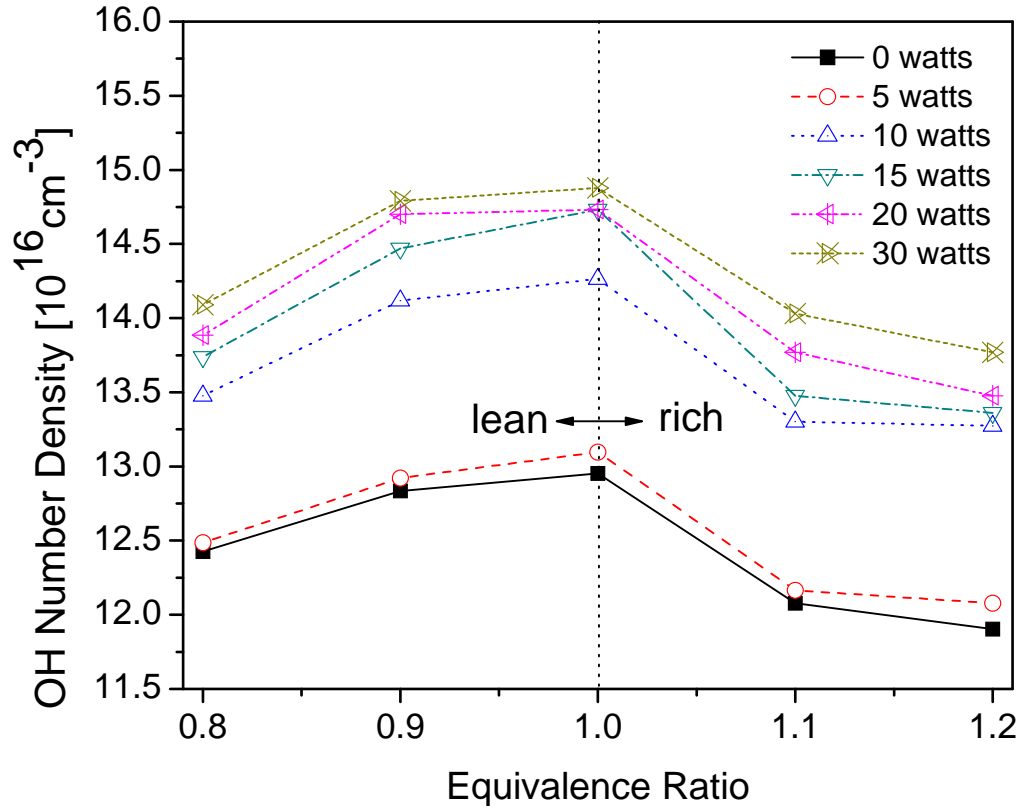


Figure 4.3 *OH* number density vs. equivalence ratios ( $\phi=0.8$  to 1.2) with different microwave powers (0 to 30 *Watts*). Total flow rate is 100 *SCCM*.

## 4.2 Flammability Limits and Flame Speed

The addition of plasma has been shown to increase the flammability limits [29, 30]. Flammability limits (both lean and rich) for this plasma discharge system with and without microwave enhancement are shown in Figure. 4.4.

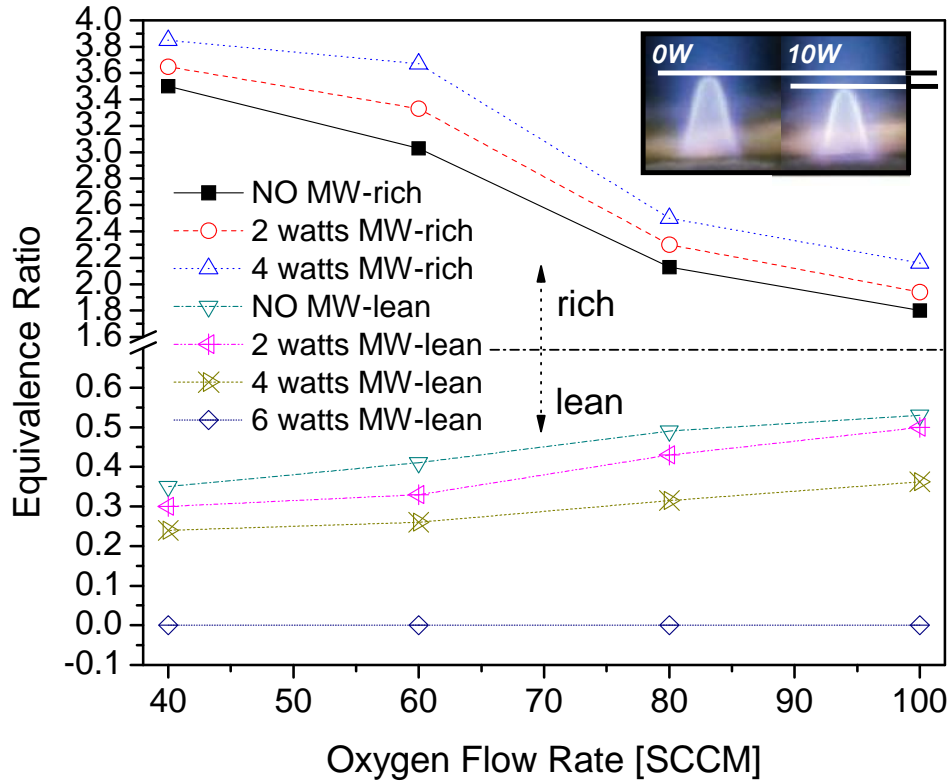


Figure 4.4 Flammability limits for methane/oxygen flame (lean and rich) with flamespeed increase demonstrated by flame photographs with no microwave radiation and 10 *Watts* microwave radiation (right top).

In these measurements, the total flowrate is not held constant in determining the extended oxidation limits. In the upper portion of the figure, the oxygen flow rate is fixed and methane is increased to achieve the rich flammability limit. Our goal in this section is to show how much fuel can be put into and combusted with constant oxygen flow input.

In the bottom portion of the figure, the oxygen flow rate is fixed and methane is reduced to obtain the lean flammability limits. All the data presented in Figure 4.4 are in the low-power range (0 to 4 *W*), with a flowrate spanning from 50 to 250 *SCCM*. Clearly we can see improvements in the flammability in this range, although the flame enhancement is only through a weak electric field. At power levels of more than 6 *W*, the

discharge could be sustained with only oxygen or methane and without combustion. As the ground state  $OH$  number density was not shown to increase in this stage, the improvement in the flammability limit is mainly assumed to be from temperature increase. This will be discussed further next.

Flamespeed enhancement was also shown in this region by observing the change in the reaction zone contour as the flame velocity was changed. An example of this is shown in the upper right inset of Figure 4.4, where a photograph of the flame is shown without microwave input and with 10  $W$  of microwave power. Here, the flamespeed increase is demonstrated by a decrease in the Bunsen flame “cone” angle; this is observed in all three stages of the microwave coupling. Flamespeed enhancement using microwave fields has been observed previously in tunable microwave cavities, using free floating laminar premixed flames [28, 70]. Note that in Figure 4.4 the flame images look different from those in Figure 4.1 due to different exposure times. In Figure 4.1, a longer exposure time (1/10 second) is used to integrate the emission from all the chemical species. In Figure 4.4, a significantly shorter exposure time (1/30 second) was used for high contrast of the flame front.

### **4.3 Emission Measurements and Temperature**

In order to probe the changes in excited state species and temperature, spectrally resolved emission of the reaction zone was obtained. Figure 4.5 shows the emission spectra for the methane-oxygen flame with no microwave input and 10  $W$  microwave

input (top) and *OH* rotational temperature for different total flow rates and equivalence ratios (bottom) with the top portion of Figure 4.5 demonstrating a fast scan over the entire spectral range.

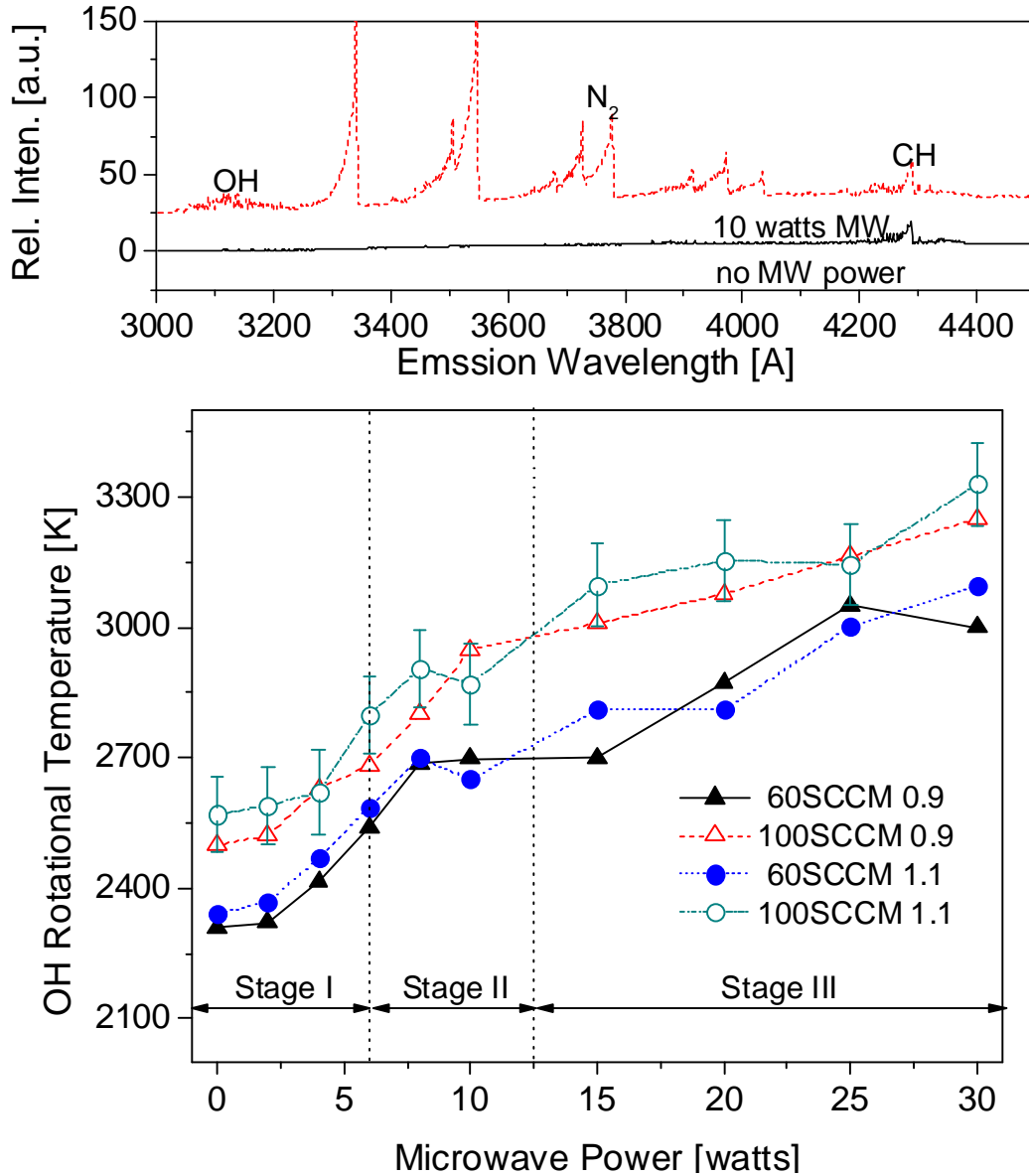


Figure 4.5 Emission spectra from  $CH_4/O_2$  flame with no microwave radiation and 10 W microwave radiation (top) and *OH* rotational temperature at the same conditions as in Figure 4.2 (bottom).

The OH rotational temperature is calculated using a more detailed scan over the *OH* with a resolution of 1/30 nm and higher gain (not shown here). The general range and trend of the temperatures reported here agree fairly well with a previous measurement using *CH* emission in a similar torch configuration [71]. As the signal is from chemically excited species, the emission intensity is a relative measure of concentration. Although, temperature corrected concentrations of excited-state species are not reported here, it is clear from Figure 4.5 that even without relevant temperature corrections, for 10 *W* of microwave power, the emission is generally higher and excited state species, such as *OH* and *CH*, have been shown previously to play an important role in the flame chemistry [29, 72]. Temperature measurements using *CH* emissions were also measured for comparison and were shown to generally agree with the *OH* rotational temperatures (described below) and in the same range. The main choice for using *OH* is due to the fact that distortion from self absorption is lower (smaller cross-section), and more importantly, because OH is more pervasively present past the reaction zone than *CH* which occupies a small portion of the flame front (note that the flame is very small).

For the reported temperatures, the *OH* population density is determined under the assumption of Boltzmann distributions. The emission intensity *I* can be expressed according to the following equation [73]:

$$\ln\left(\frac{I}{\lambda^4 S}\right) = -\frac{E_j}{kT} + \ln C, \quad (4.1)$$

where  $\lambda$  is the emission wavelength (nm),  $S$  is oscillator strength (Honl-London factor) (a.u.),  $E_i$  is the rotational energy of the initial level of the line ( $\text{cm}^{-1}$  or eV),  $k$  is the Boltzmann constant,  $C$  is the proportionality constant, and  $T$  is the rotational temperature. Four transitions ( $R_2(14)$  (307.1145 nm),  $R_2(15)$  (307.3028 nm),  $R_2(4)$  (307.4369 nm), and  $R_2(3)$  (307.7028 nm)) and associated constants ( $\lambda, S, E_J$ ) are taken from [74, 75] for the rotational thermometry.

Table 4.1 Transitions for OH rotational Temperature Method

	$\lambda$ (nm)	$S$ (a.u.)	$E_J$ ( $\text{CM}^{-1}$ )
$R_2(3)$	307.7028	9.1	32643.83
$R_2(4)$	307.4369	12.8	32778.99
$R_2(14)$	307.1145	63.2	35913.21
$R_2(15)$	307.3028	57.2	36394.95

The overall error is expected to be about  $\pm 100$  K [74], including the fitting error. The  $OH^*$  temperatures reported here are meant to provide understanding of the change in temperature through the various stages of plasma coupling, and we acknowledge that the rotational temperatures reported here may vary from the actual translational temperature due to effects such as self absorption [76] and chemical pumping mechanisms [77] which may preferentially populate high lying rotational states in the electronically excited  $OH$ .

For microwave field enhanced combustion (Stage 1), there are different reports in the literature about the temperature change: In some cases about  $\sim 100$  K temperature

variations were observed [78] whereas in other cases measurements showed no increase in rotational temperature [70]. We observed an *OH* rotational temperature increase of around 100 to 150 K, which we believe is directly responsible for the observed increase of both flame speed and flammability. Overall, the *OH* rotational temperature increases with microwave power input, which confirms the results from a previous study using *CH\** [71].

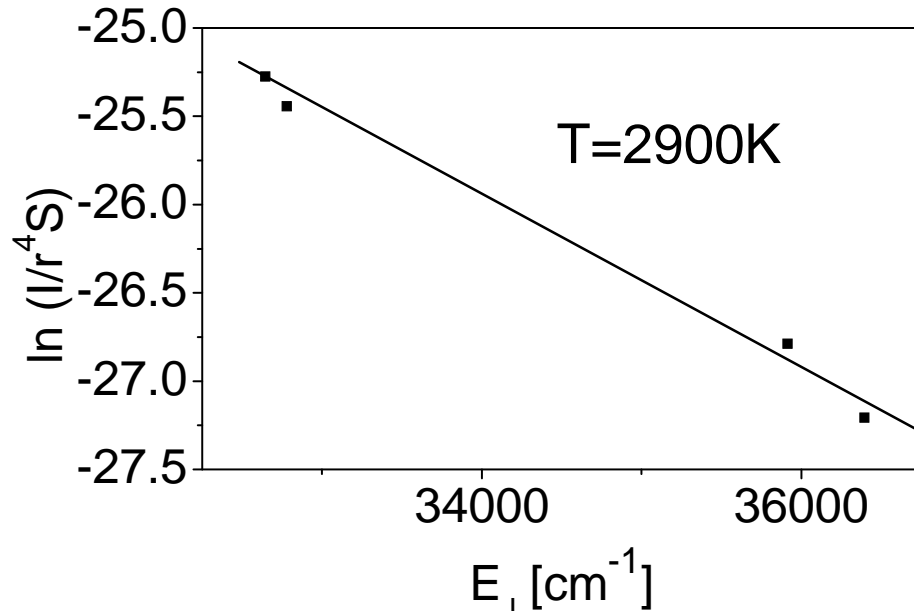


Figure 4.6 Sample Image to show how to obtain *OH* rotational temperature at condition of 100 *SCCM* total flow rate and equivalence ratio of 1.1. The *OH* rotational temperature using this method is 2,900 K.

The discharge power noted here is not the exact power coupled into the flame. Much of it is lost along the transmission lines and volumetric spatial microwave field distribution full of the whole cavity which is larger than the flame. We estimate that about 40% of the power is coupled into the flame considering the electrical components of the circuit and mode of microwave propagation. Assuming constant gas composition,

specific heats (products), and using rotational temperature as the overall global temperature, about half of the coupled energy is going into the temperature increase, and therefore a significant portion is coupled into the chemical energy conversion via kinetics effects. The plasma energy is calculated as a fraction of the total combustion power (5% to 10%). This fraction decreases with increasing power.

We acknowledge that the use of rotational temperatures over a wide range of plasma powers is subject to error and unintended influence from non-equilibrium effects. Other optical measurements such as Rayleigh scattering can be considered in the future to corroborate these findings.

#### **4.4 In-Situ Fuel Reforming**

One mechanism to explain the enhancement by the plasma discharge is fuel reforming. Fuel reforming, or fuel break up or fuel fragmenting is a process where hydrocarbon molecules are broken into syn-gas (hydrogen and carbon monoxide). Fuel reforming in *PAC* area was mostly conducted by Kim and et al at Stanford University. They used a USRD discharge, finding that flame stability is most and only sensitive to the concentration of *CO* and *H<sub>2</sub>* in the system [9]. In another study, it is reported that the depletion of *H<sub>2</sub>* and *CO* leads to flame instability. Flame enhancement for the *H<sub>2</sub>* flame is not observed for the same conditions under which the hydrocarbon flame is enhanced [79].

Figure 4.6 shows  $CO$  number density in the reaction zone of the  $CH_4/O_2$  flame vs. microwave powers for total flow rates of 60 and 100  $SCCM$  and for  $\phi=0.9$  and 1.1 from the two-photon absorption  $LIF$  ( $TALIF$ ) images. The region of interest (displayed in Figure 4.6) is in and around the reaction zone of the tip of the flame where the  $CO$  concentration is highest.

Overall  $CO$  number density increases with microwave power for all conditions. In Stage 1, the in-situ fuel reforming (to hydrogen and carbon monoxide) as well as the temperature increase is expected to contribute to the enhancement in flammability limits and flame speed. It appears from Figure 4.7 that the increase in  $CO$  is most dramatic near the intersection of stages 1 and 2, and tends to be linear towards the end of stage 2 and into stage 3. This is because the fraction of microwave power that goes into fuel reforming is larger near stages 1 and 2, whereas more power is directed towards ionization of gases in stages 2 and 3.

$CO$  production in rich flames is generally higher than in lean flames. This is confirmed in the first data point (0  $W$  microwave power) of all four series. But in Stages 2 and 3 when microwave power is higher,  $CO$  number density at 100  $SCCM$  with  $\phi=0.9$  is higher than that at 60  $SCCM$  with  $\phi=1.1$ . This is because in the higher microwave power range, the effects of fuel breakdown from the plasma discharge surpass the thermal  $CO$  production in the flame. With lower flow rates, the microwave energy distribution per particle will be larger. Therefore, at lower microwave powers (Stage 1),  $CO$  production is higher for rich conditions while at higher microwave powers (Stages 2 and 3),  $CO$

production for lower total flow rate is higher than that at the higher flow rate. Also at higher flow rate, the residence time (during which the mixture gas reacts with the discharge) is shorter than that at a lower flow rate.

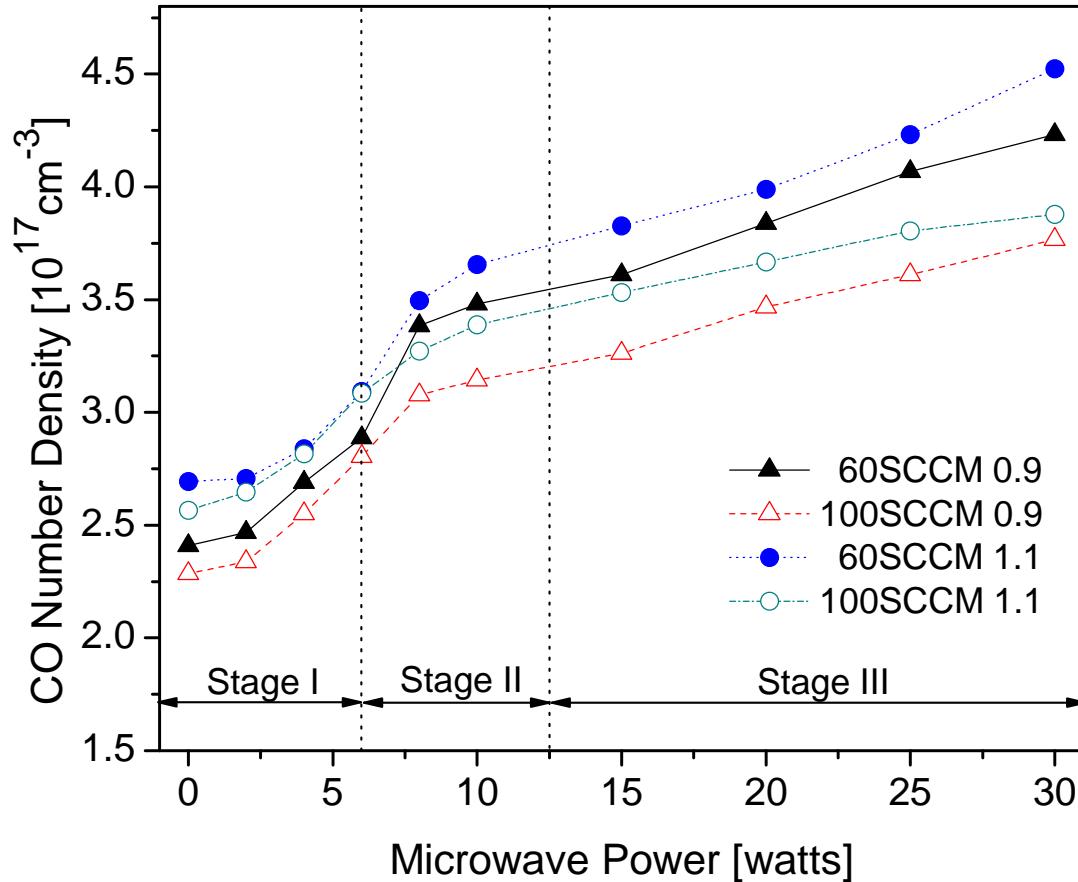


Figure 4.7 *CO* number density in burnt gas of  $CH_4/O_2$  flame vs. microwave powers at the same conditions as in Figure 4.2 using *CO* Two-Photon Laser Induced Fluorescence.

It is of great interest to quantify of the degree of fuel reforming assisted by the plasma. Syn-gas generation has other practical implications in terms of hydrogen generation [80, 81]. The *CO* number density increases to  $3.88 \times 10^{17} \text{ cm}^{-3}$  at the highest microwave power of 30 *W*, from  $2.57 \times 10^{17} \text{ cm}^{-3}$  without microwave at the same flow

condition (100 *SCCM* and  $\phi=1.1$ ). Mole fraction was calculated using the rotational temperature in the previous section. *CO* mole fraction increases approximately to 15% from 9% without microwave in the same condition. Assuming that the water is in vapor state, in our configuration, 18% of the total methane undergoes reforming to syn-gas at 30 *W* of microwave power. This is significant considering the competing oxidation reactions which subsequently lead to *CO*<sub>2</sub>.

## Chapter 5 Combustion Dynamics in a DC Plasmatron

### 5.1 Premixed and Non-Premixed Modes

The discharge system used in this chapter is a transient arc direct current (*DC*) plasmatron [26, 60, 82, 83] from ‘Applied Plasma Technologies’ and is shown in Figure 5.1.

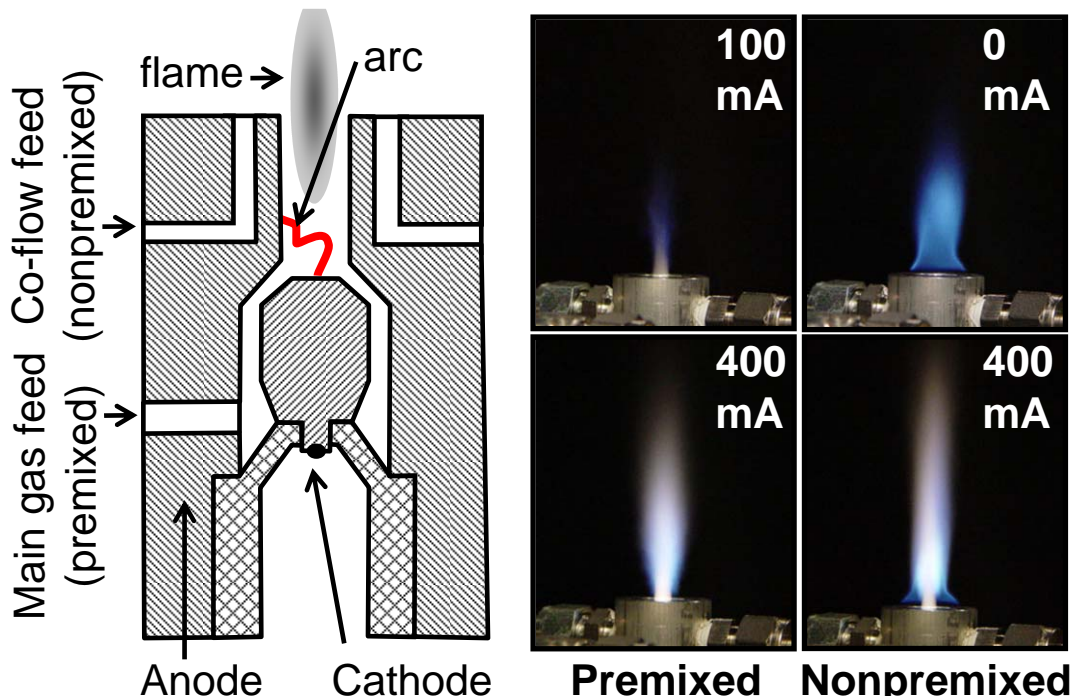


Figure 5.1: Schematic of transient arc plasmatron with cathode in the center and two different inlets are used to get two different experimental setup(left); Images for premixed (100 *mA* and 400 *mA* *DC* current) and nonpremixed (0 and 400 *mA* *DC* current) flames of methane/air with equivalence ratio of 0.9.

The plasmatron exit has dimensions of 5 *mm* for the inner diameter, and the arc chamber is approximately 50 *mm* in length. This discharge system operates on a

repetitive glow-to-spark transition mode, offering the advantages of a thermal plasmatron with low average power output, low average temperatures (600–1300 K), and high electron density. The torch operates primarily in the glow mode where high voltage ( $\sim 10$  kV) is applied between the cathode (inner electrode) and the surrounding anode. During the glow-to-spark transition, a short duration spark ( $\sim 100$  ns) [60] or diffuse channel arises and propagates towards the torch tip. Since the overall temperature is low, however, electrode erosion is significantly lower than with traditional DC torches, and the torch can withstand prolonged operation without internal cooling.

There are two gas inlets in this discharge system: a lower one is connected directly to the arc chamber, and a top inlet provides co-flow around the main exit of the torch, as shown in Figure 5.1. In the *premixed* mode, a mixture of fuel and air flows through the lower inlet, while a nitrogen co-flow is sent through the top inlet to further stabilize the flame and cut off entrainment of atmospheric oxygen. In the *nonpremixed* mode, air flows through the lower inlet (to generate the discharge) and methane through the top inlet. As this is an igniter for a combustor, it is designed for high flow with plasma stabilization. Therefore, most of the flowrates used in this study are conditions that are too high for unassisted stabilization; however, a few low power nonpremixed mode settings where natural stabilization can be achieved are also employed, as shown in Figure 5.1 (far right for the nonpremixed flames). Here, images for premixed (100 mA and 400 mA DC current) and nonpremixed (0 and 400 mA DC current) flames of

$CH_4$ -air are shown. It can be seen that in both modes, the height of the illuminated region is increased with higher  $DC$  current due to the presence of a plasma plume. For premixed flames, the reaction mainly occurs inside the chamber at low  $DC$  currents, while at higher currents the discharge plume is observed outside the torch as the plasma is not fully quenched inside the cavity. For nonpremixed flames, the combustion occurs entirely outside the chamber (since there is no fuel in the plasma chamber), and the center region shows a bright white hue as the plasma plume interacts with the flame. The anchor of the nonpremixed flame can be seen at the base of the plasma plume. Both the size and luminosity of the plume increase as a function of the input power.

## **5.2 Impact on Flame Structure**

Single and ensemble averaged  $OH$  Planar Laser-Induced Fluorescence (*PLIF*) images are shown in Figure 5.2 as a function of increasing microwave power for both premixed (top) and nonpremixed flames (bottom). Average images were based on acquisition of 200 instantaneous images.

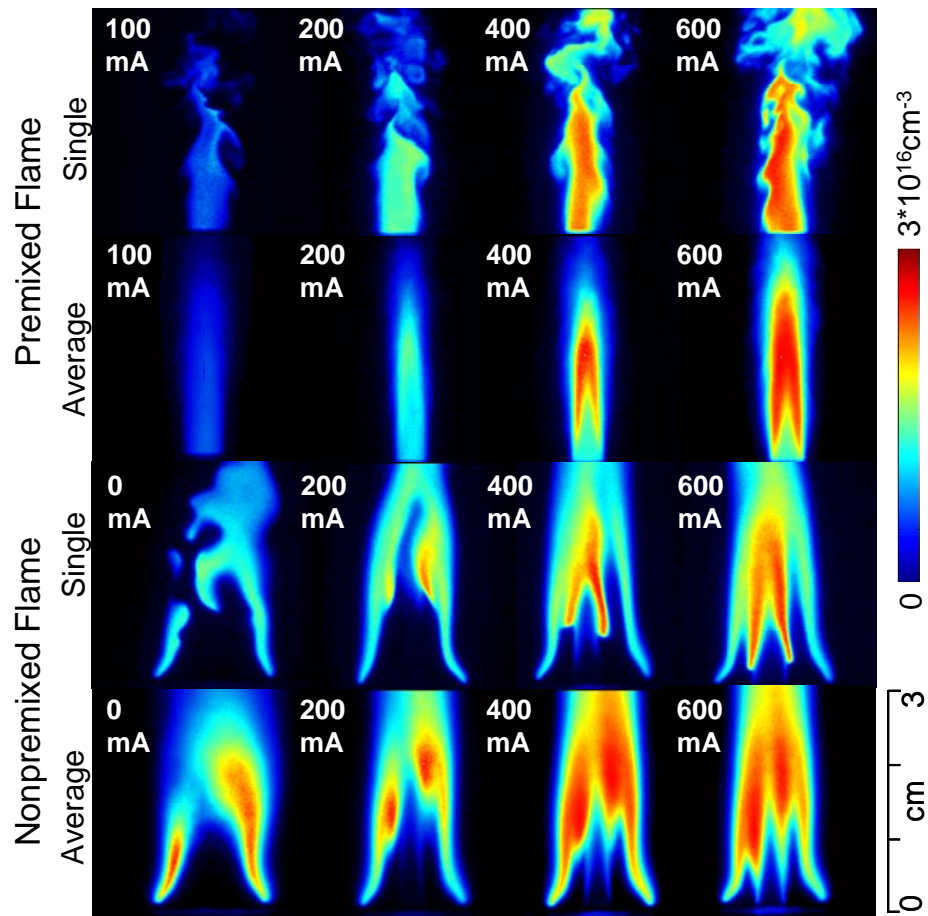


Figure 5.2: Single and averaged 2-D *OH* Planar Laser-Induced Fluorescence (*PLIF*) images as a function of increasing microwave power for both premixed flames (top) and nonpremixed flames (bottom).

Here, the total flow rate for the reactants is 9 standard liters-per-minute (*LPM*, referenced to *STP* conditions), and the equivalence ratio is  $\phi=0.95$ . The equivalence ratio in the nonpremixed case is defined here as the ratio between the fuel and oxygen in the inner nozzle. At these conditions, combustion power from the oxidation of the fuel is about 500 *Ws* using the lower heating value of methane. For 1<sup>st</sup> order comparisons, measurements using a thermocouple show that temperatures for premixed flames are

about 100 to 200  $K$  higher than in nonpremixed flames for the same fuel flowrates. For premixed flames, the visible flame luminosity and plasma volume increase with increased current/power. The range of current is between 100 and 900  $mA$  in our research, resulting in a discharge power of 150 to 750  $W$ . At low powers ( $\sim 100$   $mA$ ), the  $OH$  signal is lower than that in a typical premixed flame, presumably because a significant portion of the oxidation reactions occur inside the arc chamber, where the mixture initially comes in to contact with the discharge. When the  $DC$  current is higher, the reaction rates are expected to increase, resulting in a more compact flame structure especially as a larger portion of the fuel is oxidized inside the chamber. However, the introduction of added species and charged particles with higher momentum (and new reaction chemistry involving ions and electrons) provides new chemical pathways. This ultimately results in a higher concentration of  $OH$  radicals, via reactions such as  $O(^3P)+H_2O \rightarrow OH+ OH$ ,  $O(^1D)+H_2O \rightarrow OH+ OH$  [68].

There are many kinds of thermocouple, each made from a unique metal or alloy to achieve its temperature measurements range and application. Also there are different diameters for the bead: on the one hand a bigger bead can last longer, on the other hand a bigger bead leads to higher error and interference with the measured volume. Also, different types of thermocouples have dramatically different measurements ranges, for example the  $B$  type can measure a reading range of 300  $K$  - 2000  $K$  whereas it is 0  $K$  - 1500  $K$  for a  $K$  type thermocouple. What is needed in this research is one that can measure high temperature, with a medium size of bead diameter and a longer lifetime

for the thermocouple. For the readings of thermocouple measurements, calibration should account for systematic errors from emission to the wall. Calibration for different types with different bead diameters is shown in Table 5.1. In our experiments, the *B* type thermocouple with a 0.02 inch diameter was used for its relatively long life and moderate size bead.

As can be seen in Figure 5.2, nonpremixed flames show a unique two-cone flame structure: within the inner cone the main oxidation of the fuel with the air from the plasma discharge takes place; within the outer cone combustion with the ambient air occurs. Overall, the height of the flame is greater for the nonpremixed mode than that for the premixed case while the flow appears to be more turbulent in the premixed flames due to the shorter main reaction zone. The outer cone flame in the nonpremixed mode can be sustained without any *DC* plasma power input for some of the lower flow rates used. In the nonpremixed flame, the reaction zone for the outer cone remains relatively constant as power is increased. However, the inner cone is dramatically increased as highly reactive air interacts with the fuel. At powers exceeding 400 *mA*, the *OH LIF* intensity for the inner flame front is much higher than the outer one. Flame stability is dominated by the plasma discharge.

Table 5.1 Thermocouple Measurements and Calibrations

$T_{\text{Measured}}$	<i>B</i> 0.020''	<i>B</i> 0.032''	<i>J</i> 0.032''	<i>K</i> 0.032''
100 <i>K</i>	<i>N/A</i>	<i>N/A</i>	<i>N/A</i>	99.95 <i>K</i>
200 <i>K</i>	<i>N/A</i>	<i>N/A</i>	<i>N/A</i>	199.95 <i>K</i>
300 <i>K</i>	300 <i>K</i>	300 <i>K</i>	300 <i>K</i>	300 <i>K</i>
400 <i>K</i>	400.12 <i>K</i>	400.15 <i>K</i>	400.15 <i>K</i>	400.15 <i>K</i>
500 <i>K</i>	500.41 <i>K</i>	500.53 <i>K</i>	500.53 <i>K</i>	500.53 <i>K</i>
600 <i>K</i>	601.01 <i>K</i>	601.30 <i>K</i>	601.30 <i>K</i>	601.30 <i>K</i>
700 <i>K</i>	702.10 <i>K</i>	702.69 <i>K</i>	702.69 <i>K</i>	702.69 <i>K</i>
800 <i>K</i>	803.92 <i>K</i>	805.02 <i>K</i>	805.02 <i>K</i>	805.02 <i>K</i>
900 <i>K</i>	906.80 <i>K</i>	908.71 <i>K</i>	908.71 <i>K</i>	908.71 <i>K</i>
1000 <i>K</i>	1011.13 <i>K</i>	1014.24 <i>K</i>	1014.24 <i>K</i>	1014.24 <i>K</i>
1200 <i>K</i>	1226.16 <i>K</i>	1233.48 <i>K</i>	<i>N/A</i>	1233.48 <i>K</i>
1400 <i>K</i>	1454.09 <i>K</i>	1469.23 <i>K</i>	<i>N/A</i>	1469.23 <i>K</i>
1600 <i>K</i>	1701.82 <i>K</i>	1730.31 <i>K</i>	<i>N/A</i>	<i>N/A</i>
1800 <i>K</i>	1978.33 <i>K</i>	2028.24 <i>K</i>	<i>N/A</i>	<i>N/A</i>
1900 <i>K</i>	2130.82 <i>K</i>	2195.43 <i>K</i>	<i>N/A</i>	<i>N/A</i>
2000 <i>K</i>	2294.98 <i>K</i>	2377.54 <i>K</i>	<i>N/A</i>	<i>N/A</i>
2100 <i>K</i>	<i>N/A</i>	<i>N/A</i>	<i>N/A</i>	<i>N/A</i>
2200 <i>K</i>	<i>N/A</i>	<i>N/A</i>	<i>N/A</i>	<i>N/A</i>

### 5.3 Impact on Radical Concentration

The number density of the  $OH$  was calibrated from the  $LIF$  signal using a Hencken Burner with a near-stoichiometric methane-air mixture in the weakly excited  $OH$  fluorescence regime. The uncertainty of the resulting  $OH$  number densities is estimated as  $\pm 20\%$  of the indicated value. This accounts for the uncertainty of the calibration number density (from the original absorption measurements) and for the application of the calibration to these flames (accounting for differences in quenching rates, temperatures, laser sheet intensity, etc.). In Figure 5.3, the  $OH$  number density is plotted for different  $DC$  currents, total flow rates and equivalence ratios for the premixed mode. In the left portion of Figure 5.3, the equivalence ratio is fixed while  $DC$  current and total flow rate change. The data points are taken at a fixed height in the center of the reaction zone (shown in the insert) where  $OH$   $LIF$  is most intense. For low total flow rates (6  $LPM$ ), the flow is not strong enough to propagate the nano-second arc discharge to the end of the plasmatron chamber, and most of the fuel is partially oxidized inside the chamber resulting in a low  $OH$  concentration above the tip. It is clear that with higher  $DC$  currents (higher  $DC$  power), the  $OH$  number density increases almost linearly with the input power. For different total flow rates, it is noticeable that all  $OH$  number densities at 100  $mA$  are less than  $10^{16} \text{ cm}^{-3}$ , which is the typical  $OH$  production level in a Bunsen flame without plasma enhancement. This is an indication

that the plasma is mostly acting to dissociate and preheat the fuel inside the arc chamber and that combustion outside is generally not influenced by the discharge.

It can be seen from Figure 5.3 (top) that  $OH$  is highest with an equivalence ratio of 0.8 and is less at values of 0.9 and 1.0 [67, 69]. This is due to the fact that  $OH$  production in this case is a combination of direct coupling of the mixture inside the chamber and partial coupling after exiting the torch, and higher  $OH$  concentration in lean conditions indicates that the oxidation of lean mixtures extends further out to the tip. The increase of  $OH$  number density with  $DC$  power levels is a direct influence of the plasma chemistry such as the additional oxidation of product water vapor ( $H_2O$ ) by electron impact.  $H_2O$  plays an active role in the production of active radicals through direct electron impact disassociation:  $e+H_2O\rightarrow H+OH+e$ ; and reaction with  $O(^1D)$  disassociated from  $O_2$ :  $O(^1D)+H_2O\rightarrow 2OH$ ,  $e+O_2\rightarrow O(^1D)+O+e$  [84]. These radicals in turn result in increased  $OH$  production which can offset termination reactions when the  $DC$  power is raised.

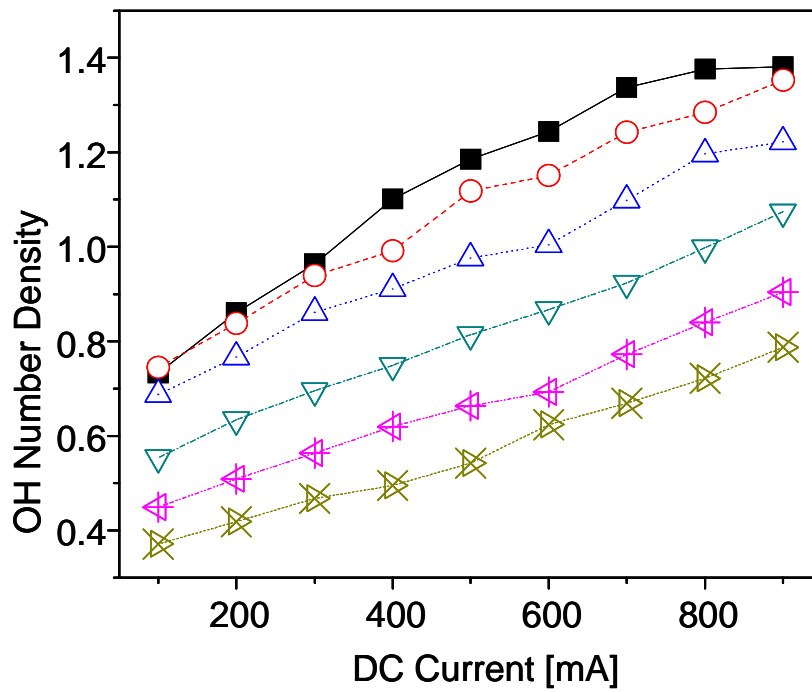
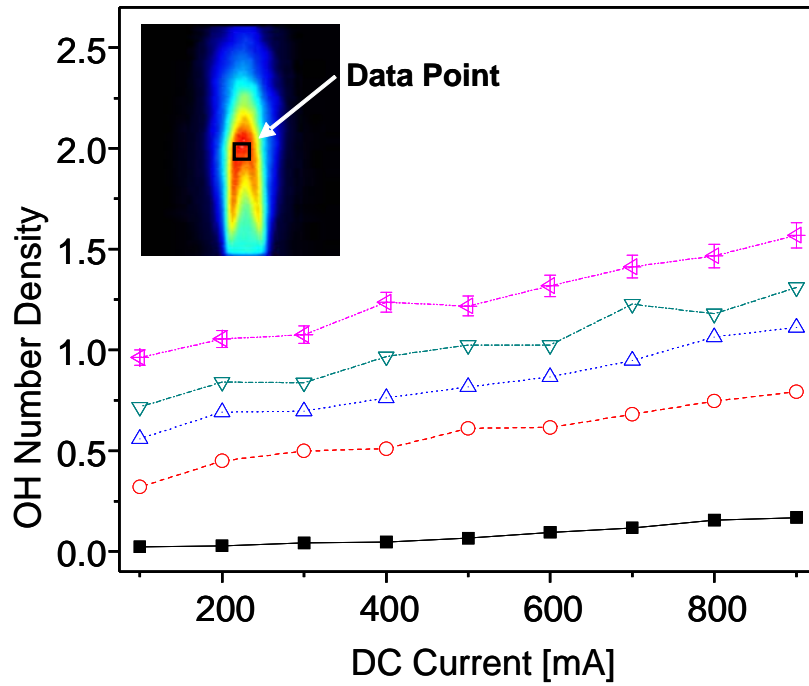


Figure 5.3: *OH* number density is plotted for different *DC* currents, total flow rates (top, equivalence ratio is fixed at 0.95 and for different *DC* current, equivalence ratios (bottom, total flowrate is fixed at 15 *LPM*) in premixed mode.

A first order comparison of *OH* densities for both premixed and nonpremixed flames is shown in Figure 5.4. In this plot, the *OH* number densities are shown at the same flow rates, but with increasing levels of power input for both flame geometries. For the premixed flame, the data is extracted from a central location identical to that shown in Figure 5.3. For the nonpremixed flame, the data is extracted from two locations, representing the inner and outer cones, as shown in the insert of Figure 5.4.

*OH* number density in the premixed mode increases by almost 100% from 100 *mA* to 900 *mA* of *DC* current input. In contrast for nonpremixed flames, *OH* number density remains relatively stable on the outer flame front and is close to the Burner flame *OH* production rates, which indicates that outer flame has little influence from the inside air discharge. However, the *OH* number density in the inner flame front shows an incensement of about 750% percent and the highest *OH* number density reaches over  $3 \times 10^{16} \text{ cm}^{-3}$ , which is more than twice that of the *OH* production of a premixed flame for the same condition. This shows that much of the flame enhancement for the nonpremixed flame is carried out at the inner flame front, as the power is enhanced. For the inner flame, the significant increase in *OH* number density comes from the active excited species in the air discharge exiting the plasma chamber, including atomic oxygen, which has been previously documented as a significant factor for flame enhancement [7] and a cause for increased *OH* concentration.

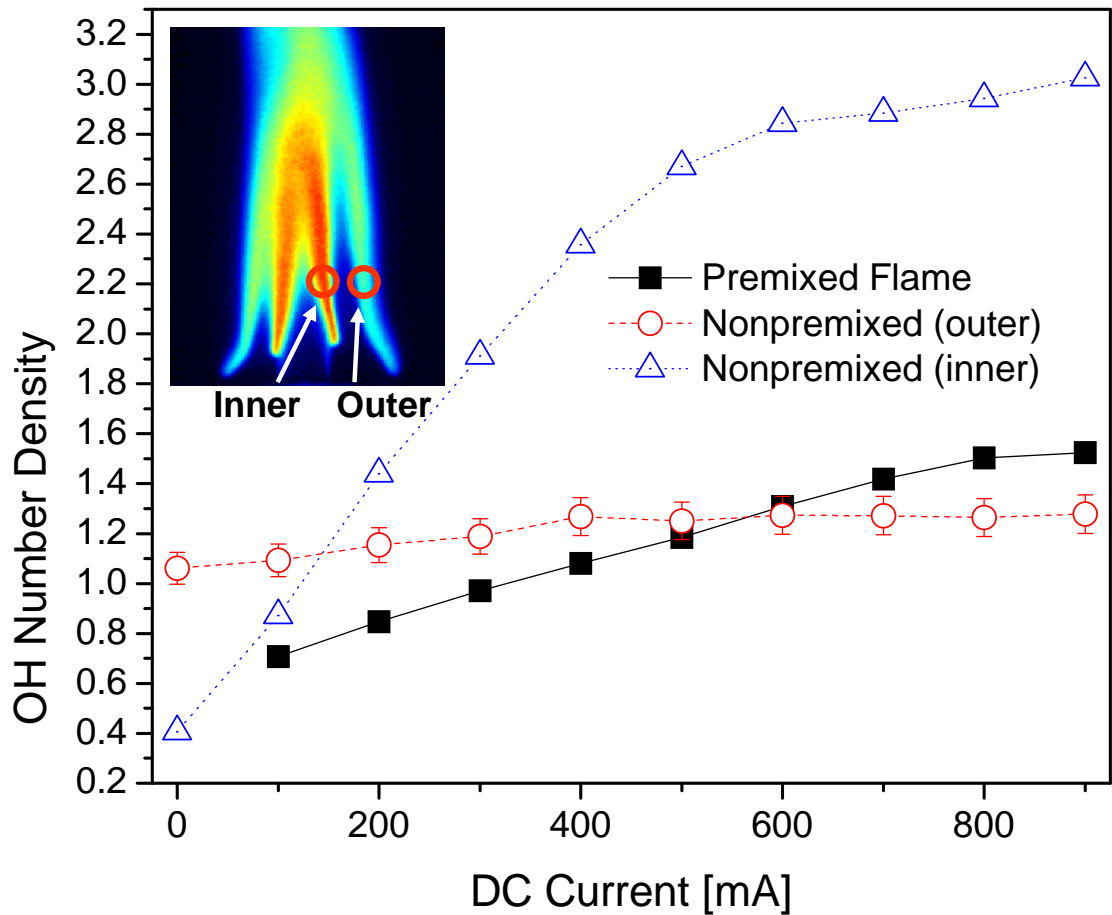


Figure 5.4:  $OH$  number density with the same flow conditions (total flow rate is 9  $SLPM$ , and  $\phi=0.95$ ) but different currents for both premixed (from data point the same as in Figure 5.3) and nonpremixed (two data points, one outer flame front and the other one inner flame front as shown) flames.

#### 5.4 Flame Stability, $CO$ Formation and Energy Efficiency

The influence of geometry and other parameters on the flame stability can also be observed from  $OH$  PLIF images. Figure 5.5 shows averaged  $OH$  PLIF images for both premixed and nonpremixed flames at various flowrates and equivalence ratios. The top row shows a premixed flame with a rate of 12  $SLPM$ , with equivalence ratios of  $\phi=0.7$ ,

1.0 and 1.3. The bottom two rows show nonpremixed mode flowrates of 6 *SLPM* (middle)/15 *SLPM* (bottom) with overall equivalence ratios of  $\phi = 0.7, 1.0$  and 1.3. In the premixed mode, the figures represented here are generally reproduced for all the flowrates where the flame is stable at the end of the plasmatron tip for leaner conditions; however, the flame tends to lift off at higher equivalence ratios ( $\phi = 1.3$ , top row in Figure 5.5).

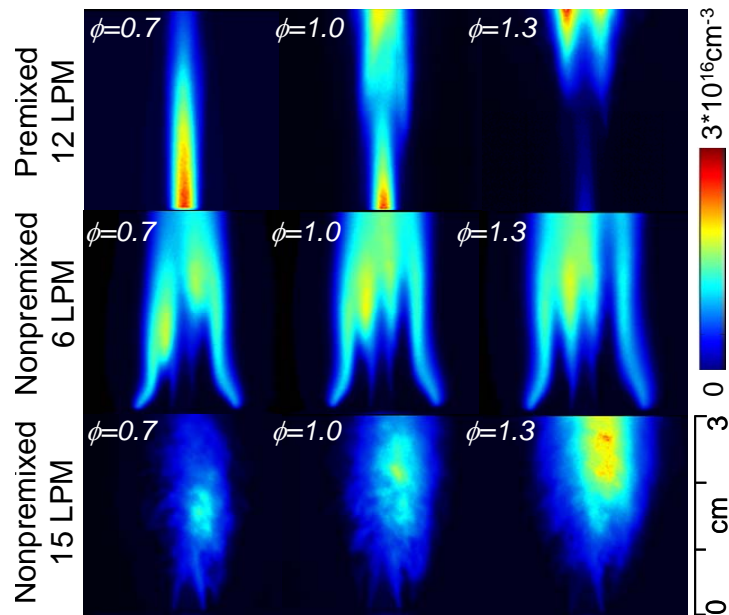


Figure 5.5: Averaged *OH PLF* images for all flowrates at premixed mode with  $\phi = 0.7, 1.0$  and 1.3 (top); Averaged *OH PLF* images for 6 *LPM* (middle)/15 *LPM* (bottom) at nonpremixed mode with  $\phi = 0.7, 1.0$  and 1.3.

At high equivalence ratios, the radical pool is poorly established and fuel/air mixture tends to react more with the ambient air resulting in combustion downstream of the exit. Nonpremixed flames at low (6 *SLPM*, middle row in Figure 5.5) do not reflect this phenomenon, and the flame is stable over a wide range of equivalence ratios. For

higher total flowrates (15 *SLPM*, bottom row in Figure 5.5), the stability of the nonpremixed flame is compromised; the outer flame is no longer visible in the turbulent structure and the two flame zones merge into a single structure. The stability for these two configurations is different in that the premixed mode appears to be more chemistry driven and dependent on the equivalence ratio whereas the nonpremixed mode is more dependent on the flowrates and the physical interaction of the fuel and the plasma discharge. Overall, the premixed mode can stabilize higher flowrates, but the smaller dimensions of the combustion and sensitivity on the fuel and air ratios can render the premixed mode more difficult to use.

The *CO* number density is measured using two-photon-absorption *LIF* (*TALIF*) to investigate the in-situ reforming into carbon monoxide (*CO*) and hydrogen (*H<sub>2</sub>*), which is believed to be a key mechanism for flame stabilization [9]. *CO* was measured with two-photon *PLIF*, using the  $B^1\Sigma^+ - X^1\Sigma^+$  (0,0) transition at 230.10 *nm* [63]. A Sirah Precisionscan LG-2400 dye laser was pumped by the 532 *nm* beam from a *Q*-switched Nd:YAG laser. The 653-*nm* output of the dye laser was sum-frequency-mixed with the third harmonic beam (355 *nm*) from the injection seeded Nd:YAG laser to produce an 18 mJ/pulse of 230-*nm* radiation (linewidth of  $\sim 0.1 \text{ cm}^{-1}$ ). *CO* fluorescence is then detected at 486 *nm* using an intensified *CCD* camera fitted with an interference filter (10 *nm FWHM*).

In Figure 5.6, averaged *CO PLF* images for premixed (insert top row) and nonpremixed (insert bottom row) are shown, and *CO PLIF* intensity are plotted for both

modes with equivalence ratios of  $\phi=0.7$  and 1.1. Due to the two-photon excitation of the  $CO$ , the quality of the  $LIF$  signal for the non-linear process is not as high as that of  $OH$ . Coupled with a more diffused profile of  $CO$ , the  $LIF$  signal did not resolve the two cones of the nonpremixed flame. It should be noted that because of the weak absorption, the laser sheet is smaller and more focused near the center, therefore a dramatic drop of  $CO$  downstream is an artifact of the laser sheet.

For the lower portion of Figure 5.6, the  $CO$   $PLIF$  signal intensity is corrected for the quadratic dependence [85] on the laser power to reproduce a relative  $CO$  number density (a.u.). since the irradiance is not high enough for photoionization to exceed quenching in our case to influence the quadratic dependence [86]. We assume that the increase of  $CO$  in the reaction zone is indicative of in-situ fuel reforming, which may not be reflected in the overall byproduct as conversion to  $CO_2$  occurs. For both modes, the  $CO$   $LIF$  intensity is shown to increase with increased  $DC$  current input. It is clear that for nonpremixed and premixed flames,  $CO$   $LIF$  intensity for rich flames ( $\phi=1.1$ ) is higher than lean flames ( $\phi=0.7$ ).

Comparison between  $CO$  number densities of premixed and nonpremixed flames with an equivalence ratio of 0.7 indicates that higher fuel reforming is observed for the nonpremixed flame over the entire range of powers used. This is expected as a very rich interface is established in the nonpremixed flame between the plasma discharge and the fuel. For both flame configurations, we see a gradual rise in  $CO$  as the power is increased. This additional  $CO$  generated from the in-situ reforming of the fuel will

contribute as a major mechanism for flame stabilization by increasing the mixture hydrogen content. We assume that the *CO* increase also indicates temporary increase of hydrogen. Increase of *CO* is about 30 *a.u.* in the premixed flame and 40 to 50 *a.u.* in the nonpremixed mode for the same conditions over the power range 0 - 800 *mA*.

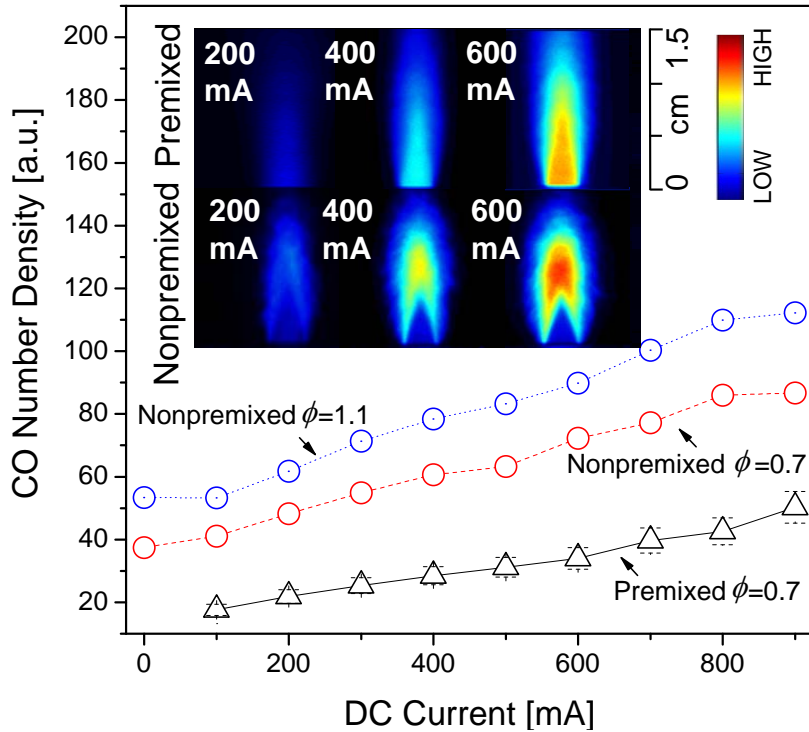


Figure 5.6: Averaged *CO* PLF images for premixed (insert top) and nonpremixed (insert bottom); *CO* number density is plotted for with equivalence ratio 0.7 (premixed and nonpremixed) and 1.1 (nonpremixed).

For plasma assisted combustion, energy consumption (energy needed for the same amount of air with the same current) during the coupling process is a critical parameter. This parameter can be analyzed by comparing of both modes with the air discharge case. Figure 5.7 shows the actual input power as a function of input current under identical flow conditions. It is clear that most power is required for the air-only plasma because

significant energy is required for dissociation, ionization, and vibration excitation of nitrogen, resulting in significant  $NO_x$  generation [87]. When combustion is present, the breakup of the nitrogen is assisted by the exothermic reactions involving the fuel. Thus, the ionization threshold is lowered. Therefore, the conversion efficiency to  $H_2$  and  $CO$  is increased.

In the premixed mode at lower currents, power consumption is lower as fuel is injected into the discharge chamber and in-situ breakup of  $CH_4$  molecules and the plasma impact reactions further accelerate the reaction chemistry. The study in the next chapter shows that with combustion,  $NO$  production is reduced by an order of magnitude less, meaning much less energy is used to break the  $N-N$  bond in Nitrogen. At higher  $DC$  currents, the power consumption for premixed and nonpremixed flames is seen to converge as plasma impact and fuel breakup are eventually saturated for both cases.

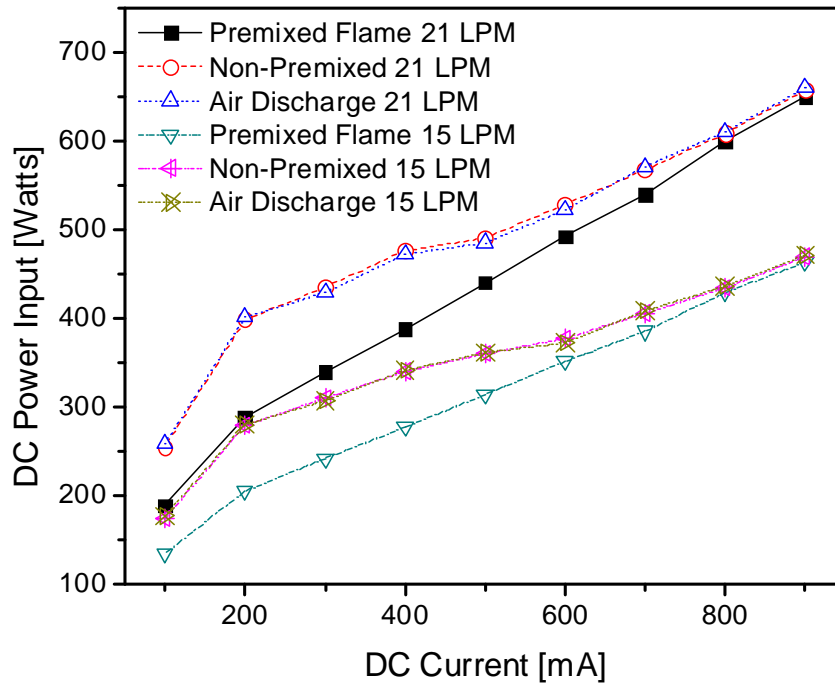


Figure 5.7: DC Power input with different current for air plasma, premixed flames and nonpremixed flames.

## Chapter 6, Nitric Oxide Formation in a DC Plasmatron

### 6.1 Nitric Oxide Formation in Flames

Generally, *NO* formation in conventional combustion is due to four main processes [13, 14]: (1) thermal (Zeldovich) mechanism which occurs at high temperatures because of high energy required for dissociation of the nitrogen molecule (reactions 1,2 and 3); (2) prompt mechanisms with important intermediate species *HCN* and *NH* (reactions 4 and 5); (3) *N<sub>2</sub>O* mechanism which involves third body collision (reactions 6, 7 and 9); and (4) fuel-bound nitrogen mechanism where nitrogen is supplied from the fuel itself. *NO* can also be removed by reacting with hydrocarbon radicals in rich flame through a process known as '*NO* reburn' [15], of which some of the key reactions are also listed in Table 6.1. *NO<sub>x</sub>* emission in a conventional combustion is highly dependent on temperature as shown in Figure 6.1. When temperature is high (higher than 1,800 K), most Nitric Oxide from traditional combustion is from Thermal (Zeldovich) mechanism.

Coupling high temperature reactive flows with a nonequilibrium plasma discharge can lead to significant changes in the formation of nitric oxide (*NO*), one of the most problematic combustion effluents and a critical design parameter for all practical combustion systems. The key mechanisms involved in the *NO* chemistry for plasma discharges and methane flames are shown in Table 6.1.

Table 6.1: Reactions for NO formation in methane/air flame in plasma

Thermal (Zeldovich)mechanism	$O+N_2 \leftrightarrow NO+N$	1
	$N+O_2 \leftrightarrow NO+O$	2
	$OH+N \leftrightarrow NO+H$	3
Prompt mechanisms	$NH+O \leftrightarrow NO+H$	4
	$CN+O_2 \leftrightarrow CO+NO$	5
Mechanism involving $N_2O$	$O+N_2+M \leftrightarrow N_2O+M$	6
	$N_2O+O \leftrightarrow NO+NO$	7
Other reactions to form $NO$	$NNH+O \leftrightarrow NO+NH$	8
	$N_2+e \leftrightarrow N+N+e$	9
Electron and Ion Reaction	$N_2O+e \leftrightarrow NO+N+e$	10
	$NO+e \leftrightarrow N+O+e$	11
	$N_2O+e \leftrightarrow N_2+O+e$	12
	$NO_2+e \leftrightarrow NO+O+e$	13
Excited State Species Reaction (*: excited state)	$O+N_2^* \leftrightarrow NO+N$	14
	$NO_2+N_2^* \leftrightarrow NO+N_2+O$	15
$NO$ Reburn mechanism	$N(^2D)+O_2 \leftrightarrow NO+O$	16
	$HCCO + NO \leftrightarrow HCN + CO_2$	17
	$HCCO + NO \leftrightarrow HCNO + CO$	18
	$CH + NO \leftrightarrow HCN + O$	19
	$CH_3 + NO \leftrightarrow HCN + H_2O$	20
	$CH_3 + NO \leftrightarrow H_2CN + OH$	21
	$NH_2+NO \leftrightarrow N_2+H_2O$	22

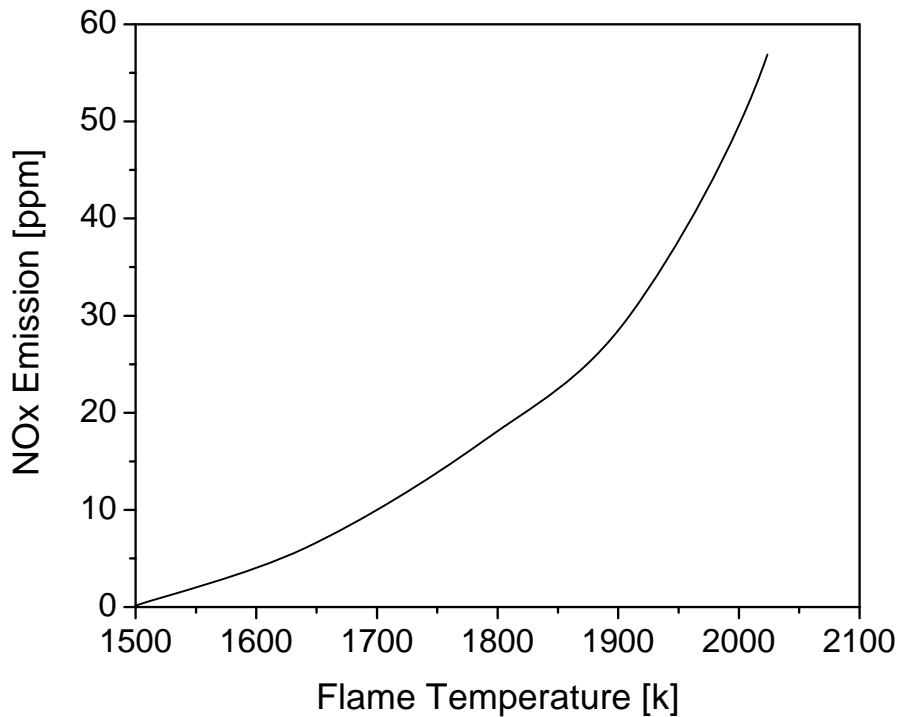


Figure 6. 1 *NOx* emission as f function of combustion temperature [30, 88]

In the case where no combustion is involved and there is only a plasma discharge, formation of *NO* from air varies depending on the discharge system. For example, reaction 14 can be the principal *NO* formation pathway in pulsed discharge with shorter time scales ( $10^{-8}$ – $10^{-6}$  seconds) [89] while reaction 16 is shown to be dominant in corona discharges [90]. For variety of reduced electric fields, different percentage of energy deposition into air goes to elastic losses, ionization,  $N_2/O_2$  electronic states,  $N_2/O_2$  vibration [34], resulting in different pathways for *NO* formation.

In plasma assisted combustion, analysis of the *NO* formation mechanism becomes difficult to determine as energy distribution of individual molecules can deviate from

thermal equilibrium and the relationship between the *NO* production and deposition of heat is unclear. More importantly, high electron density generated by the electric field gives rise to new electron and ion impact processes which can enhance the propagation and branching of radicals and ultimately accelerate *NO* production. *NO* formation in plasma assisted combustion could be formed both from the thermal mechanism due to high combustion temperature and plasma particle reactions, especially reactions 14, 15 and 16 due to high energy for dissociation of nitrogen. As *NO* formation is a major concern for all practical combustion systems, accurate methods to measure *NO* formation in the reaction zone is important to the continued development of plasma enhanced combustion systems, and a task which can benefit from the extensive research already available on *NO* formation of both combustion and plasma systems, respectively.

## 6.2 Quantification of Nitric Oxide

Imaging of *NO* using *LIF* is a well established tool in combustion diagnostics [91]. Therefore, a detailed discussion of the relevant spectroscopy is omitted but it should be noted that we are using an excitation at 226.03 nm which has been previously noted as being well isolated from interference of  $O_2$  [92, 93] even in high-pressure flames where the problem is most pronounced. This excitation line, composed of  $P_1(23.5)$ ,  $Q_1+P_{21}(14.5)$  and  $Q_2+R_{12}(20.5)$  transitions, has a moderate temperature dependence over typical combustion temperatures between 1700 and 2300 K. In this section, we focus

on three other issues of practical importance: quantification of *NO* concentration, signal distortion due to thermal nonequilibrium and temperature field imaging.

Quantification of the *LIF* signal can be a difficult task as it is not only dependent on *NO* number density, but also on the optical setup and potential interference from alternative species. The approach used in this study here is to calibrate the signal using a well defined flat flame torch using a variable *NO* seeding method [94]. The calibration torch is made by fitting a 50 micron sintered plate into a 1 *cm* diameter stain steel pipe in order to stabilize a flat *I-D* flame and seed various levels of nitric oxide. The *LIF* is measured at two different excitation wavelengths, which have minimal and maximum *NO* signal strengths, respectively as illustrated in Figure 6.2. The plot shows a magnified view of the small box in the inserted graph. The *NO* addition is varied from 200 to 600 *ppm* and *NO-LIF* is detected with excitation at two different wavelengths. Excitation 1 and 2 refer to two different excitation wavelengths ( $\lambda_1$ : 226.030 *nm*,  $\lambda_2$ : 226.042 *nm*).

These wavelengths are selected relatively close together in the target scan range where the baseline intensity, if present, can be assumed to be constant for a given pressure. After measuring the total signal at two different wavelengths at several different *NO* seeding concentrations, the overall signal is linearly fit as a function of *NO* seeding for each of the excitation wavelengths. These two linear fits are extrapolated to their intersection yielding the nascent *NO* concentration and the value of the baseline signal. Determination of the nascent *NO* concentration (and *LIF* baseline) by this method assumes the *NO* reburn mechanism is first order in *NO* concentration, as evidenced by the

linearity in Figure 6.2. In the stoichiometric and lean flames studied here with less than 100 ppm NO addition, the NO reburn is expected to be linear in NO concentration and of no significant amount [95, 96]. It has also been shown that temperature in typical flames does not vary ( $\leq 2\%$ ) for NO additions as large as 1000 ppm [94]. In all the cases, NO is being weakly excited and no saturation effects are observed with our laser power.

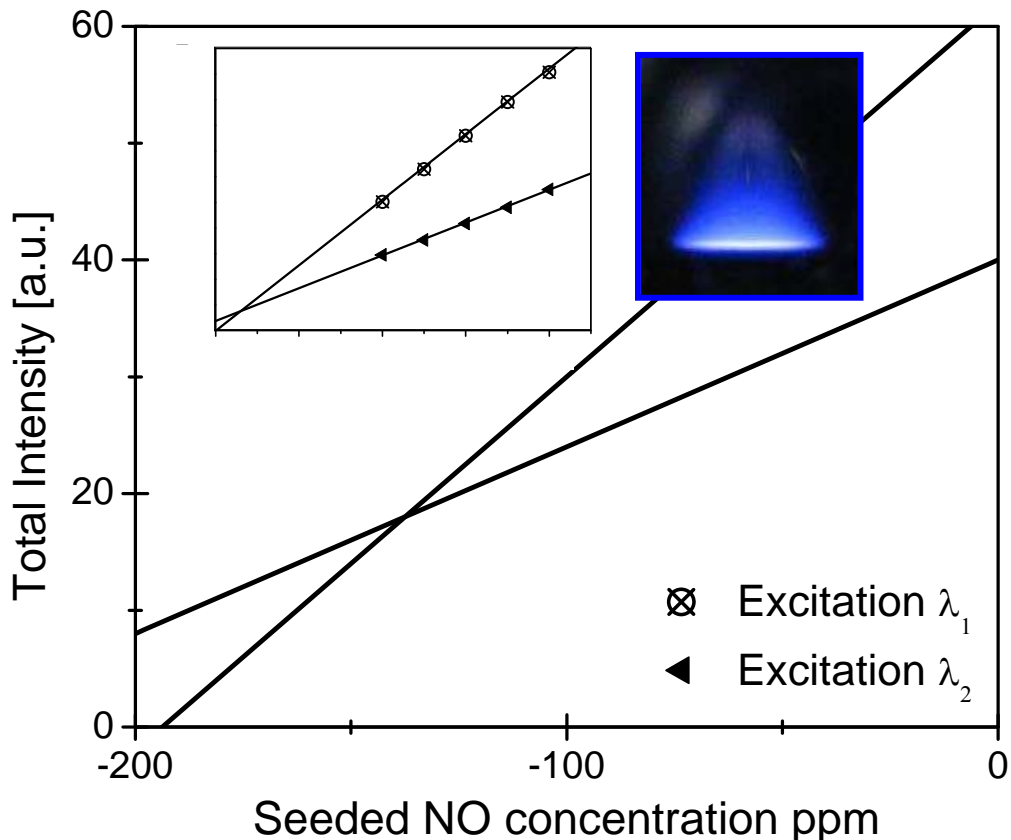


Figure 6.2 NO addition method for determination of the baseline strength and the nascent NO concentration.

### 6.3 Temperature Profile Measurements

A 2-D temperature profile is measured using an IR camera and shown in Figure 6.3.

From the temperature profile, we can see a rise of reaction zone when equivalence ratio is

increased from lean (0.7) to rich (1.2). Also from the figure, we also can see the turbulence of the combustion. The *IR* thermometry is a method for relative 2-*D* profile and we need some more accurate way to calibrate for higher accuracy. In this research, I used multi-line *NO LIF* thermometry. The data point for calibration is shown in Figure 6.3 with a circle on the upper right.

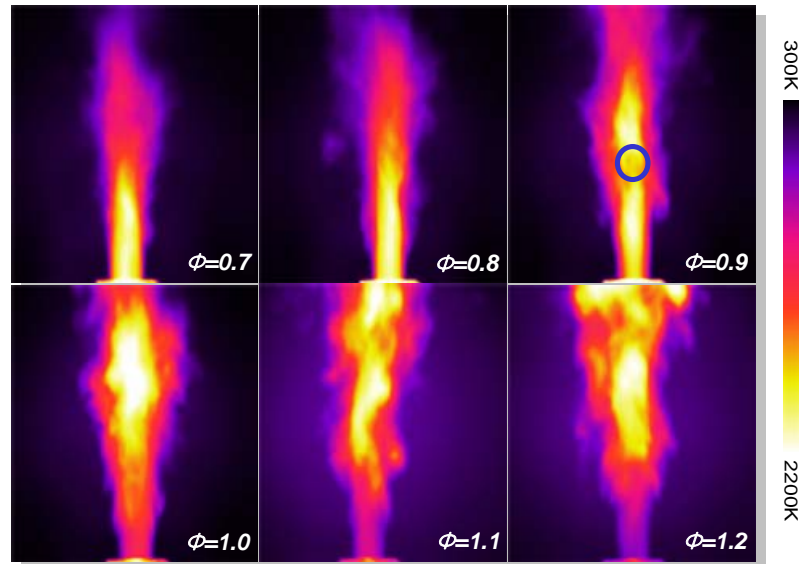


Figure 6.3 *IR* temperature profile with different equivalence ratio for premixed methane and air flame with circle shown in the figure where the multi-line thermometry calibration is used.

Another effect which can significantly influence the LIF signal is the nonequilibrium distribution of the rotational states in the *NO*. Generally, for most plasma enhanced combustion systems at atmospheric pressure, it is assumed that the *NO* in the flame region will follow a Boltzmann distribution of the rotational states and therefore in thermal equilibrium. In our studies, this was tentatively confirmed by comparing signal strengths from a number of varying rotational states, where the intensity generally

followed the nitric oxide concentration within 2%. However, for systems where highly nonequilibrium plasma energy is coupled at lower pressures, the impact of deviation from a thermal equilibrium of the rotational energy  $E_{\text{rot}}$  on the LIF signal should be considered.

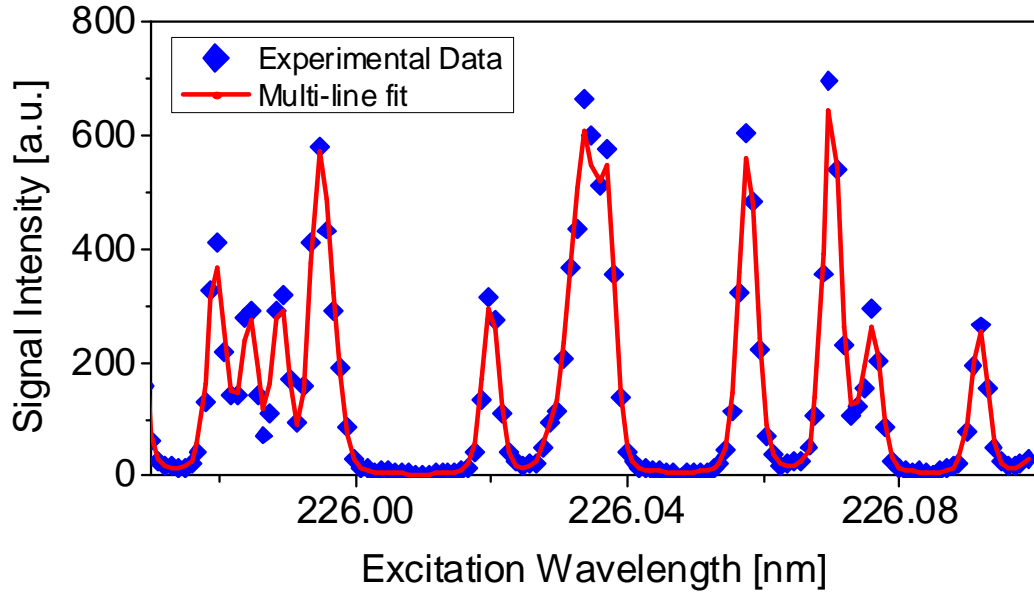


Figure 6. 4 Multi-line *NO LIF* thermometry (126 transitions between 225.975 nm and 226.1 nm).

To accurately calibrate the signal intensity for both concentration and spatial variation, we need to acquire information regarding the temperature. It is needed to correct for the temperature variation of the *NO LIF* signal via the temperature dependence of the laser-excited ground state population, the spectral overlap between the laser-spectral profile and *NO* absorption spectrum, and the fluorescence yield. In this study, we use IR thermometry for determination of temperature fields, which measure temperature using gray body radiation (infrared) emitted from reacting gases over the

whole viewing area. IR emission from excited species also adds to the intensity of the figure, but it would be lower than gray body radiation and also an rough indication of temperature. The images are then calibrated at a single point using a multi-line *NO LIF* thermometry [97] which is based on excitation of multiple transitions by scanning the wavelength of the laser over a wide spectral region and then fitting the excitation profile with a numerical simulation. An example of the multi-line *NO LIF* thermometry method is shown in Figure 6.4. This provides highly accurate temperatures at a single point which can be used to correct for the less accurate temperature images obtained through the IR thermometry.

The model used for the fitting is LIFSim [53]. LIFSim is a multi-level spectroscopic simulation of nitric oxide for the  $A-X$  transition during laser absorption and spontaneous fluorescence. It is particularly well calibrated for the  $A_2\Sigma^+ - X_2\Pi (0,0)$  transition where data for term energies, transition energies, transition strengths, collisional line broadening and shifting, quenching, and energy transfer terms are well known. For use of *LIFSim* in our studies, we must assume thermal equilibrium (or understand subsequent internal energy modes) of the flame, which can be made as the reaction zone outside the torch is far from the arc chamber where all the non-equilibrium effects are dominant. *LIFSim* is also used to account for temperature dependence of the *LIF* signal as will be discussed in the following sections.

## 6.4 Planar Laser-Induced-Fluorescence (*PLIF*) Imaging of *NO*

*2-D NO PLIF* images are taken for discharge only in air without combustion over a range of flow rates and discharge powers. For plasma enhanced methane/air combustion, images are taken as a function of flow rate, discharge power and equivalence ratio. The laser sheet propagates through the center of the plasma torch exit and the emission is synchronized with the intensified *CCD* camera. In order to correct for the laser energy fluctuations, every image is calibrated by the corresponding laser pulse energy, collected using a fast speed photodiode (LaVision). As the gas flow is turbulent, 200 images were averaged when comparing the *NO* formation for different operating conditions. Averaged images also allow us to accurately calibrate the signal over the imaging field as a function of temperature by using averaged IR thermometry.

*2-D NO PLIF* signal intensity is not only affected by the laser pulse power, but also the nonuniformities in the laser sheet profile and from the spherical aberration of the lens. Emission from a fluorescent *UV* glass was used for the laser sheet corrections, and the spherical aberration is corrected using an algorithm from the Davis software (LaVision) based on a pre-shot grid. Both single shot and averaged *2-D NO* concentration images from *NO PLIF* of discharge only in air as a function of different plasma power and stoichiometric methane/air flame with different plasma power are shown in Figure 6.4. In both figures, you can observe the two plasma plumes coming out from either side of the torch.

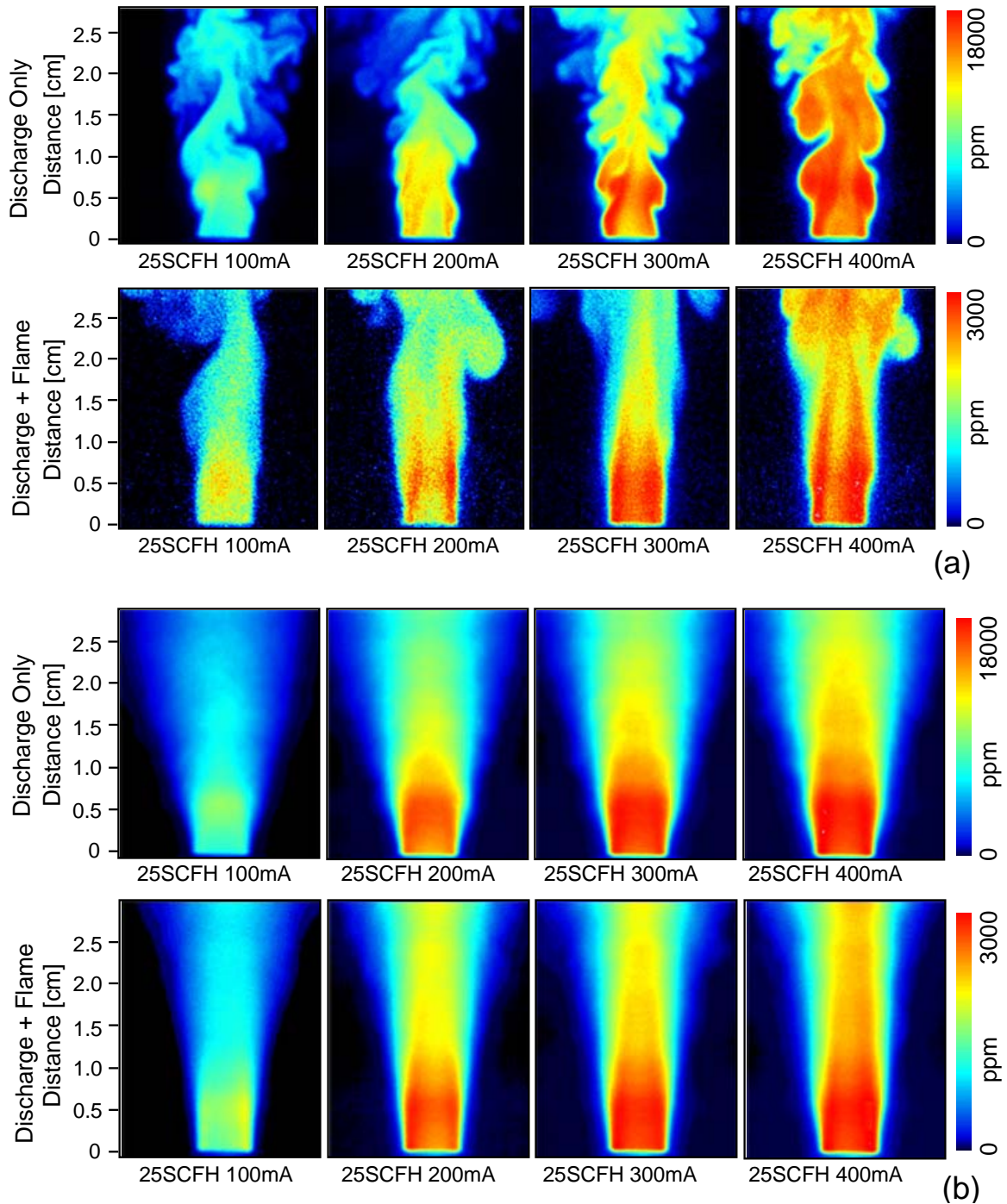


Figure 6.5 Single shot  $NO$  concentration fields using  $NO$  PLIF of gas discharge of air and plasma enhanced flames with different plasma power at same gas flow rate (a). Averaged  $NO$  concentration fields from  $NO$  PLIF (200 images averaged) of plasma enhanced flames with different plasma power at same gas flow rate (b).

It can be seen from the Figure 6.5 that turbulent flows exists in both discharge-only and plasma enhanced combustions for our plasmatron. The degree of instability is observed to be more severe in plasma discharge only cases for the same conditions, as the plasma assisted combustion is more energetically driven by the additional chemical heat release. For the single shot images, it can be seen that the plasma only case (upper) row has images which are smoother in quality due to the higher levels of the *NO* signal which results in higher Signal to Noise Ratio (*SNR*). Additionally, it should be noted that *NO* formed near the flame front is diffused along with the flow and is reduced about 30% to 40% from the highest concentration to a distance of 2.5 *cm* from the plasmatron exit.

## **6.5 Temperatures and *NO* Concentrations in Plasma Discharge Only**

In order to compare the *NO* formation between different operational conditions, we present both temperature and *NO* concentration at a specific location in our image as shown in Figure 6.6 for a plasma discharge only case. The location was chosen as a single point in the center of the flame where a stable and high temperature region exists due to the convergence of the two plasma plumes from either side of the torch. In order to obtain the temperature at this location, multi-line *NO LIF* thermometry is used for higher accuracy.

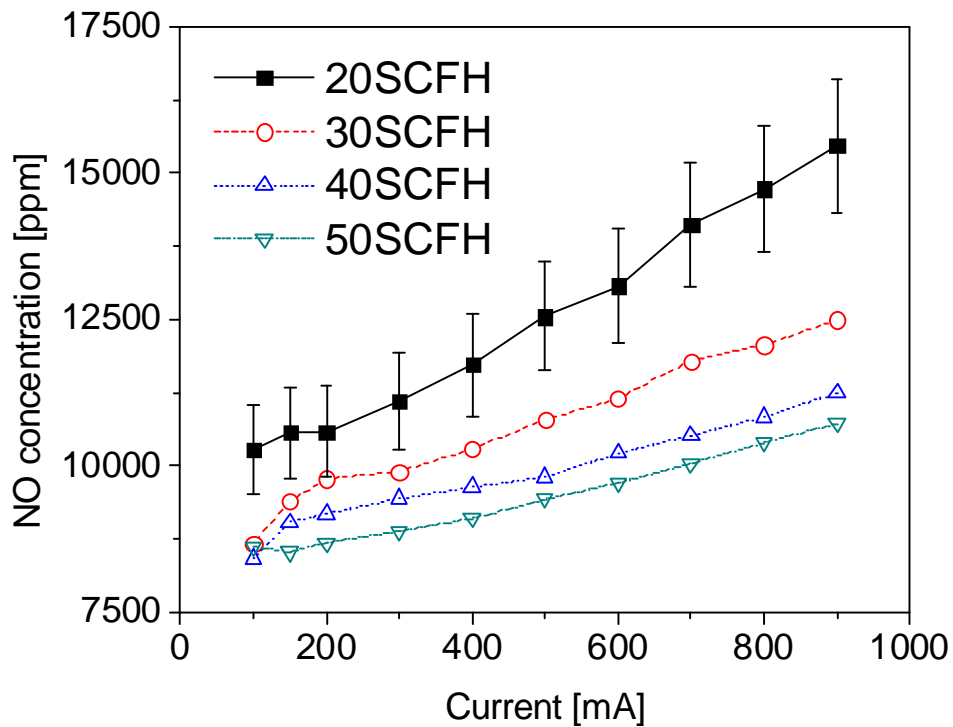
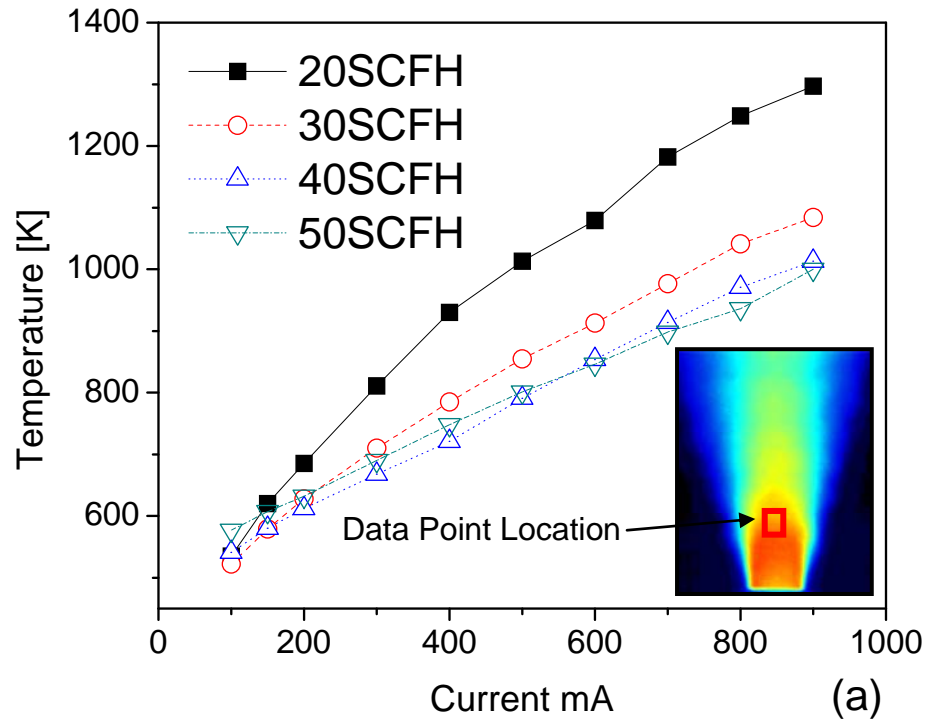


Figure 6.6 Temperature (a) and *NO* concentration (b) data at specific location of the discharge for different power levels and air flow rates in discharge only case in air.

*NO* concentration in the discharge plasma is quantified by the following process. First the *NO LIF* intensity value (calibrated for both laser sheet nonuniformity and laser pulse energy) is taken from an averaged image of 200 laser shots. Using the temperature information provided from *NO-LIF* thermometry, the signal is calibrated for temperature dependence of the *NO* excitation by using a multi-level excitation and fluorescence model, *LIFSim* [53]. Note that we have verified that we are operated in the linear (weak) excitation region and free from saturation effects. The *LIF* signal at this point is linear to the number density of *NO* (molecules/cm<sup>3</sup>), and we apply the following relationship to convert it into a mole fraction based concentration (molecules/total molecules). The final signal is then quantified using a *NO* addition method previously described.

$$I_{LIF} \sim N_{NO} = X_{NO} \times \frac{p}{kT} \quad (6.1)$$

$I_{LIF}$  is *NO LIF* signal intensity,  $N_{NO}$  is the number density and  $X_{NO}$  is the mole fraction of *NO*.

The uncertainty in the temperature measurements affects the concentration measurements through the mole fraction/number density correction in *LIF* equation, and also through calibration of the *LIF* signal temperature dependence using *LIFSim*. The temperature uncertainty is within 1% for our measurement techniques at atmospheric pressure. This is because the quenching terms in *LIFSim* for the low temperatures as that in the plasma discharge has larger errors. The uncertainty associated with beam energy fluctuation corrections and wavelength shift of the laser is expected to be less than 1%.

Camera readout error was suppressed by subtracting a background image taken without the laser pulse and can be neglected. Another component of uncertainty comes from the fact that the quenching coefficient used to determine the *LIF* strength in *LIFSim* lacks accuracy at low temperatures in discharge only case (<5%). Combined with the errors from the flowmeters and shot noise (due to statistical fluctuation of finite number of signal photos reaching the *CCD* array), the overall uncertainty is expected to be ~7.4% in the *NO* concentration measurements for plasma discharge and ~4.7% for plasma assisted combustion.

Figure 6.6 shows temperature and *NO* concentration plots with different gas flow (20 to 50 *SCFH*) and average current (100 to 900 *mA*). The temperature and *NO* concentration data is extracted from a region 10 mm from the top of the plasma torch with an area of 2.56 mm X 2.56 mm (40 pixel X 40 pixel with resolution of 64 *um* X 64 *um* per pixel). The amount of *NO* production is significantly large due to the large energy input (200 to 700 *Watts*). As the temperature range for all conditions lies within 550 to 1300 *K*, *NO* production from the thermal mechanism is considered to be small in this low temperature range. Moreover, the system lacks carbon and hydrogen compounds required for prompt *NO* production. Therefore, we can conclude that the possible dominant *NO* production mechanism is the electron and excited state species (i.e., oxygen) impact reactions which lead to dissociation of  $N_2$  and also possible *NO* formation reactions from  $N_2O$ . In Figure 6.6 (b), *NO* production increases with current/power and inversely with air flow. The same general trend is shown in the temperature plot. As formation of *NO*

from  $N_2O$  is expected to increase as temperature is decreased, it seems to be of little impact here indicating that the most dominant mechanism for  $NO$  production is the electron, ion, and excited state species impact reactions.

It is apparent in Figure 6.6 (a) that temperature increases with current, as a result of more energy per volume of gas. At the same time, temperature drops when the air flow is raised as the gas resident time in the discharge is reduced, leading to fewer collisions between excited particles and eventual lowering of the temperature even though the discharge power is actually higher at higher flow rates due to an increase in the average voltage. The voltage is shown to increase with increased flow rate (not plotted here) in our experimental setup where the flow rate is increased from 20 *SCFH* to 50 *SCFH*, corresponding to a gas speed increase from 8 *m/s* to 20 *m/s*. For all the gas velocities used here, the plasma plume is injected outside the torch and visually accessible although the initial breakdown is expected to occur inside the torch near the cathode.

For a typical *DC* discharge, a range between  $10^{-5}$  to 1 *A* is the normal glow regime, where the voltage will increase as the current increases [98]. Although it is not shown here, we have noticed that the voltage drops in our plasmatron when current is increased for the same flow rate, which leads us to assume weaker electric field but more spark channels to maintain the current. Discharge energy input to the system is not only from the electric field, but also thermal deposition from the higher temperatures. Table 6.2 shows the percentage of energy which goes to heating the gas flow at 20 *SCFH* in a current of 100 to 900 *mA*. Energy for heating the plasma gas is calculated using specific

heat  $C_p$  of air and assumes that temperature of the input gas is room temperature of 300 K. It can be seen that the percentage for heating the plasma gas increases with increased current which also means an increase total power input. The increase in the kinetic energy of the molecules and increased collisions further support that *NO* formation is predominantly from electron and ion impact reactions.

Table 6.2. Energy data of discharge only in air with different current

Current	Final Temperature	Voltage	Discharge Power	Power for heating	Heating Percentage
mA	K	kV	J/s	J/s	%
100	540	1.95	195	48	24.5
150	630	1.55	232.5	65	28
200	710	1.32	264	83	31.3
300	830	0.99	297	112	37.6
400	920	0.8	320	132	41.3
500	990	0.68	340	148	43.5
600	1050	0.6	360	163	45.3
700	1080	0.54	378	171	45.2
800	1170	0.49	392	193	49.2
900	1210	0.44	396	203	51.2

Voltage drop across the plasma column (from the end of the inner cathode) is about 500 to 1000 voltage for all the combustion conditions in this study and the length of the plasma column is about 4 mm. Therefore, the reduced electric field ( $E/n$ ) is calculated to be 50~85 Td ( $1 \text{ Td} = 10^{-17} \text{ V}\cdot\text{cm}^2$ ) for 500 to 1000 voltage, 1 atm and 4 mm. Reduced electric field is a measure of kinetic energy transfer cross-section from electrons to internal degrees-of-freedom molecules. For certain reduced electric field, appropriate molecular energy states is excited. For example, vibrational levels of the ground electronic state nitrogen, or low-energy electronic states of oxygen are more likely to be excited at lower  $E/n$  level, while high-energy electronic levels of nitrogen and oxygen, as well as in their dissociation and ionization for higher  $E/n$ . For this experiment, majority of the energy deposition into the air results in  $N_2$  molecule vibration (90% to 95%) excitation along with some  $N_2$  electronic states (~5%) while there exists little ionization, rotation or  $O_2$  vibrational/electric excited states [34]. Therefore, the main pathway responsible for large amount of  $NO$  production is  $N_2(v)+O \rightarrow NO+N$  in this case. This is consistent with kinetic model study of similar  $DC$  glow discharge with the same order in magnitude reduced electric field in [99].

We find that  $NO$  production in a  $DC$  plasmatron can be significantly high near the reaction zone and that the glow to spark transition strongly affects the  $NO$  production via increase in the electron density. This  $NO$  formation channel will be interrupted by the methane when combustion is involved as will be shown in the next section.

## 6.6 Temperatures and *NO* Concentrations in a Plasma Enhanced Flame

In this section, results in a plasma enhanced flame in a similar format as the previous section will be presented. The *NO* concentration is shown as a function of current, equivalence ratio, and total flow rate.

Glow to spark transition with even little energy dissipation can significantly contribute to the ignition of fuel during plasma assisted combustion due to the abundance of chemically active particles already present in the glow discharge. This random and continuous transition is then able to sustain the flame. Ignition in methane/air mixture can be achieved with equivalence ratios as low as 0.1. As stated in the description of plasmatron, the flame speed of premixed flames in this type of discharge can increase three fold or more at 300 *mA*, with further increase at higher currents. Also note that in the plasma energy added is on the order of 15-95% of the thermal energy from the combustion, which is generally reasonable in an ignition system of this kind. Keep in mind that the power level will be orders of magnitude lower than the actual combustion system which the igniter will be a part of in a practical system.

In Figure 6.7, we show the temperature and *NO* concentration as function of current and flow rate when the equivalence ratio is held at 1. It is apparent in Figure 6.6 (a) that the gas temperature increases with current, an indication that the deposition of heat increased when more energy is added to the flow. Unlike the discharge only case, the temperature increases with the flow rate. This is due to the heat release of the combustion

process which increases the temperature of the gas, and although the stoichiometry is maintained, the increased density of the burnt fuel in the confined arc chamber and through the exit of the torch results in a higher temperature. The plasma input power (current X voltage) to the flame is similar in magnitude to that of the plasma discharge only case. It can be seen that the NO production is reduced to a much lower level of 500 to 3500 *ppm* rather than the 8000 to 15000 *ppm* shown in the discharge only case. The relation of NO concentration in air over in PAC is shown in Table 6.3. Number for lower to higher current decreases, indicating a NO saturation towards higher current range. This reduction of *NO* has also been previously observed by Kim et al. [100, 101].

Table 6.3. *NO* Concentration in Air over in *PAC*

Times	20 <i>SCFH</i>	30 <i>SCFH</i>	40 <i>SCFH</i>	50 <i>SCFH</i>
100	19.64637	18.30008	18.50497	22.59199
200	9.050061	8.894798	8.58164	10.42774
300	7.534822	6.445892	6.047817	8.121705
400	5.94333	5.776397	5.223709	6.623402
500	5.796336	5.01545	4.525725	5.876072
600	4.976757	4.651474	4.129818	5.482375
700	4.697449	4.26576	3.948711	4.832408
800	4.201341	4.127193	3.662822	4.225948
900	4.509511	3.978688	3.463385	3.997834

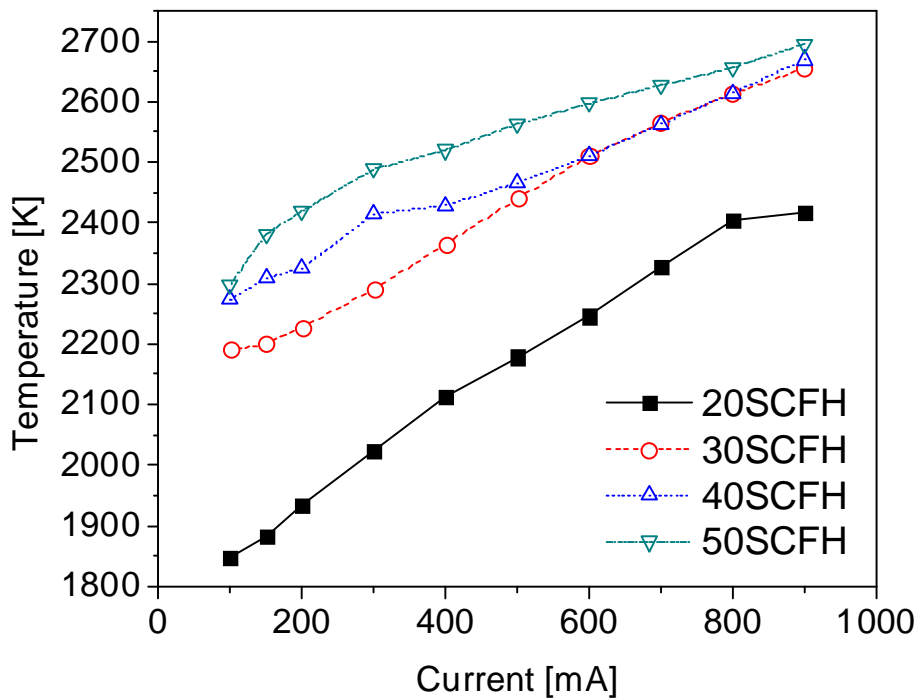
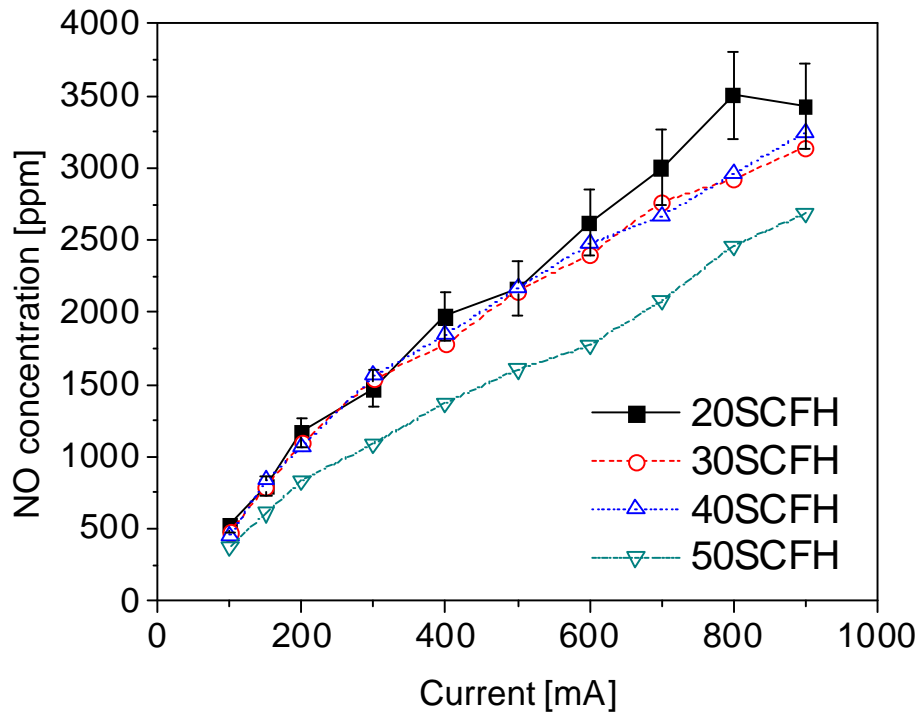


Figure 6.7 Temperature (a) and *NO* concentration (b) data as function of current and flow rate when the equivalence ratio is held at 1 in plasma assisted methane/air flame.

The main cause of this effect is the addition of methane which is a discharge interruption species (especially compared to other compositions  $O_2$  and  $N_2$ ) and alternative electron impact reactions which leads to reduce the NO formation. Note that temperature is high in the plasma assisted methane/air combustion (1850 ~ 2600 K), where thermal NO formation is most likely the dominant mechanism. In particular, we notice from Figure 6.7 that NO concentration surprisingly decreases with the flow rate although this leads to an increase in temperature and injection density of plasma energy into the flow. Upon further inspection, we note that the plasma energy input per molecule is actually decreased as the flow rate is increased from 20 SCFH to 50 SCFH. Energy input for each molecule is 0.203, 0.162, 0.159 and 0.154 (eV/molecule) for 20 SCFH, 30 SCFH, 40 SCFH and 50 SCFH, respectively at 100 mA and stoichiometric conditions. This lower power input per molecule at higher flow rate results in less electrons and collisions needed to initiate reactions that can result in the increase of NO. This is a clear example that although thermal NO is expected to be dominant in the high temperature range here, it is not the only mechanism.

In Figure 6.8, the temperature and NO concentration as a function of current and equivalence ratio when flow rate is held at 25 SCFH are shown. It can be seen that the NO increases with the current/power, and also with the total flow rate. Once again, it is interesting to note that NO formation is higher for leaner flames although the temperature is lower. Therefore, in addition to what can be expected from thermal formation of NO, we need to consider the impact of increased methane. This is addressed below.

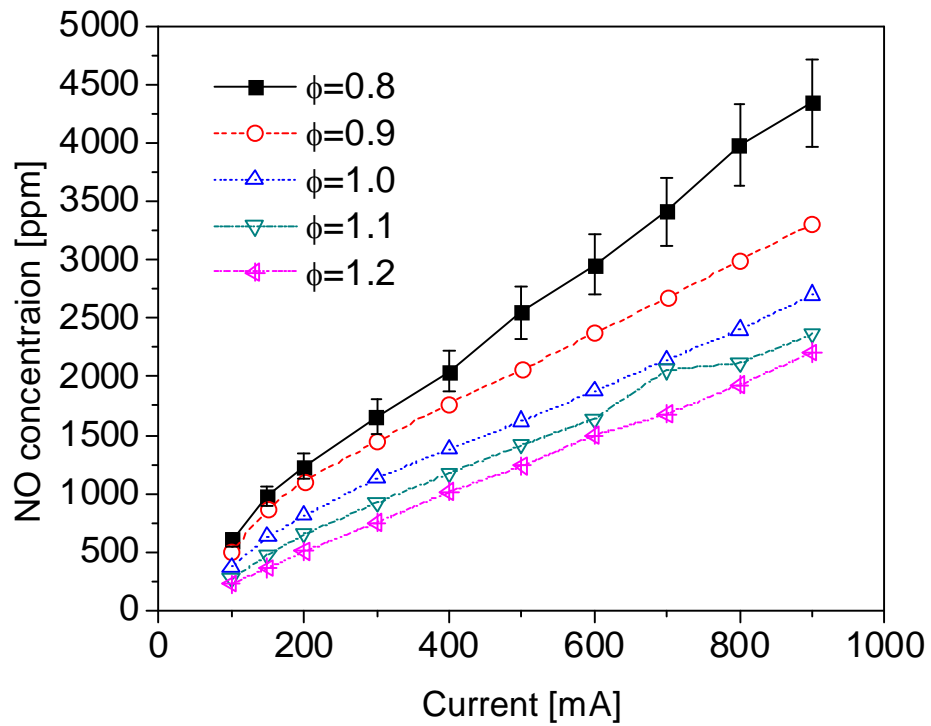
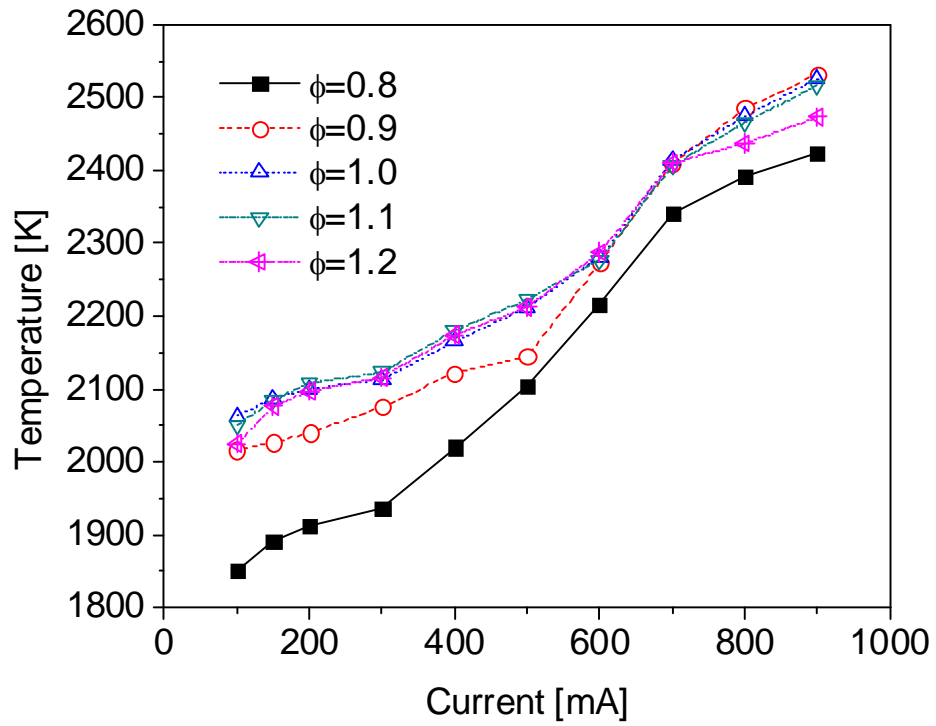


Figure 6.8 Temperature (a) and  $NO$  concentration (b) data as function of current and equivalence ratio when flow rate the same in plasma with methane/air combustion.

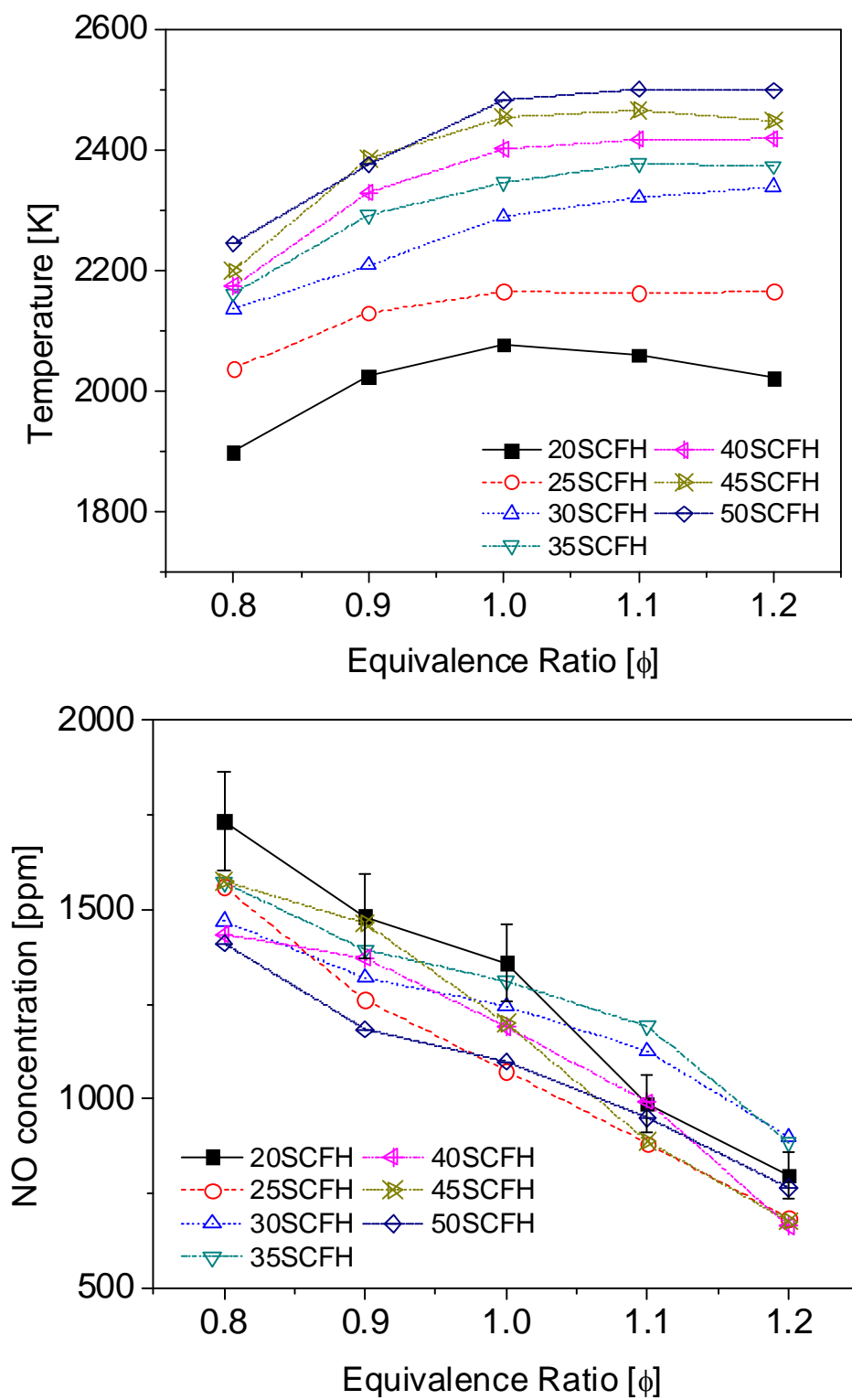


Figure 6.9 Temperature (a) and *NO* concentration (b) data with equivalence ratio and flow rate when the current is the same in plasma assisted methane/air combustion.

In Figure 6.9, we show the temperature and *NO* concentration as function of equivalence ratio and the flow rate when the current is held at 300 mA. The temperature profile as a function of equivalence ratio is similar to that of a typical case of combustion using methane without any plasma enhancements. The peak temperature is reached at an equivalence ratio close to 1, and higher current/power of the plasma increases the absolute temperature. The temperature for lower flow rate of methane/air mixture is lower than that of higher flow rate due to the less chemical heat release from combustion. It is interesting to observe the linear decay of *NO* as the equivalence ratio is increased. Note that *NO* quenching cross section with methane is extremely low [102], and therefore, interaction between the two species is negligible. On the other hand, methane will act as a discharge interruption species (especially compared to other composition *O*<sub>2</sub> and *N*<sub>2</sub>), and the indirect interaction between methane and discharge will significantly impact the *NO* formation. First, generation of vibrational nitrogen, a key factor for *NO* formation, is reduced even though the same amount of energy is added to the system as greater portion of it is allocated to alternative electron impact reactions, including breaking of *CH*<sub>4</sub> into smaller molecules. Second, as the flame becomes richer, unburnt hydrocarbons can also contribute to the reduction of *NO* through reburn reactions. Third, atomic oxygen and ozone generated from hydrocarbon help bring *NO* level down through reverse Zeldovich reaction  $NO+O \rightarrow N+O_2$  and through *NO* interactions with ozone. Atomic oxygen and ozone can be abundant in hydrocarbon/air mixtures when a plasma discharge is present and have been reported to increase flame propagation speed [3] and enhance flame speed

[103]. *NO* decay mechanism through atomic oxygen and ozone is confirmed experimentally and by using kinetic models in [104]. The main production channel of atomic oxygen is believed to be the dissociative quenching of  $O_2$  [105, 106] by  $N_2$ . Another potential explanation can be from the fact that as fuel reforming is increased in so called ‘cold pre-flame’ regions, it competes with *NO* formation reactions in the use of atomic oxygen, thus leading to the reduction of *NO* [79, 100]. In actual practice where this torch will be a part of a larger combustor, the additional chemistry and the fluid dynamics of the combustor will determine the overall *NO* formation, and the conditions of the igniter should be determined according to the conditions of the specific application.

## Chapter 7 Conclusions and Future Work

### 7.1 Microwave Discharge Results

A newly designed microwave re-entrant cavity applicator discharge system is used for plasma enhanced combustion to probe the concept of direct coupling of microwave power into the reaction zone of methane/oxygen mixtures. In the research, I have conducted optical and laser diagnostics to probe the physicochemical characteristics of coupling electromagnetic energy into the premixed flame. The flame was subjected to a wide range of microwave power and displayed three distinct stages, depending on the input microwave power as described below.

- **Stage 1:** “Electric Field Only Stage”: In this stage, the flame is influenced by only a weak electric field under 6  $W$ . No visual change can be seen in either the photographs or the *OH PLIF* as the power is increased. Most collisions in this stage are elastic leading to only ohmic heating, which is responsible for flammability limits expansion in this stage.
- **Stage 2:** “Transition Stage”: Between 6 and 10  $W$ , the plasma discharge and flame exist at the same time and the discharge volume is dramatically increased. Also, high electron temperatures and high reactivity lead to inelastic collisions for dissociate into new species, excitation and eventually ionization.

- **Stage 3:** “Full Plasma Stage” If microwave energy input exceeds 10  $W$ , the system enters a stage where the plasma plume dominates and the discharge emits a pink hue.

The number density of  $OH$  does not vary during Stage 1 but proceeds to rise rapidly through the rest of the stages as a plasma plume develops. Through Stage 1 of the coupling process, increase in the flammability limit, the flamespeed, and the rotational temperature (from  $OH$  Chemiluminescence) is observed from ohmic heating as a result of inelastic collisions. As the microwave power is raised, the electron temperature increases; generation of new radicals and breakdown of the gas results in a plasma plume. The plasma plume can be self sustained at this point without combustion and can re-ignite fuel and oxidizer. This plasma discharge grows in volume and luminosity as the power is further increased.

As the microwave power is increased further, the reaction zone is overlapped by a full plasma plume; the  $OH$  number density is relatively constant, but the  $CO$  concentration increases further. The importance of in-situ fuel reforming in plasma coupled flames is shown through the concentration of  $CO$ , which increases  $\sim 18\%$  with 30  $W$  microwave power. In this stage, the plasma discharge can be sustained without combustion and can ignite methane/oxygen mixture. The direct coupling of electromagnetic energy can be utilized for various levels of combustion enhancement and ignition for practical combustion systems including flame holding for harsh transient operating conditions.

## 7.2 DC Discharge Results

A DC plasmatron characterized by a nano-second glow-to-arc transient is used to investigate premixed and nonpremixed flames using *OH* Laser Induced Fluorescence and *CO* Two Photon Absorption Laser Induced Fluorescence (*TALIF*). Unique two cone flame geometry is seen for the nonpremixed mode, where the inner cone is produced by the plasma enhanced air mainly interacting with the flame and the outer one is from oxidation between input fuel and ambient air. Partial oxidation inside the chamber for premixed flames generally resulted in higher energy efficiencies compared to air discharge and diffusion mode as activation energy of methane is much lower than that of nitrogen. For nonpremixed flames, the flame is mainly stabilized by the reactive discharge of air in the inner core and the stability of nonpremixed flames is significantly influenced by the flowrates of the gases. By comparison of *OH PLIF* images in both modes for different total flow rates and equivalence ration, stability of premixed flames is more dependent on chemistry. *OH* number density for inner and outer cone indicates the increase of *OH* with increased discharge power, while stability for nonpremixed case depends on inner cone from discharge. Two photon *LIF* measurements of relative *CO* number density showed *CO* number density increases with high discharge power indicating that both configurations are significantly influenced by in-situ fuel reforming at higher plasma powers.

### 7.3 Nitric Oxide Measurements Results

To investigate Nitric Oxide formation in *DC* plasma assisted combustion, planar laser-induced fluorescence (*PLIF*) is used to acquire spatially resolved nitric oxide (*NO*) concentrations in plasma-enhanced flames of a transient arc plasmatron. Quantitative concentration of *NO* is calibrated by comparing the *LIF* signal to a well defined flat-flame calibration torch and using a *NO* addition method.

*IR* thermometry and a more accurate multi-line fitting technique of multiple *NO* transitions were used to obtain temperature field for two purposes: correction of *LIF* signal due to spectroscopic temperature dependence and also to investigate the changes in *NO* production as a variation of temperature.

Planar *LIF* images of *NO* were presented to show relative *NO* concentration in both cases of plasma only and plasma enhanced combustion. In the case of plasma only, *NO* production is high in the region of 8000 to 15000 *ppm* with *DC* power input of 200 to 750 *Watts*. Temperature range at these conditions is 550 to 1250 *K* where thermal *NO* production is minor and *NO* formation is predominantly from  $N_2(v)+O \rightarrow NO+N$ .

For plasma enhanced combustion case, *NO* production in methane/air flame for investigated equivalence ratio range is about one order lower in magnitude. In this case temperature is so high that thermal *NO* mechanism is still dominant. Plasma power and equivalence ratio are the two main operational parameters in producing *NO* in the combustion system here. For lower *NO* concentration in plasma enhanced flames of this

type, we need to avoid lean and high current conditions. Linear decay from equivalence ratio 0.8 to 1.2 may be caused by quenching of vibrational nitrogen, interactions with atomic oxygen and ozone, and reaction with unburned hydrocarbon species at rich conditions.

#### **7.4 Some Suggestions for Future Work**

The plasma assisted combustion research is a challenge field with numerous unsolved problems but the ultimate goal is to identify and quantify every mechanism and apply the concept in real life for better fuel efficiency and less emission. Plasma assisted combustion may contribute to solution of current energy crisis as well as the problem of global warming.

The current research uses several thermometries: thermocouple, *IR* thermometry, *NO* multi-line thermometry and *OH* rotational thermometry. However, a more advanced measurement (e.g. Rayleigh scattering thermometry) could offer a more accurate temperature field, and thus better validate any simulation work and therefore, the robustness and accuracy of future plasma assisted combustion detailed mechanisms.

One important and significant aspect of current study lies in that all discharge systems are under atmospheric pressure, which is more practical than a low pressure discharge and also cost efficient without extensive pumping systems; and meanwhile, discharge is achieved at low input electric power. But the use of pulsed discharge might be a crucial aspect to further investigate the combustion dynamics for more detailed studies and comparisons. The use of a pulsed discharge would provide a more

equilibrium with higher efficiency, even though the cost is double or more. Implementation of a discharge system with a real-life combustor (e.g. *IC* engines) will offer more insights on future plasma assisted combustion applications under real work environments (higher pressure, requirements for lower total weight, etc.)

To extend current research, different enhancement mechanisms (thermal, kinetics, in-situ fuel reforming and etc.) should be quantified and compared with different systems for their roles in plasma assisted combustion. For now, these mechanisms are believed to contribute to enhancements when plasma is coupled into flames, but how much each mechanism influences enhancement for different systems is still unknown and would be interesting.

## **BIBLIOGRAPHY**

## BIBLIOGRAPHY

- [1] Bittencourt, *Fundamentals of plasma physics*, 3rd ed: the author, 2003.
- [2] S. M. Starikovskaia, "Plasma assisted ignition and combustion," *Journal of Physics D: Applied Physics*, vol. 39, pp. R265-R299, 2006.
- [3] A. Y. Starikovskii, "Plasma supported combustion," *Proceedings of the Combustion Institute*, vol. 30, pp. 2405-2417, 2005.
- [4] A. B. Leonov, D. A. Yarantsev, A. P. Napartovich, and I. V. Kochetov, "Plasma-assisted ignition and flameholding in high-speed flow," presented at 44th AIAA Aerospace Sciences Meeting, AIAA-2006-563, Reno, Nevada, 2006.
- [5] S. B. Leonov and D. A. Yarantsev, "Plasma-induced ignition and plasma-assisted combustion in high-speed flow," *Plasma Sources Science and Technology*, vol. 16, pp. 132-138, 2007.
- [6] T. Ombrello, Y. Ju, and A. Fridman, "Kinetic Ignition Enhancement of Diffusion Flames by Nonequilibrium Magnetic Gliding Arc Plasma," *AIAA J.*, vol. 46, pp. 2424-2433, 2008.
- [7] T. Ombrello, S. H. Won, and Y. Ju, "Lifted Flame Speed Enhancement by Plasma Excitation of Oxygen," presented at 47th AIAA Aerospace Sciences Meeting and Exhibit, AIAA-2009-689, 2009.
- [8] W. Kim, H. Do, M. G. Mungal, and M. A. Cappelli, "Plasma-Discharge Stabilization of Jet Diffusion Flames," *IEEE Transactions on Plasma Science*, vol. 34, pp. 2545-2551, 2006.
- [9] W. Kim, M. Godfrey Mungal, and M. A. Cappelli, "The role of in situ reforming in plasma enhanced ultra lean premixed methane/air flames," *Combustion and Flame*, pp. doi:10.1016/j.combustflame.2009.06.016, 2009.
- [10] E. Mintusov, A. Serdyuchenko, I. Choi, W. R. Lempert, and I. V. Adamovich, "Mechanism of Plasma Assisted Oxidation and Ignition of Ethylene-Air Flows by a Repetitively Pulsed Nanosecond Discharge," presented at 46th AIAA Aerospace Sciences Meeting and Exhibit, AIAA 2008-1106, 2008.
- [11] M. Uddi, N. Jiang, E. Mintusov, I. V. Adamovich, and W. R. Lempert, "Atomic

Oxygen Measurements in Air and Air/Fuel Nanosecond Pulse Discharges by Two Photon Laser Induced Fluorescence," presented at 46th AIAA Aerospace Sciences Meeting and Exhibit, AIAA 2008-1110, Orlando, Fl, 2008.

- [12] E. S. Stockman, S. H. Zaidi, R. B. Miles, C. D. Carter, and M. D. Ryan, "Measurements of combustion properties in a microwave enhanced flame," *Combustion and Flame*, vol. 156, pp. 1453-1461, 2009.
- [13] C. T. Bowman, "Gas-phase reaction mechanisms for nitrogen oxide formation and removal in combustion," in *Pollutants from Combustion*, C. Vovelle, Ed. Netherlands: Kluwer Academic Publishers, 2000, pp. 123-144.
- [14] J. Warnatz, U. Maas, and R. W. Dibble, *Combustion*, 3 ed. Berlin-Heidelberg-New York: Springer, 1997.
- [15] B. Atakan and A. T. Hartlieb, "Laser Diagnostics of NO reburning in fuel-rich propene flames," *Applied Physics B-Lasers and Optics*, vol. 71, pp. 697-702, 2000.
- [16] I. Orlandini and U. Riedel, "Modelling of NO and HC removal by non-thermal plasmas," *Combustion Theory and Modelling*, vol. 5, pp. 447-462, 2001.
- [17] L. Magne, S. Pasquiers, N. Blin-Simiand, and C. Postel, "Production and reactivity of the hydroxyl radical in homogeneous high pressure plasmas of atmospheric gases containing traces of light olefins," *Journal of Physics D: Applied Physics*, vol. 40, pp. 3112-3127, 2007.
- [18] H. F. Calcote and R. N. Pease, "Electrical properties of flames," *Industrial and Engineering Chemistry*, vol. 43, pp. 2726-2731, 1951.
- [19] H. F. Calcote and C. H. Berman, "Increased methane-air stability limits by a DC electric field," presented at Proceedings of the ASME Fossil Fuels Combustion Symposium, I1989.
- [20] G. P. Tweari and J. R. Wilson, *Combustion and Flame*, vol. 24, 1975.
- [21] T. Kitagawa, A. Moriwaki, K. Murakami, K. Takita, and G. Masuya, "Ignition characteristics of methane and hydrogen using a plasma torch in supersonic flow," *Journal of Propulsion and Power*, vol. 19, pp. 853-858, 2003.
- [22] A. Y. Starikovskii, N. B. Anikin, I. N. Kosarev, E. I. Mintousov, M. M. Nudnova,

- A. E. Rakitin, D. V. Roupasov, S. M. Starikovskaia, and V. P. Zhukov, "Nanosecond-pulsed Discharge for Plasma-Assisted Combustion and Aerodynamics," *Journal of Propulsion and Power*, vol. 24, pp. 1182-1197, 2008.
- [23] G. Lou, A. Bao, M. Nishihara, S. Keshav, Y. G. Utkin, J. W. Rich, W. R. Lempert, and I. V. Adamovich, "Ignition of Premixed Hydrocarbon-Air Flows by Repetitively Pulsed, Nanosecond Pulse Duration Plasma," *Proceedings of the Combustion Institute*, vol. 31, pp. 3327-3334, 2007.
- [24] N. Chintala, A. Bao, G. Lou, and I. V. Adamovich, "Measurements of combustion efficiency in nonequilibrium RF plasma-ignited flows," *Combustion and Flame*, vol. 144, pp. 744-756, 2006.
- [25] I. V. Kuznetsova, N. Y. Kalashnikov, A. F. Gutsol, A. F. Fridman, and L. A. Kennedy, "Effect of "overshooting" in the transitional regimes of the low-current gliding arc discharge," *J. Appl. Phys*, vol. 92, pp. 4231-4237, 2002.
- [26] Y. D. Korolev and I. B. Matveev, "Nonsteady-State Processes in a Plasma Pilot for Ignition and Flame Control," *Plasma Science, IEEE Transactions on*, vol. 34, pp. 2507-2513, 2006.
- [27] L. Bromberg, D. R. Cohn, A. Rabinovitch, and J. Heywood, "Emissions Reductions Using Hydrogen from Plasmatron Fuel Converters," *Inter. J. of Hydrogen Energy*, vol. 26, pp. 1115-1121, 2001.
- [28] S. H. Zaidi, E. Stockman, X. Qin, Z. Zhao, S. Macheret, Y. Ju, R. B. Miles, D. J. Sullivan, and J. F. Kline, "Measurements of hydrocarbon flame speed enhancement in high-Q microwave cavity," presented at 44th AIAA Aerospace Sciences Meeting and Exhibit, AIAA-2006-1217, 2006.
- [29] W. Kim, H. Do, M. G. Mungal, and M. A. Cappelli, "Investigation of NO production and flame structure in plasma enhanced premixed combustion," *Proc. Combust. Inst*, vol. 31, pp. 3319-3326, 2007.
- [30] G. Pilla, D. Galley, D. A. Lacoste, F. Lacas, D. Veynante, and C. O. Laux, "Stabilization of a Turbulent Premixed Flame Using a Nanosecond Repetively Pulsed Plasma," *IEEE Trans. on Plasma Science*, vol. 34, pp. 2471-2477, 2006.
- [31] T. Ombrello, X. Qin, Y. Ju, A. Gutsol, A. Fridman, and C. Carter, "Combustion Enhancement via Stabilized Piecewise Nonequilibrium Gliding Arc Plasma Discharge," *AIAA J.*, vol. 44, pp. 142-150, 2006.

- [32] C. S. Kalra, A. Gutsol, and A. Fridman, "Gliding arc discharge as a source of intermediate plasma for methane partial oxidation," *IEEE Transactions on Plasma Science*, vol. 33, pp. 32-41, 2005.
- [33] L. Wu, J. Lane, N. P. Cernansky, D. L. Miller, A. A. Fridman, and A. Y. Starikovskii, "Plasma-assisted ignition below self-ignition threshold in methane, ethane, propane and butane- air mixtures," *Proceedings of Combustion Institute*, vol. doi:10.1016/j.proci.2010.06.003, 2010.
- [34] A. Bao, "Ignition of hydrocarbon fuels by a repetitively pulsed nanosecond pulse duration plasma," in *Department of Mechanical Engineering*, vol. Doctor Of Philosophy: Ohio State University, 2008.
- [35] N. Chintala, R. Meyer, A. Hicks, A. Bao, J. W. Rich, W. R. Lempert, and I. V. Adamovich, "Non-Thermal Ignition of Premixed Hydrocarbon-Air Flows by Nonequilibrium RF Plasma," *Journal of Propulsion and Power*, vol. 21, pp. 583-590, 2005.
- [36] A. C. Eckbreth, *Laser Diagnostics for Combustion Temperature and Species*. Amsterdam: Gordon and Breach, 1996.
- [37] D. R. Crosley, "Laser Probes for Combustion Chemistry," American Chemical Society, Washington D.C. 1980.
- [38] K. Kohse-Höinghaus, "Laser Techniques for the Quantitative Detection of Reactive Intermediates in Combustion Systems," *Progr. Energy Combust. Sci.*, vol. 20, pp. 203-279, 1994.
- [39] J. W. Daily, "Laser Induced Fluorescence Spectroscopy in Flames," *Progr. Energy Combust. Sci.*, vol. 23, pp. 133-199, 1997.
- [40] C. N. Banwell and E. M. McCash, *Fundamentals of Molecular Spectroscopy*, 4 ed: McGraw-Hill, 1994.
- [41] W. Demtröder, *Laser Spectroscopy*. Berlin: Springer-Verlag, 1982.
- [42] N. M. Laurendeau and J. E. M. Goldsmith, "Comparison of hydroxyl concentration profiles using five laser-induced fluorescence methods in a lean subatmospheric-pressure H<sub>2</sub>/O<sub>2</sub>/Ar flame," *Combust. Sci. Technol.*, vol. 63, pp. 139-152, 1989.

- [43] A. Yariv, *Quantum Electronics*. New York: Wiley and Sons, 1975.
- [44] W. G. Bessler, "Quantitative nitric oxide concentration and temperature imaging in flames over a wide pressure range with laser-induced fluorescence," vol. Ph.D.: Heidelberg University, 2003.
- [45] W. P. Patridge and N. M. Laurendeau, "Formulation of a dimensionless overlap fraction to account for spectrally distributed interactions in fluorescence studies," *Applied Optics*, vol. 34, pp. 2645, 1995.
- [46] D. R. Grieser and R. H. Barnes, "Nitric Oxide Measurements in a Flame by Laser Fluorescence," *Applied Optics*, vol. 19, pp. 741-743, 1980.
- [47] R. L. McKenzie and K. P. Gross, "Two-photon excitation of nitric oxide fluorescence as a temperature indicator in unsteady gasdynamic processes," *Applied Optics*, vol. 20, pp. 2153-2165, 1981.
- [48] G. Kychakoff, R. D. Howe, and R. K. Hanson, "Quantitative Flow Visualization Technique for Measurements in Combustion Gases," *Applied Optics*, vol. 23, pp. 704-712, 1984.
- [49] P. H. Paul, M. P. Lee, B. K. McMillin, J. M. Seitzman, and R. K. Hanson, "Application of Planar Laser-Induced Fluorescence Imaging Diagnostics to Supersonic Reacting Flow," *28th AIAA/SAE/ASME/ASEE Joint Propulsion Conf., Orlando, FL*, pp. paper 90-1844, 1990.
- [50] C. F. Kaminski, J. Holt, and M. Alden, "High repetition rate planar laser induced fluorescence of OH in a turbulent non-premixed flame," *Appl. Phys. B*, vol. 68, pp. 757, 1999.
- [51] C. Kittler and A. Dreizler, "Cinematographic imaging of hydroxyl radicals in turbulent flames by planar laser-induced fluorescence up to 5 kHz repetition rate," *Appl. Phys. B.*, vol. 89, pp. 163-166, 2007.
- [52] N. Jiang and W. R. Lempert, "Ultrahigh-frame-rate nitric oxide planar laser-induced fluorescence imaging," *OPTICS LETTERS*, vol. 33, pp. 2236-2238, 2008.
- [53] W. G. Bessler, C. Schulz, V. Sick, and J. W. Daily, "A versatile modeling tool for nitric oxide LIF spectra," presented at 3rd Joint Meeting US Sec. Combust. Inst., Chicago ([www.lifsim.com](http://www.lifsim.com)), 2003.

- [54] Y. P. Raizer, "Propagation of a high-pressure microwave discharge," *Soviet Physics JETP-USSR*, vol. 34, pp. 114, 1972.
- [55] R. M. Fredericks and J. Asmussen, "Retuning and hysteresis effects of a rf plasma in a variable size microwave cavity," *J. Appl. Physics*, vol. 42, pp. 3647-3649, 1971.
- [56] X. Rao, K. Hemawan, I. Wichman, C. Carter, T. Grotjohn, J. Asmussen, and T. Lee, "Combustion dynamics for energetically enhanced flames using direct microwave energy coupling," *Proceedings of the Combustion Institute*, vol. doi:10.1016/j.proci.2010.06.024, 2010.
- [57] K. W. Hemawan, I. S. Wichman, T. Lee, T. A. Grojohn, and J. Asmussen, "Compact Microwave Reentrant Cavity Applicator for Plasma Assisted Combustion," *Submitted*, 2009.
- [58] K. Hamawan, C. Romel, S. Zuo, I. Wichman, T. Grotjohn, and J. Asmussen, "Microwave plasma assisted premixed flame combustion," *Appl. Phys. Lett.*, vol. 89, pp. 141501, 2006.
- [59] K. W. Hemawan, C. L. Romel, S. Zuo, I. S. Wichman, T. A. Grotjohn, and J. Asmussen, "Microwave plasma-assisted premixed flame combustion," *Appl. Phys. Lett.*, vol. 89, pp. 141501, 2006.
- [60] Y. D. Korolev, O. B. Frants, N. V. Landl, V. G. Geyman, and I. B. Matveev, "Glow-to-Spark Transitions in a Plasma System for Ignition and Combustion Control," *Plasma Science, IEEE Transactions on*, vol. 35, pp. 1651-1657, 2007.
- [61] K. Kohse-Hoinghaus and J. B. Jeffries, *Applied Combustion Diagnostics*: Taylor & Francis, 2002.
- [62] P. H. Paul, "A Model For Temperature-Dependent Collisional Quenching of OH  $A^2\Sigma^+$ ," *J. Quant. Spectrasc. Radiat. Transfer*, vol. 51, pp. 511-524, 1994.
- [63] J. M. Seitzman, J. Haumann, and R. K. Hanson, "Quantitative two photon LIF imaging of carbon monoxide in combustion gases," *Applied Optics*, vol. 26, pp. 2892-2899, 1987.
- [64] "GRI-Mech 3.0 <http://www.me.berkeley.edu/gri-mech/version30.>"
- [65] C. Schulz, V. Sick, U. E. Meier, J. Heinze, and W. Stricker, "Quantification of NO

- A-X(0,2) laser-induced fluorescence: investigation of calibration and collisional influences in high-pressure flames," *Applied Optics*, vol. 38, pp. 1434-1443, 1999.
- [66] T. Pedersen and R. C. Brown, "Simulation of electric field effects in premixed methane flames," *Combustion and Flame*, vol. 94, pp. 433-448, 1993.
- [67] Y. Ju, S. O. Macheret, M. N. Shneider, R. B. Miles, and D. J. Sullivan, "Numerical study of the effect of microwave discharge on the premixed methane-air flame," presented at 40th AIAA/ASME/SAE/ASEE Joint Propulsion Conference and Exhibit, Fort Lauderdale, FL, 2004.
- [68] R. Ono and T. Oda, "OH radical measurement in a pulsed arc discharge plasma observed by a LIF method," *IEEE Transaction on Industry Applications*, vol. 37, pp. 709-714, 2001.
- [69] Q. V. Nguyen, R. W. Dibble, C. D. Carter, G. J. Fiechtner, and R. S. Barlow, "Raman-LIF Measurements of Temperature, Major Species, OH, and NO in a Methane-Air Bunsen Flame," *Combustion and Flame*, vol. 105, pp. 499-510, 1996.
- [70] K. Shinohara, N. Takada, and K. Sasaki, "Enhancement of burning velocity in premixed burner flame by irradiating microwave power," *J. Phys. D: Appl. Phys.*, vol. 42, pp. 182008 (4pp), 2009.
- [71] K. W. Hemawan, I. S. Wichman, T. Lee, T. A. Grotjohn, and J. Asmussen, "Compact Microwave Reentrant Cavity Applicator for Plasma Assisted Combustion," *Review of Scientific Instruments*, vol. 80, pp. 053507, 2009.
- [72] M. Uddi, "Non-equilibrium kinetic studies of repetitively pulsed nanosecond discharge plasma assisted combustion," in *Department of Mechanical Engineering*, vol. Ph.D.: Ohio State University, 2008.
- [73] P. W. J. M. Boumans, *Inductively Coupled Plasma Emission Spectroscopy*, vol. Part 2. New York, Chichester, Brisbane, Toronto, Singapore: John Wiley & Sons, 1987.
- [74] J. Happold, P. Lindner, and B. Roth, "Spatially resolved temperature measurements in an atmospheric plasma touch using the  $A^2, v=0 \rightarrow X^2, v'=0$  OH band," *J. Phys. D: Appl. Phys.*, vol. 39, pp. 3615-3620, 2006.
- [75] S. Pellerin, J. M. Cormier, F. Richard, K. Musiol, and J. Chapelle, "A

- spectroscopic Diagnostic Method using UV OH band spectrum," *J. Phys. D: Appl. Phys.*, vol. 29, pp. 726, 1996.
- [76] H. P. Broida, *J. of Chem. Phys.*, vol. 21, pp. 1165-1169, 1953.
- [77] A. G. Gaydon and H. G. Wolfhard, *Flames, their structure, radiation and temperature*, 3rd ed, 1970.
- [78] E. S. Stockman, J. B. Michael, A. Fuller, S. H. Zaidi, and R. B. Miles, "Toward High Q Evanescent Coupled Microwave Controlled Combustion," presented at 47th AIAA Aerospace Sciences Meeting Including The New Horizons Forum and Aerospace Exposition, 2009.
- [79] W. Kim, H. Do, M. G. Mungal, and M. A. Cappelli, "A Study of Plasma Stabilized Diffusion Flames at Elevated Ambient Temperatures," *IEEE Transactions on Plasma Science*, vol. 36, pp. 2898-2904, 2008.
- [80] L. Bromberg, D. R. Cohn, A. Rabinovich, and J. Heywood, "Emission reductions using hydrogen from plasmatron fuel converters," *International Journal of Hydrogen Energy*, vol. 26, pp. 1161-1121, 2001.
- [81] L. Bromberg, D. R. Cohn, A. Rabinovich, and N. Alexeev, "Plasma catalytic reforming of methane," *International Journal of Hydrogen Energy*, vol. 24, pp. 1131-1137, 1999.
- [82] Y. D. Korolev, O. B. Frants, N. V. Landl, V. G. Geyman, and I. B. Matveev, "Nonsteady-State Gas-Discharge Processes in Plasmatron for Combustion Sustaining and Hydrocarbon Decomposition," *IEEE Transaction on Plasma Science*, vol. 37, pp. 586-592, 2009.
- [83] X. Rao, I. Matveev, and T. Lee, "Nitric Oxide Formation in a Premixed Flame With High-Level Plasma Energy Coupling," *IEEE Transaction on Plasma Science*, vol. 37, pp. 2303-2313, 2009.
- [84] J. J. Lowke and R. Morrow, "Theoretical analysis of removal of oxides of sulphur and nitrogen in pulsed operation of electrostatic precipitators," *IEEE Transaction on Plasma Science*, vol. 23, pp. 661-671, 1995.
- [85] J. B. Kelman, D. A. Greanhalgh, E. Ramsay, D. Xiao, and D. T. Reid, "Flow imaging by use of femtosecond-laser-induced two-photon fluorescence," *Optics Letters*, vol. 29, pp. 1973-1975, 2004.

- [86] A. V. Mokhov, H. B. Levinsky, C. E. v. d. Meij, and R. A. A. M. Jacobs, "Analysis of laser-induced-fluorescence carbon monoxide measurements in turbulent nonpremixed flames," *Applied Optics*, vol. 34, pp. 7074-7082, 1995.
- [87] X. Rao, T. Lee, and I. Matveev, "Nitric Oxide Formation during Ignition and Combustion of a Transient Arc Plasmatron," presented at 47th AIAA Aerospace Sciences Meeting, 2009.
- [88] A. H. Lefebvre, *Gas Turbine Combustion*. Philadelphia, PA: Taylor & Francis, 1999.
- [89] J. T. Herron, "Modeling Studies of the Formation and Destruction of NO in pulsed barrier discharges in nitrogen and air," *Plasma Chem. Plasma Process*, vol. 21, pp. 581-609, 2001.
- [90] G. Zhao, S. V. B. Janardhan, X. Hu, M. D. Argyle, and M. Radosz, "Effect of oxygen on nonthermal plasma reactions of nitrogen oxides in nitrogen," *Environmental and energy engineering*, vol. 51, pp. 1800-1812, 2005.
- [91] K. Kohse-Höinghaus and J. B. Jeffries, *Applied Combustion Diagnostics*: Taylor and Francis, 2002.
- [92] M. D. DiRosa, K. G. Klavuhn, and R. K. Hanson, "LIF Spectroscopy of NO and O<sub>2</sub> in High-Pressure Flames," *Combustion Science and Technology*, vol. 118, pp. 257-283, 1996.
- [93] W. G. Bessler, C. Schulz, T. Lee, J. B. Jeffries, and R. K. Hanson, "Strategies for laser-induced fluorescence detection of nitric oxide in high-pressure flames. III. Comparison of *A-X* excitation schemes," *Applied Optics*, vol. 42, pp. 4922-4936, 2003.
- [94] T. Lee, W. G. Bessler, H. Kronmayer, C. Schulz, and J. B. Jeffries, "Quantitative temperature measurements in high-pressure flames with multiline NO-LIF thermometry," *Applied Optics*, vol. 44, pp. 6718-6728, 2005.
- [95] P. A. Berg, G. P. Smith, J. B. Jeffries, and D. R. Crosley, "Nitric oxide formation and reburn in low-pressure methane flames," *Proceedings of the Combustion Institute*, vol. 27, pp. 1377-1384, 1998.
- [96] J. H. Bromly, F.J.Barnes, S.Muris, X.You, and B.S.Haynes, "Kinetic and Thermodynamic Sensitivity Analysis of the NO-Sensitised Oxidation of

- Methane," *Combustion Science and Technology*, vol. 115, pp. 259-296, 1996.
- [97] W. G. Bessler and C. Schulz, "Quantitative multi-line NO-LIF temperature imaging," *Applied Physics B*, vol. 78, pp. 519-533, 2004.
- [98] A. Fridman and L. Kennedy, *Plasma Physics and Engineering*. New York: Taylor and Francis, 2004.
- [99] B. F. Gordiets, C. M. Ferreira, V. L. Guerra, J. M. A. H. Loureiro, J. Nahorny, D. Pagnon, M. Touzeau, and M. Vialle, "Kinetic model of a low pressure N<sub>2</sub> O<sub>2</sub> flowing glow discharge," *IEEE Transactions on Plasma Science*, vol. 4, pp. 750-768, 1995.
- [100] W. Kim, H. Do, M. G. Mungal, and M. A. Cappelli, "Investigation of NO production and flame structure in plasma enhanced premixed combustion," *Proceedings of the Combustion Institute*, vol. 31, pp. 3319-3326, 2007.
- [101] W. Kim, M. G. Mungal, and M. A. Cappelli, "The role of in situ reforming in plasma enhanced ultra lean premixed methane/air flames," 2009.
- [102] M. C. Drake and J. W. Ratcliffe, "High Temperature Quenching cross sections for nitric oxide laser-induced fluorescence measurements," *J. Chem. Phys.*, vol. 98, pp. 3850-3865, 1993.
- [103] T. Ombrello, S. H. Won, Y. Ju, and S. Williams, "Lifted Flame Speed Enhancement by Ozone," presented at 4th International Workshop and Exhibition on Plasma Assisted Combustion, 2008.
- [104] M. Uddi, N. Jiang, I. V. Adamovich, and W. R. Lempert, "Nitric Oxide Density Measurements in Air and Air/Fuel nanosecond pulse discharges by laser induced fluorescence," *J. Phys. D: Appl. Phys.*, vol. 42, pp. 075205, 2009.
- [105] G. D. Stancu, F. Kaddouri, D. A. Lacoste, and C. O. Laux, "Investigations of rapid plasma chemistry generated by nanosecond discharges in air at atmospheric pressure using advanced optical diagnostics," presented at 47th AIAA Aerospace Sciences Meeting, Orlando, FL, 2009.
- [106] M. Uddi, N. Jiang, E. Mintusov, I. V. Adamovich, and W. R. Lempert, "Atomic oxygen measurements in air and air/fuel nanosecond pulse discharge by two photon laser induced fluorescence," *Proc. Combust. Inst.*, vol. 32, pp. 929-936, 2009.